



Universität Hamburg

DER FORSCHUNG | DER LEHRE | DER BILDUNG

Pump-probe experiments, driven by high-field THz pulses, shaped by double electron bunches at FLASH

Dissertation

ZUR ERLANGUNG DES DOKTORGRADES

an der Fakultät für Mathematik, Informatik
und Naturwissenschaften
Fachbereich Physik
der Universität Hamburg

vorgelegt von

Ekaterina Zapolnova

August 2020

Gutachter/in der Disputation:

Dr. Elke Plönjes-Palm

Prof. Dr. Ulrike Frühling

Prof. Dr. Daniela Pfannkuche

Prof. Dr. Michael Gensch

Dr. Martin Beye

Datum der Disputation:

12.08.2020

Vorsitzende der Prüfungskommission:

Prof. Dr. Daniela Pfannkuche

Vorsitzender Fach-Promotionsausschusses:

Prof. Dr. Günter Hans Walter Sigl

Leiter des Fachbereichs Physik:

Prof. Dr. Wolfgang Hansen

Dekan der MIN Fakultät:

Prof. Dr. Heinrich Graener

Dedicated to my mother

Abstract

The Free Electron Laser in Hamburg (FLASH) has a unique combination of high repetition rate, tunable, intense, and narrowband THz pulses naturally synchronized to the XUV pulses. It provides the opportunity to investigate light-matter interaction on an ultrafast timescale. However, due to the different properties of THz and XUV radiation, the optical transport differs for these pulses. The result is that the optical path of the THz beamline is several meters longer than the XUV beamline, preventing the utilization of the full potential of FLASH.

This work demonstrates a new approach for XUV-THz pump-probe experiments at FELs, providing a solution to the optical path difference problem of naturally synchronized THz and XUV pulses. The described THz Doubler scheme is based on the generation of two consecutive electron bunches, separated in time, to enable temporal overlap of THz and XUV pulses at the experiment. The first bunch is specifically tuned for the generation of THz radiation and the second for XUV with the achieved synchronization of 19 fs r.m.s.. This new scheme enables pump-probe experiments with high temporal resolution, high pulse energies, and tunable XUV and THz wavelengths.

Temporal and spatial overlap is critical for ultrafast XUV-THz pump-probe experiments, both at FEL facilities and at table-top high harmonic sources. A simple and robust spatio-temporal overlap tool was developed and is presented here. It is based on ultrafast changes of the optical properties of silicon induced by ultrafast XUV pulses and probed by THz pulses, and enables the arrival time between XUV and THz pulses to be measured with temporal resolution comparable to the duration of the THz pulse.

Finally, a novel Fourier transform infrared (FTIR) spectrometer, based on the reflective lamellar grating and operating over an extremely broad spectral range of THz frequencies, has been developed and commissioned. The lamellar grating interferometer, in contrast to the typical Michelson interferometer, has a much higher throughput and almost constant frequency response, making it an ideal tool for spectral characterization of broadband sources.

Kurzfassung

Der Freie-Elektronen-Laser in Hamburg (FLASH) verfügt über eine einzigartige Kombination aus hochrepetitiven, durchstimmbaren, intensiven und schmalbandigen THz-Pulsen, welche naturgemäß mit den XUV-Pulsen synchronisiert sind. Diese Eigenschaft bietet die Möglichkeit Licht-Materie-Wechselwirkungen auf einer ultraschnellen Zeitskala zu untersuchen, wobei sich aufgrund der unterschiedlichen Eigenschaften von THz- und XUV-Strahlung der optische Transport für diese Pulse unterscheidet.

Diese Arbeit demonstriert einen neuen Ansatz für XUV-THz pump-probe Experimente an FELs und bietet eine Lösung für das Problem der optischen Weglängendifferenz von natürlich synchronisierten THz- und XUV-Pulsen. Das beschriebene THz-Doppler-Schema basiert auf der Erzeugung von zwei aufeinanderfolgenden, zeitlich getrennten Elektronenpaketen, um einen zeitlichen Überlapp von THz- und XUV-Pulsen am Experiment zu ermöglichen. Das erste Bündel ist speziell auf die Erzeugung von THz-Strahlung und das zweite auf XUV-Strahlung abgestimmt und erlaubt eine Synchronisation auf 19 fs r.m.s.. Dadurch ermöglicht dieses neue Schema pump-probe Experimente mit hoher zeitlicher Auflösung, hohen Pulsenergien und durchstimmbaren XUV- und THz-Wellenlängen.

Der zeitliche und räumliche Überlapp ist für ultraschnelle XUV-THz pump-probe Experimente, sowohl an FEL-Anlagen, als auch an Laborquellen mit hohen harmonischen von entscheidender Bedeutung. Ein einfaches und robustes Werkzeug wurde entwickelt und wird hier vorgestellt. Es basiert auf ultraschnellen Änderungen der optischen Eigenschaften von Silizium, die durch ultraschnelle XUV-Pulse induziert, und mit THz-Pulsen abgetastet werden. Dies ermöglicht die Messung der Ankunftszeit zwischen XUV- und THz-Pulsen mit einer zeitlichen Auflösung, welche in der Größenordnung der Pulsdauer der THz-Pulse liegt.

Darüberhinaus wurde ein neuartiges Fourier-Transform-Infrarotspektrometer (FTIR) entwickelt und in Betrieb genommen. Es basiert auf einem reflektierenden Lamellengitter und arbeitet über einen extrem breiten Spektralbereich von THz-Frequenzen. Das Lamellengitter-Interferometer hat im Gegensatz zum typischen Michelson-Interferometer eine deutlich höhere Effizienz und einen nahezu konstanten Frequenzgang, was es zu einem idealen Werkzeug für die spektrale Charakterisierung von Breitbandquellen macht.

List of publications

1. **E. Zapolnova**, T. Golz, R. Pan, K. Klose, S. Schreiber and N. Stojanovic, THz pulse doubler at FLASH: double pulses for pump–probe experiments at X-ray FELs, *Journal of Synchrotron Radiation*, (2018) 25, 39–43
2. **E. Zapolnova**, R. Pan, T. Golz, M. Sindik, M. Nikolic, M. Temme, M. Rabasovic, D. Grujic, Z. Chen, S. Toleikis and N. Stojanovic, XUV plasma switch for THz: new temporal overlap tool for XUV-THz pump-probe experiments at FELs, *Journal of Synchrotron Radiation*, (2019), 27(1), 11-16
3. R. Pan, **E. Zapolnova**, T. Golz, A. J Krmpot, M. D Rabasovic, J. Petrovic, V. Asgekar, B. Faatz, F. Tavella, A. Perucchi, S. Kovalev, B. Green, G. Geloni, T. Tanikawa, M. Yurkov, E. Schneidmiller, M. Gensch and N. Stojanovic, Photon diagnostics at the FLASH THz beamline, *Journal of Synchrotron Radiation*, (2019) 26, 700-707
4. K. Wenig, M. Wieland, A. Baumann, S. Walther, A. Dimitriou, M. Prandolini, O. Schepp, I. Bermúdez Macias, M. Sumfleth, N. Stojanovic, S. Düsterer, J. Röntsch-Schulenburg, **E. Zapolnova**, R. Pan, M. Drescher and U. Fröhling, Electronic decay in a dissociating molecule: THz streaking of core-excited HCl molecules, *Structural Dynamics* (2019), 6 (3), 034301

List of Figures

2.1	Scheme of FLASH.	7
2.2	Time structure of electron bunches at FLASH.	8
2.3	Principle of electron-bunch compression at FLASH	9
2.4	Scheme of the XUV and THz sources at FLASH1	11
2.5	The layout of beamlines at FLASH1	14
2.6	The layout of the collimation and transport optics in the THz beamline	15
2.7	Transmission of CVD diamond window and Silicon	16
2.8	Transverse THz Beam profiles with Dump magnet radiation and THz undulator	17
2.9	THz Doubler principle	18
2.10	Scheme of the laser pulse doubler	20
3.1	EO crystal orientation	24
3.2	Real part of the refractive index for the laser and THz wavelengths and the electro-optical coefficient of ZnTe and GaP crystals	26
3.3	EOS detection principle in EOS	27
3.4	Sequential EOS and Spectral decoding techniques principles	28
3.5	EOSD scheme principle	29
4.1	XUV double pulse suppression measurements with a fast XUV photodiode. 1 st and 2 nd XUV pulses separated by 21 ns can be clearly distinguished during the tuning phase. The orange bars indicate the positions of the pulses for clarity.	34
4.2	Fast GMD for XUV suppression measurements	35
4.3	XUV double pulses suppression result	36
4.4	XUV Doubler pulse energy distribution after tuning	37
4.5	Correlation plot of XUV photodiode and GMD electron signal	38
4.6	The spectrum from the OPA	39
4.7	Modified spectral decoding scheme for detection of THz double pulses	40
4.8	Pulse duration of the stretched laser pulse measured by FROG	42
4.9	Spectral decoding traces for THz double pulses	43
4.10	Jitter measurement results	44
4.11	Spectral calibration	45

5.1	Photo-absorption coefficient of Silicon	49
5.2	Scheme of the experimental setup for the XUV plasma switch experiment in the refocusing mirror geometry	52
5.3	Reflectivity of the refocusing XUV multi-layer mirror	53
5.4	Filter and window transmission for XUV plasma switch experiment	54
5.5	Electron bunch current profile measurement with LOLA	55
5.6	Setup for THz and XUV 2D raster scan in the sample position	57
5.7	Result of the 2D scan and spatial overlap	58
5.8	Transient THz reflectivity change of Si in the refocusing mirror geometry	60
5.9	Scheme of the experimental setup for XUV plasma switch experiment in the THz Doubler geometry	61
5.10	2D THz and XUV beam profiles with the Doubler geometry in focus	62
5.11	The transient optical reflectivity curve for THz for Si sample measured with the THz Doubler geometry	63
5.12	Pump fluence dependence of Si	64
5.13	Schematic illustration of the tilted pulse front encoding setup	67
5.14	XUV-THz single shot arrival time measurement using the echelon mirror	69
6.1	Scheme of a Michelson interferometer	72
6.2	Schematic of the diffraction of waves on the lamellar grating	76
6.3	Calculated diffraction orders position for three different wavelengths in the THz range	77
6.4	Schematic of the lamellar grating	79
6.5	Comparison of the efficiency of the Lamellar grating interferometer to the Michelson interferometer	80
6.6	Scheme of the white light interferometer setup for the lamellar grating interferometer alignment	82
6.7	Alignment of the Lamellar grating with a red CW laser	83
6.8	White light interferometry for lamellar grating alignment	84
6.9	The white light interferometer setup for the alignment of the lamellar grating	85
6.10	Scheme of the lamellar grating Interferometer	87
6.11	Double-sided interferogram with shadowing	87
6.12	FTIR measurement for THz edge radiation with 215 μm THz band-pass filter	88
6.13	Interferogram and the corresponding spectrum from the dump magnet	89
7.1	Spectral range and pulse energies from XUV and THz Sources in FLASH1	91

List of Tables

2.1	Parameters of the THz sources at FLASH1	13
4.1	THz Doubler pulse energies after tuning	36
5.1	Si electron and hole energies	50

Contents

1	Introduction	3
2	FLASH - Free Electron Laser in Hamburg	7
2.1	Overview of FLASH	7
2.1.1	FLASH injector laser and accelerator	7
2.1.2	Electron bunch compression	8
2.1.3	SASE principle	9
2.2	Integrated THz sources at FLASH	11
2.2.1	THz transport	13
2.3	THz Doubler	18
2.3.1	Generation principle	19
3	THz Diagnostics	21
3.1	Electro-optical sampling theory	21
3.2	Balanced detection	25
3.3	Electro-optical spectral decoding (EOSD)	28
3.4	Pyro detectors	29
3.5	THz spectral filters	30
3.6	THz Streaking	30
3.7	Fourier transform infrared spectroscopy at FLASH	31
4	THz Doubler characterization	33
4.1	XUV suppression measurements	33
4.2	Jitter measurements	37
4.2.1	Modified spectral decoding scheme	39
4.2.2	Laser stretching	40
4.2.3	Choice of the electro-optical crystal	42
4.3	Experimental realization	42
5	XUV plasma switch for THz	47
5.1	Theory of ionization dynamics in semiconductors	48

5.1.1	Excitation processes	48
5.1.2	Calculation of the critical electron density for THz range	50
5.2	XUV refocusing mirror geometry	52
5.2.1	2D beam profiles and spatial overlap	56
5.2.2	Results of the temporal overlap and resolution of the method	59
5.3	THz Doubler geometry	61
5.4	Comparison to the experiment in the refocusing mirror geometry	64
5.5	Future perspectives for the single shot XUV plasma switch for THz	66
5.5.1	Tilted pulse front single shot encoding	66
6	Lamellar Grating Spectrometer	71
6.1	Fourier-transform Infrared spectroscopy	72
6.2	Lamellar Grating spectrometer	75
6.2.1	Choice of parameters	76
6.2.2	Design of the lamellar grating	78
6.2.3	Efficiency comparison to Michelson Interferometer	80
6.2.4	White light interferometer for alignment	81
6.2.5	THz beamline spectral characterization	84
7	Conclusions and future perspectives	91
A	Acknowledgements	95

Chapter 1

Introduction

Free electron laser (FEL) facilities provide photon pulses with extremely short durations, high repetition rates and variable wavelengths from X-ray to millimeter range. The combination of FELs and other photon sources of various properties in pump-probe experiments enables the fascinating study of the light-matter interaction, allows control of the properties of matter and opens the door towards better understanding of the fundamental aspects of nature. An advantage of such facilities and experiments is the possibility to access and investigate processes which happen on ultrafast time scales - within picoseconds or femtoseconds.

FLASH, the Free Electron Laser in Hamburg, is a 315m linear free electron laser located on the campus of Deutsches Elektronen Synchrotron (DESY). Its significance on the scientific arena of the world is remarkable due to the advance research in the field of accelerator development, lasers and of course in the various breakthrough scientific topics which widen the understanding of fundamental principles of nature.

The THz source at FLASH, naturally synchronized to the XUV pulses, is a unique feature of the facility. The combination of soft X-ray pulses, synchronized femtosecond near-infrared (NIR) laser with the central wavelength of 800 nm [1] and tunable (10 % bandwidth) THz at high repetition rate provides the access to large spectral range where the wavelength of the pulses can be selected almost continuously. This enables a large range of pump-probe experiments.

At facilities, which use the combination of XUV and THz pulses (for example FLASH and also in future XFEL, FERMI, and LCLS), establishing the temporal and spatial overlap between them is can be very challenging. Therefore developing new schemes, which allow to find time-overlap in the ps or fs range within a short period of time is of great importance. For the case of the temporal overlap of XUV and external laser pulses, several methods have been employed: reflectivity change monitoring of photoexcited materials, phase transitions in solids, generation of side-bands of photo-electron TOF spectra [2, 3, 4, 5]. Yet for the THz range, there are not too many techniques available.

However, the large difference in optical paths of THz and X-ray beamlines prevents utilization of the machine's full potential (e.g. extreme pulse energies in the soft X-ray range)[6]. So far the geometry with the delaying and refocusing the of the XUV pulse by a multilayer mirror

has been used. Due to the nature of the XUV radiation and limitations for the reflective optics, multilayer mirrors in this spectral range are typically designed for a narrowband wavelength range and experience up to 50% intensity loss. To solve this issue a new, so called THz DOUBLER scheme was been developed. Double electron bunches, separated by 28 periods of the driving radio frequency (at 1.3 GHz) and timed for the temporal overlap of THz and X-ray pulses at the experimental station have been used. The specific feature of the scheme is that 1st and 2nd bunches are lasing in a different way, where one produces only XUV and another one - only THz pulses. A way to suppress the XUV pulse while keeping THz present is shown in this work. In order to measure the arrival time jitter between the THz Doubler pulses a new solution, based on the electro-optical spectral decoding technique has been developed and commissioned.

THz, being one of the most challenging to study ranges in the electromagnetic spectrum, has brought a lot of research breakthroughs in the last years. There are various types of detectors available, suitable for various applications, both spectral and temporal characterization of THz pulses. This work presents an overview on the THz detection principles which have been employed at the THz beamline at FLASH and further adjusted for the characterization of 21 ns separated THz Doubler pulses.

When it comes to temporal characterization of ultra-short and very broadband THz pulses at FLASH with duration down to hundreds of femtoseconds, a lot of factors must be taken into account. The most challenging part at FLASH is the extremely broad spectral content of the pulses, which requires a detector, sensitive over the whole spectral range, including higher harmonics of the central wavelength. For some experiments ([7, 8]) it is necessary to know the shape of the electric field of the THz pulse, which requires highly sensitive scanning or single shot detection.

The main focus of this thesis is characterization of THz pulses in the THz Doubler configuration, separated by 21ns. This applies restrictions and creates challenges even for techniques which are typically used, because most of the detectors, which are used in the THz range are thermal and are sensitive on longer time scales. A few questions regarding the characterization of THz Doubler pulses for application in the experiments must be answered in this work: 1) what is the temporal jitter between the THz Doubler pulses and how to measure it; 2) what are the individual pulse energies of the THz Doubler pulses and 3) How to measure their spectrum? In order to address these questions, various types of detectors and techniques were modified particularly to fit the requirements of this work.

In this work, a new spatio-temporal overlap tool for XUV and THz pulses, based on the so-called ultrafast XUV plasma switch effect is presented. Here, the optical properties of a high resistivity silicon sample are modified by intense XUV and probed by the THz pulses. The obtained results demonstrate the feasibility of this scheme as a flexible temporal overlap tool with the precision down to the pulse duration of the probing THz pulse (in a ps range). Presented in two (refocusing mirror and THz Doubler) geometries, this is a proof-of-principle experiment for the THz Doubler scheme.

Not only the XUV plasma switch for THz can be measured with ps resolution, but by modifying the detection scheme for THz and using an additional laser for THz probing, the temporal overlap between XUV and THz can be established in a single shot way with the precision in the range of one period of the THz pulses. With the further development of this technique it will be possible to study the properties of materials in the excited states in a single shot fashion.

Knowing the precise spectral content of the radiation used in the experiment is crucial. For the THz source at FLASH it becomes especially challenging because of its extremely broadband spectral range. The limited amount of the beamtime is another important factor. In order to fulfill these requirements, a novel Fourier transform spectrometer, based on the lamellar grating technology was developed. It is a robust and extremely efficient device, suitable for the broad spectral range of FLASH. The high efficiency of the lamellar grating spectrometer is beneficial both for the purpose of the source characterization, studies of nonlinear effects as well as in biology, astrophysics and industry.

This thesis is divided into 5 major chapters:

Chapter 2: Theoretical background focuses on the working principle of free electron lasers, the parameters of the electron bunches, tuning procedure, as well as on the THz generation and typical characterization techniques. Schematic of the beam delivery at FLASH, together with the overview of the THz beamline, XUV and THz transport are also covered there. The novel THz Doubler scheme, generation principle of electron bunches, separated by 21.5 ns are concluding this chapter.

Chapter 3: THz Diagnostics gives theoretical overview on the techniques used in this thesis for characterization of the THz Double pulses.

Chapter 4: THz Doubler characterization presents the experimental results of the new scheme for the temporal jitter characterization of the 21.5 ns separated THz pulses and XUV suppression measurements.

In the **Chapter 5: XUV plasma switch for THz**, the novel XUV plasma switch technique is described. It includes an overview on the ionization dynamics of silicon, theory of the free electron plasma and the experimental realization. The experimental part includes three schemes: the refocusing mirror, the THz Doubler and the single shot geometry.

Chapter 6: Lamellar grating Spectrometer focuses on the spectral characterization of THz pulses at FLASH. It includes the theory about Fourier-transform infrared spectroscopy, generation of an interferogram, Michelson and lamellar grating interferometer working principle. The parameters and alignment procedure of the lamellar grating spectrometer, as well as the first commissioning results are presented.

Chapter 2

FLASH - Free Electron Laser in Hamburg

2.1 Overview of FLASH

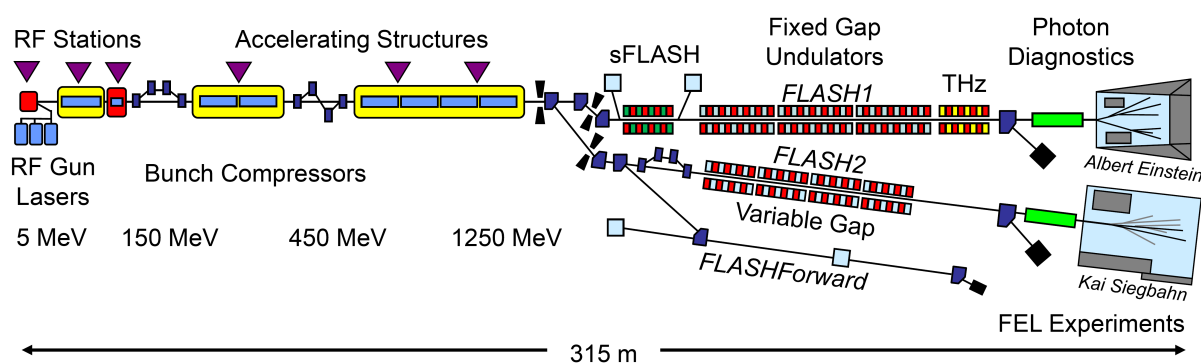


Figure 2.1: Scheme of FLASH. Layout of the main components: injector laser, accelerator, undulator beamlines and experimental halls of FLASH1 and FLASH2

The working principle of FLASH has been described in great detail in many dissertations and publications over the last decade [9, 10, 11]. This chapter will focus on the parts of the machine, which are of the highest importance for the work presented in this thesis ([12, 10, 13, 14]).

The essential components of FLASH are the injector laser, photo-cathode, the linear accelerator (LINAC), undulators section and the experimental hall, which are presented on the Fig. 2.1 [15]. Here the parameters of the machine, which are the most critical for the scope of this work are covered: on the generation and manipulation of electron bunches, on the XUV and THz photon pulses, and the THz detection schemes [16].

2.1.1 FLASH injector laser and accelerator

The very first step in the operation of any FEL is the generation of electrons via illuminating the photo-cathode with laser pulses. The cathode material at FLASH is Cs_2Te , illuminated with

UV pulses with 250-270 nm wavelength for efficient electron generation. The injector laser, originally lases at 1047 nm and utilizes two frequency-doubling stages with BBO and LBO crystals, which converts the wavelength to the 262 nm wavelength at which the laser is constantly working cite 2011 [14]. The laser oscillator produces pulses with 54.16 MHz frequency, which is synchronized to the 24th sub-harmonic of the radio frequency (RF) field, which is also used for accelerating the electrons at the next steps.

In order to accelerate the electron bunches to relativistic energies an alternating electromagnetic field is applied. The linear accelerator (linac) in FLASH is superconducting and consists of the TESLA type modules, made of niobium and cooled by superfluid helium of 2K and accelerates the electrons up to 1.25 GeV [17]. At FLASH, the 1.3 GHz RF frequency is used as the main driving frequency. The injector laser is externally synchronized to the RF frequency via optical synchronization down to sub-10 fs level [18].

At FLASH, the electron bunches are generated in bursts coming with 10Hz repetition rate. Each burst consists of bunch trains up to 800 μs length with up to 1MHz internal repetition rate. Currently, maximum number of bunches pro pulse which can be accelerated with these conditions is 800 (see Fig. 2.2)[13] .

The parameters of the driving laser pulses determine the properties of the electron bunches, such as duration, charge, distribution in time and emittance, which directly influence the properties of the generated photon pulses.

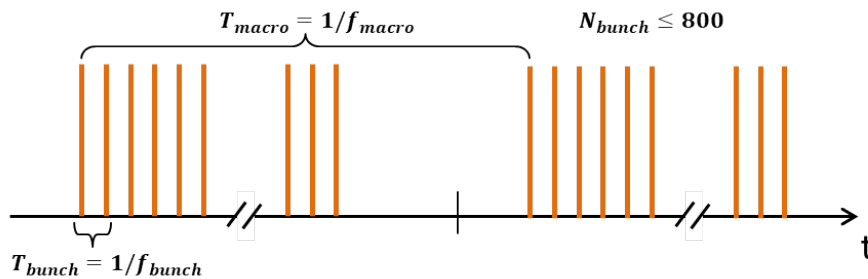


Figure 2.2: Time structure of electron bunches at FLASH. Macro pulses are delivered with 10Hz repetition rate, while the electron bunches within the macro pulse can be delivered with the repetition rate up to 1 MHz, filling the 800 μs time window, allowing maximum 800 bunches pro macro pulse.

2.1.2 Electron bunch compression

One of the important parameters for the THz Doubler scheme is the compression of the electron bunches, as it is one of the ways of the manipulation of the electron bunch parameters separately for each bunch. Electron bunches with the peak current of few kA are required at FLASH for generation of XUV pulses, but such currents can not be transported far because of the high space-charge forces, which would destroy the bunch within a very short distance. Therefore bunches at lower current of 50A are generated by the photocathode and later compressed with

magnetic chicanes. For compression, the adjustment of the phases between laser and the RF gun is critical [13].

Electrons are accelerated on the sinusoidal slope of the RF wave. This creates the chirp on the bunch: the electrons in the front have higher velocity than those in the tail. When going through the magnetic chicane, the electrons on the back are travelling a shorter path in comparison to those in the front of the bunch. Therefore, in the ideal case, the outcome of the suppression is a narrow-line shaped electron bunch. With the current configuration of FLASH it also has a spike which is carrying most of the charge. Depending on the phase between the electron bunch and the RF field the result of the compression can be more or less linear, leading to different compression conditions. Normally the phase precision lies in the range of less than 1° and sometimes even about 0.1° [14]. Therefore even small offset of phase might affect the bunch shape a lot. The electron bunch compression principle is shown on the Fig. 2.3, where δp is the deviation of the momentum of the electron with respect to the reference momentum p .

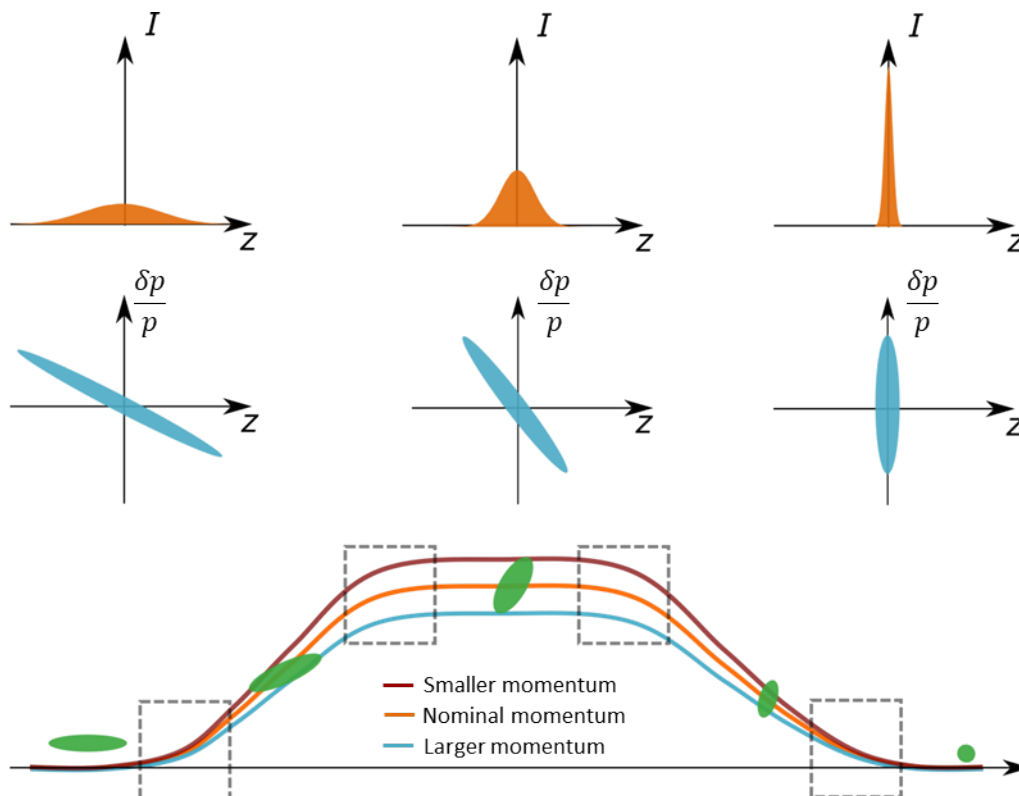


Figure 2.3: Principle of electron-bunch compression at FLASH. Electrons with smaller momentum travel longer path while those with higher momentum travel a shorter path, resulting in the longitudinal bunch compression. Adapted from [12]

2.1.3 SASE principle

After acceleration to relativistic energies and compression, electron bunches enter the undulator section where the generation of XUV radiation is initiated. FLASH is a unique facility, utilizing

simultaneous operation of three FELs. The electron bunch train is split with a fast kicker magnet (a magnet, which rapidly switches on and off, hence deflecting the electron beam from its original trajectory by the influence of the magnetic field) into two parts such that electrons are shared between FELs [16]. Both parts operate at the full repetition rate of 10Hz repetition rate and have independent repetition rate within the bunch train. The test seeding variable gap undulators in the sFLASH section are also capable of working in parallel to FLASH1 and FLASH2 [19].

Undulators at FLASH1 are periodic magnetic structures with certain parameters, dedicated for generation of XUV and THz radiation. The period of the undulator is normally much smaller than its length, $\lambda_u \ll L_u$. The XUV undulators at FLASH1 have length of $L_u = 27m$ with the period of $\lambda_u = 27.3mm$ and the peak magnetic fields of $B_u = 0.4T$. Relativistic electrons, travelling with a curved trajectory through the periodic magnetic field emit photons with the wavelength λ :

$$\lambda = \frac{\lambda_u}{2\gamma^2} \left(1 + \frac{K_u^2}{2} \right), \quad (2.1)$$

where $K_u = \frac{eB_u\lambda_u}{2\pi m_e c_0}$ is the undulator parameter, c_0 is the speed of light in vacuum and $\gamma = 1/(\sqrt{1 - (v/c_0)^2})$ is the Lorentz factor and v is the speed of a relativistic electron. FLASH1 is equipped with the fixed gap undulators, therefore the tuning of the wavelength is done by changing the energy of the electron beam:

$$W = \gamma m_e c_0 \quad (2.2)$$

The tunable wavelength of XUV pulses at FLASH1 lies between 4.2 nm up to 52 nm (295 eV to 23 eV). FLASH2 has the variable gap undulators installed which allow the possible tunable range of XUV wavelength between 4 nm and 90 nm (309 eV and 13 eV) [16]. Variable gap undulators allow for the tuning of the XUV wavelength without changing the electron beam energy and can be done during the beamtime within a short time. This feature offers a higher level of flexibility for experiments. Same scheme with variable gap undulators is also going to be implemented in FLASH1 within the FLASH2020+ upgrades [20].

The Self Amplified Spontaneous Emission (SASE) process takes place within the undulators, where the spontaneous radiation, generated by the electron bunches in the beginning of the undulator amplifies the radiation, produced along the rest of the undulators [21].

In the beginning, at the entrance of the undulators, the electrons radiate spontaneously within a broadband range of wavelengths. The beam energy and the undulator parameters, such as the current, the gap width and the length, create resonance conditions for the desired wavelength (see Eq. 2.1). Within the undulator, the emitted photons interact with the same electrons in each period of the undulator, hence slowing down electrons with higher energies and accelerating those with lower energy. Affected by this process, the electrons in the bunch are eventually

concentrated into periods, also called microbunches. The microbunches emit with high level of coherence and their energy grows exponentially along the undulators. At the point when microbunches are fully developed there is no more growth of energy and the saturation regime is reached. [21]

Besides the fundamental wavelength λ_0 of XUV, typically there are also higher odd harmonics ($\lambda_3 = \lambda_0/3$) present, therefore expanding the spectral range into much shorter range - down to 1.7 nm. The intensity of the 3rd harmonic is much lower than the fundamental wavelength (0.5%), but it has been nevertheless successfully used in the user experiments [22, 23, 24].

An alternative way of achieving high photon pulse energies at FELs is the so-called seeding technique. On contrary to SASE process, where radiation is amplified from the shot noise of the electron bunch, in the seeding technique electron bunches are shaped by an external coherent photon source before entering the undulator. The seeding photon beam can have different wavelength, depending on the configuration of the FEL and the final generated FEL wavelength. As an example, the seeding branch of FLASH, the sFLASH (see Fig. 2.1), employs photon beam in the UV range at 38 nm, by using a high harmonic generation (HHG) [25]. At FERMI, the high gain harmonic generation (HG) is used. In this case the electron bunch is modulated by laser pulses with 267 nm wavelength and additionally shaped by a tunable undulator [26]. Seeding techniques deliver pulses of higher coherence than those produced by SASE process only, but achieving high repetition rates as well as high pulse energies of the HHG sources is challenging.

2.2 Integrated THz sources at FLASH

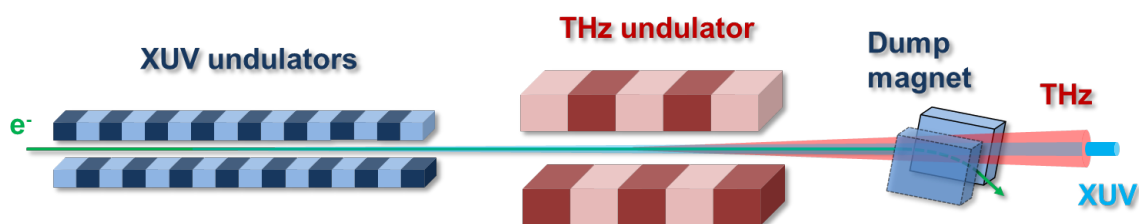


Figure 2.4: Scheme of the XUV and THz sources at FLASH. THz undulator and the electron dump magnet are located after the main XUV undulator section. Electron beam (green) first goes through the XUV undulator, generating XUV photons (purple), and then travels through the THz undulator, producing the multi-cycle THz pulses (red). Afterwards the electrons are dumped into the electron beam dump, creating a fan of photons with a broadband spectrum in the forward direction. Adapted from [27].

The worldwide unique feature of FLASH is the combination of high-repetition rate and brilliant XUV pulses with tunable and synchronized THz pulses of high intensity.

After the main XUV undulator section electrons go through the THz undulator and generate pulses with wavelengths in the THz range. Behind the THz undulator the electron beam dump

magnet separates electrons from photons, which go further to the photon diagnostics and the dedicated beamlines (see Fig. 2.4) [9].

The THz undulator at FLASH1 is a planar electromagnetic undulator with 9 full periods 40 cm long, 2 correction coils with 1/8 and 1/2 turns of a full coil (together acting as 1 full period the undulator) and with the undulator gap of 40 mm [28]. By changing the current of the magnets, the magnetic field can be manipulated, which influences the radiation, emitted by the relativistic electrons passing through. The pulse energy of the THz pulses depends on the electron beam energy and charge, the desired central wavelength and the beamline transmission. It takes a lot of expertise and careful tuning from the operators to achieve high pulse energy for experiments where both XUV and THz are used. THz pulse duration varies depending on the spectral content of the THz pulse and can be roughly estimated as $\frac{10 \times \lambda_{THz}}{c}$, where λ_{THz} is the central wavelength [9]. Due to movement of the electrons in the undulator in horizontal plane, the generated radiation is linearly polarized. The wavelength can be tuned from 1 μm and up to 300 μm with the spectral bandwidth of $\frac{\Delta\lambda}{\lambda} \sim \frac{1}{N_u} = 10\%$, where N_u is the number of undulator periods.

THz undulator has the maximum K_{max} value of 49 [29], which means that a lot of higher harmonics down to optical range are present. The presence of harmonics can be explained by considering the angle of the emitted radiation with respect to the travel axis of the electrons to be

$$\theta \approx \frac{K_{max}}{\gamma}, \quad (2.3)$$

which for high values of K is larger than the cone of the fundamental wavelength $\theta_0 \sim \frac{1}{\gamma}$ [21].

If a detector is placed on the main axis of the electron trajectory at a large distance from the undulator it detects only the fundamental radiation, emitted in the cone of θ_0 . In the undulator with a high K value the electrons have an angular trajectory, therefore the detector will see the light only when it comes within the angle θ_0 . The electric field profile in this case is spiky in alternating directions and the corresponding spectrum of it consists of the fundamental frequency and the higher harmonics. The even harmonics cancel each other on the detector, because their signal is symmetric and uniformly spaced, therefore only odd harmonics can be measured. If the detector is located off axis at an angle $\theta > 0$, then even harmonics are no longer equally spaced and can be detected [21].

The wavelength of m_{th} harmonic can be presented as follows:

$$\lambda_m = \frac{1}{m} \frac{\lambda_u}{2\gamma^2} \left(1 + \frac{K_u^2}{2} + \gamma^2 \theta^2 \right), m = 1, 2, 3, \dots \quad (2.4)$$

Due to the transport of THz through the beamline via gold-coated reflection coatings, the wavelengths shorter than 500 nm almost do not reach the experiment [27]. The transport of the THz beamline is described in details in the following section 2.2.2

Another source of THz radiation at FLASH1 is the dump magnet, which separates the electrons from the photon beam. After the undulators, electrons travel in the free space until they enter the magnetic field of the dump magnet and there they experience an abrupt change in the longitudinal velocity. This process leads to the generation of a single cycle radiation in the forward direction, so called dump radiation. [9]. As the electrons are going in a bend trajectory of the full 21° curve, only the fan of radiation within the 2.4° in the forward direction is fitting the dimensions of the vacuum pipes and can be transported to the experiment [27]. The produced photon pulses are single cycle with the broadband spectrum and the pulse energies up to $10\mu J$ [30], both depending on the electron bunch parameters, i.e. tuning of the machine.

The radiation from the dump magnet is generated at FLASH all the time when there are electrons present at FLASH, regardless whether THz undulator is switched on or off.

The summary of the parameters of the THz radiation, delivered to the experiment in FLASH is presented in the Table 2.1:

	Undulator	Dump magnet
Intensity	$\leq 150\mu J$	$\leq 10\mu J$
Bandwidth	10 %	100 %
Polarization	Linear	Radial
Pulse shape	10 Cycles	Single cycle

Table 2.1: Parameters of the THz sources at FLASH1

2.2.1 THz transport

THz beam has a significantly larger divergence and beam size than the XUV beam due to the difference in wavelength and source properties [6]. Its divergence depends on the wavelength and the properties of the source (electron bunch). The THz beamline is designed in a way to keep the THz beam within the size of the beam-transport optics. For this purpose, reflective toroidal mirrors which fold the beam at 90 degrees (45 degrees incidence) angle are used [27].

After 7.7 m from the edge of the THz undulator a plane gold coated mirror M1 with a 10 mm aperture in the center separates the THz and XUV beams (see Fig. 2.6). THz is reflected at 45 degrees and XUV passes straight through the hole. In order to keep the size of the divergent THz beam within the dimensions of the beamline the beam is re-collimated several times with the reflective parabolic and toroidal mirrors. After the collimation, the beamline vacuum is separated from the laboratory environment and air by a diamond window and THz is directed into the distribution section of the beamline, and then to the experiment in the FLASH1 hall, where XUV and THz beams are recombined [27]. Along the distance from the dump magnet until the THz hutch 7 plane and 6 toroidal mirrors are installed for transport and collimation and have $<60\%$ transmission up to $200\mu m$. The overall transmission of the beamline depends on the wavelength of the radiation and the beamsizes on the mirrors and reaches up to 80% for wavelengths between $50\mu m$ and $100\mu m$. The limits of the transmission are defined by the size

of the beamline pipe for longer wavelength and by the XUV aperture on the M1 mirror, for shorter range [9, 27].

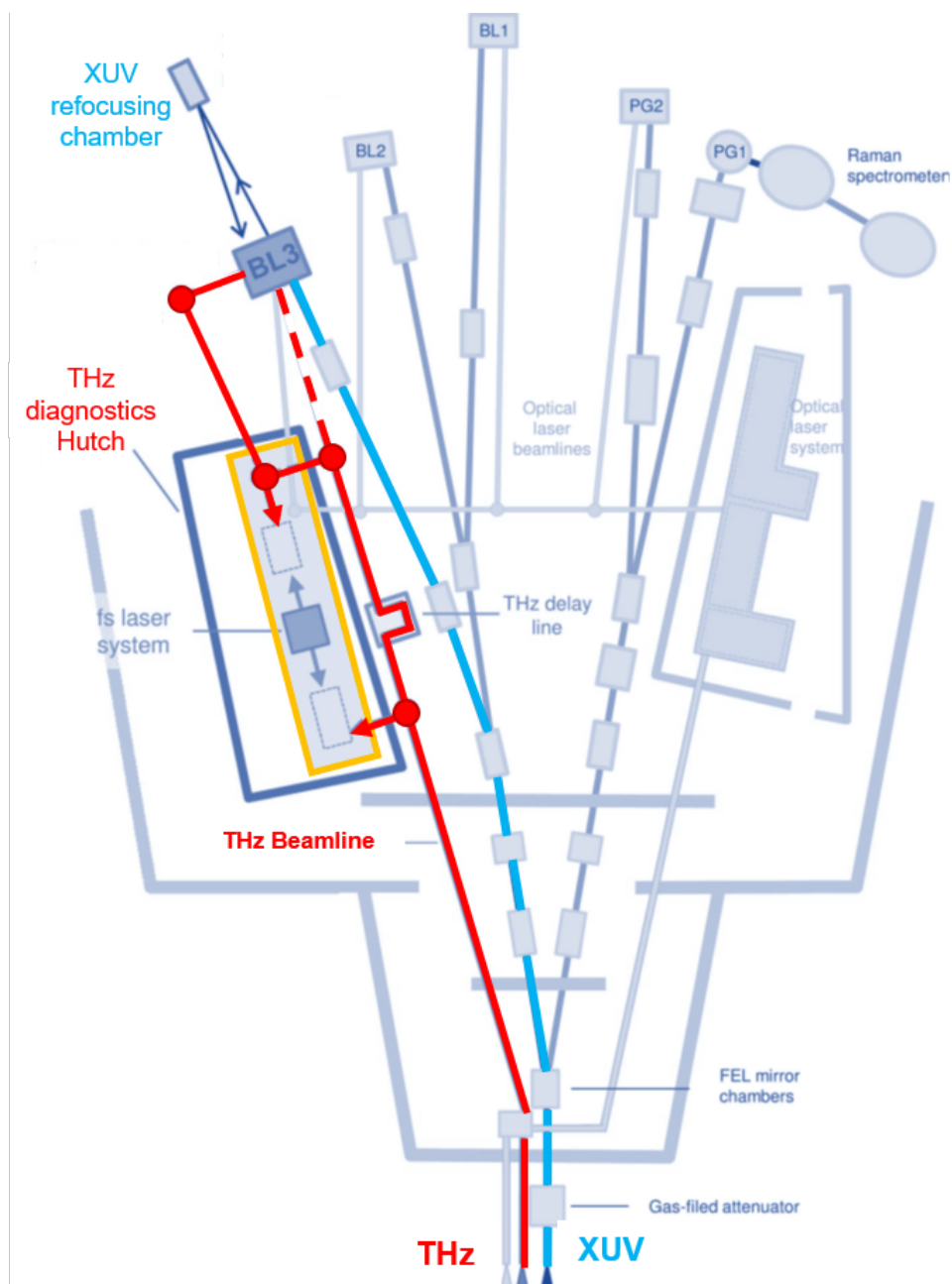


Figure 2.5: The layout of beamlines at FLASH1. THz beam is transported via the THz diagnostics hutch and further to the experimental chamber of the BL3 beamline. In the geometry with the refocusing XUV mirror, XUV passes the BL3 experimental chamber through and refocused backwards with a multilayer mirror. In the THz Doubler geometry, XUV and THz beams overlap at the experiment without refocusing of the XUV. Adapted from [27].

THz and XUV beams are separated after the electron dump magnet by a mirror (210mm x 140mm) with a 10mm aperture for the XUV beam [31]. Transport of the THz beam into experimental hall over the distance longer than 70m requires multiple focusing optics to collimate the beam. Metal coated reflective mirrors are used for this purpose. The reason for the reflective

mirrors (e.g. gold coated) is because of the broad spectral content of the THz beam, which can not be transported with transmission optics without losing the temporal structure of the pulse. The layout of the beamlines of the FLASH1 hall is presented on the Fig. 2.5.

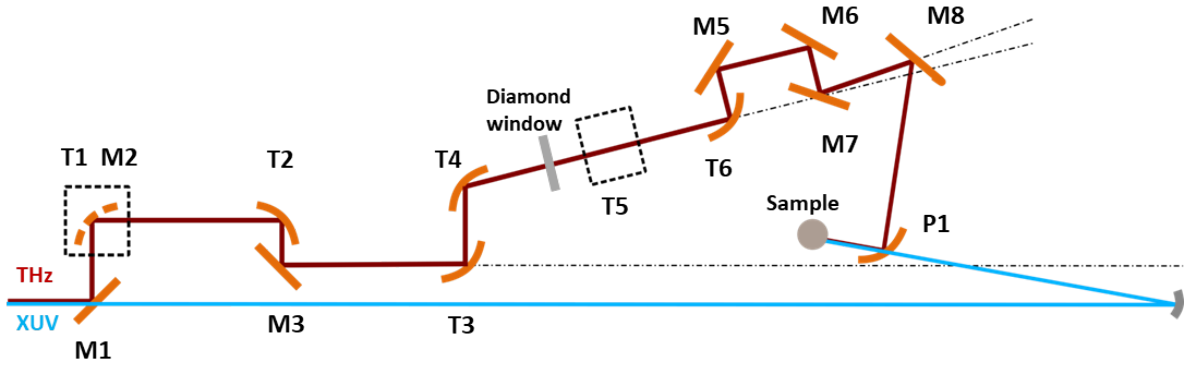


Figure 2.6: The layout of the collimation and transport optics in the THz beamline. First plane mirror M1 with a 10mm hole separates XUV and THz beams: XUV passes through further to the photon diagnostics and the experimental hall and THz beam is reflected for initial collimation. 6 toroidal (T1 - T6) mirrors with specifically chosen parameters and total 8 plane (M1-M8) mirrors installed at 45° incidence angle transport the THz beam to the THz hutch ports.

The dimensions of the collimation optics can be estimated from the ratio between the size of the beam in its waist ω , the wavelength λ and the divergence angle θ . Considering the Gaussian shape of the beam, this ratio can be written as following:

$$\theta = \frac{\lambda}{\pi\omega} \quad (2.5)$$

which means that to maintain the beam with long wavelength collimated, a larger beam size is required.

In order to separate the accelerator vacuum from the beamline vacuum, the $650 \mu\text{m}$ thick CVD (chemical vapor deposition) diamond window from "Diamond materials" is used. Diamond has a lot of unique properties, among which are 1) good transmission along a broad THz spectral range with just a few absorptions in the range between $2.5 \mu\text{m}$ and $6\mu\text{m}$. [32] (see Fig. 2.7 (blue curve) and 2) highest thermal conductivity and 3) lowest thermal expansion coefficient among other materials, which makes it a perfect material for transporting high-power beams.

To transport the THz beam through the window in the most efficient way, the beam is focused (2σ of the beam is $< 10 \text{ mm}$) [9] on the window between toroids T4 and T5, therefore reducing the possible losses on cutting the beam. The pulse energy through the diamond window is reduced by 30 % due to the reflection losses.

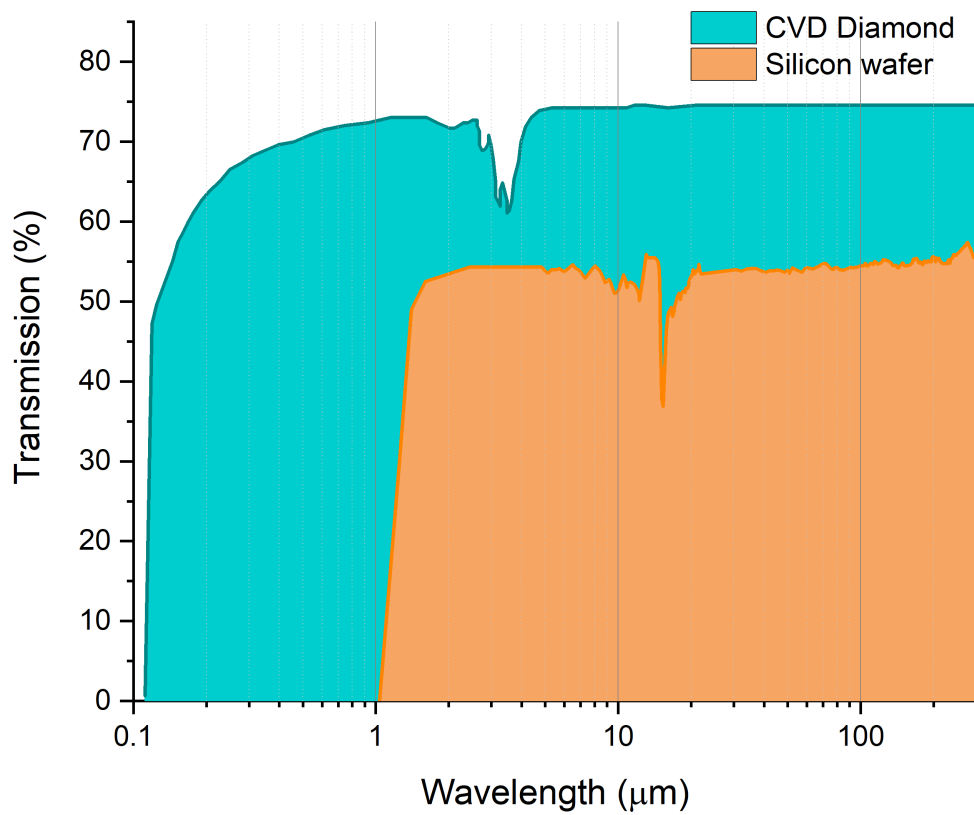


Figure 2.7: Transmission of 650 μm thick CVD diamond window from "Diamond Materials" (blue) and high resistivity 300 μm thick Silicon from "CrysTech" in the THz range (orange)

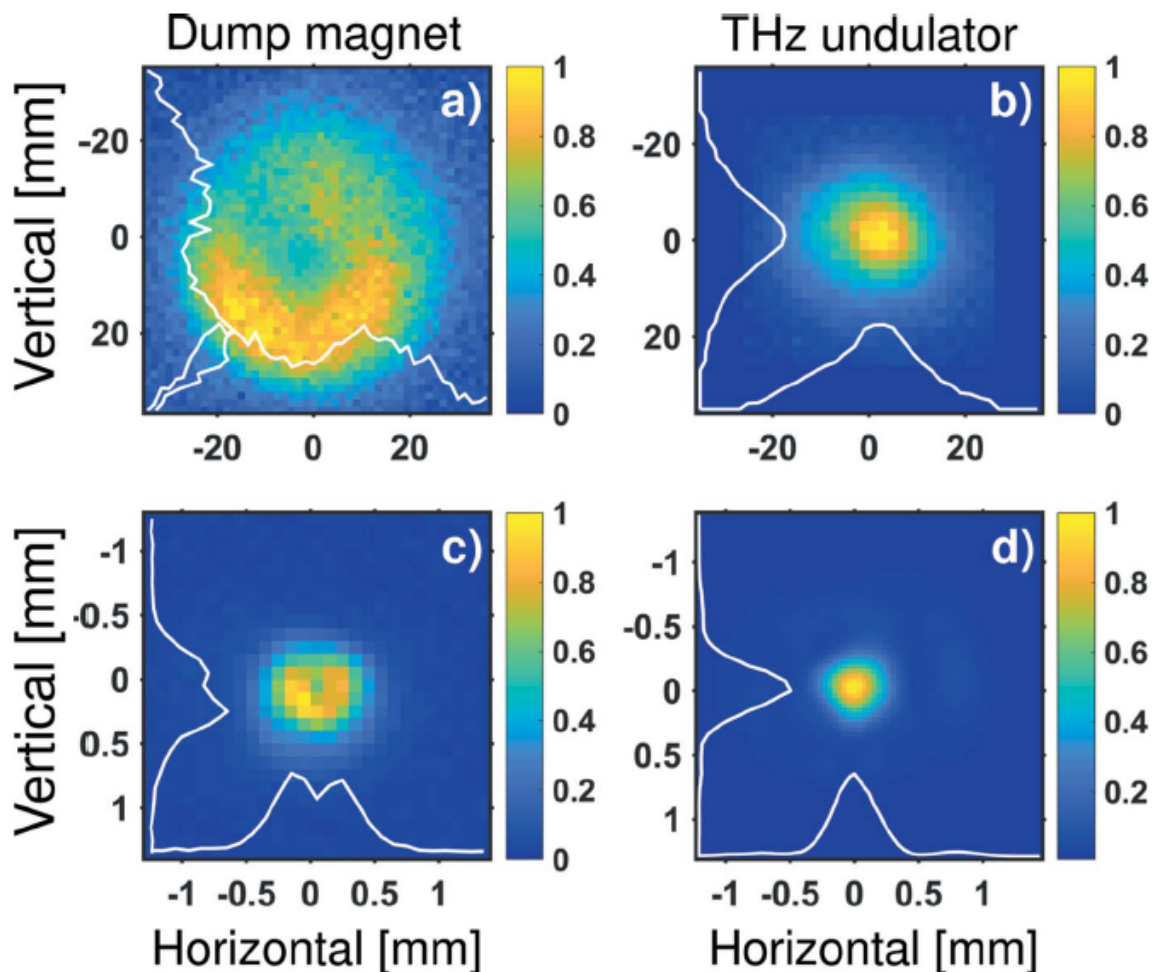


Figure 2.8: Transverse THz Beam profiles with Dump magnet radiation and THz undulator. Unfocused (a) dump magnet and (b) THz undulator beams at $88 \mu\text{m}$ (3.4 THz), measured at the THz hutch in air, focused (c) dump magnet and (d) THz undulator beams. Image from [27].

The examples of the measured THz beam profiles generated from the dump magnet and the undulator tuned to $88 \mu\text{m}$ (3.4 THz) for both collimated and focused beams are presented on the Fig. 2.8 The beam from the dump magnet has a specific 3/4-donut shape with lower intensity in the center while the beam from the undulator has a profile close to Gaussian. At normal experimental conditions these two beams overlap with each other.

In the THz hutch, additional mirrors and optics are installed, which enable to switch the beam between the THz characterization tool in the hutch and the experimental setup in the FLASH hall. THz beamline is additionally equipped with 2 delay lines for variable delay, which gives the total adjustment range for experiments in the FLASH hall of 2ns.

2.3 THz Doubler

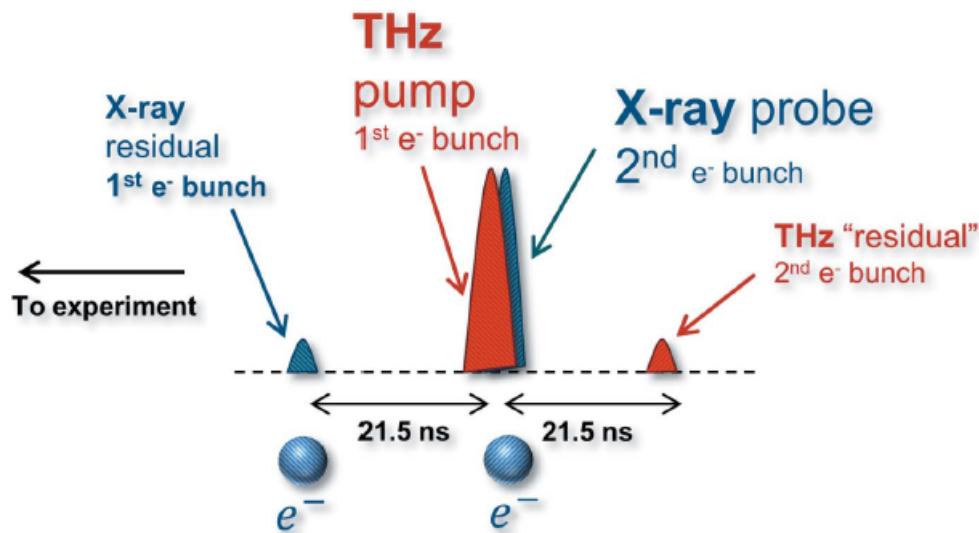


Figure 2.9: THz Doubler principle: Schematic representation of the XUV and THz pulse arrival times for doubler electron bunch scheme. The electron bunches are separated by 21.5 ns, and the corresponding generated THz and XUV pulses from the 1st and 2nd electron bunches respectively temporally overlap in the experiment.

Due to multiple reflections of the THz beam along the beamline, optical delay between THz and XUV beams is introduced. Although THz and XUV pulses are produced by the same electron bunch and have almost no jitter between each other there are still limitations for the experiments due to optical path differences.

The XUV beam is distributed to the FLASH beamlines by switching the plane mirrors at the incidence angles of 2° or 3°, depending on the beamline [33]. Silicon or ZERODUR substrate mirrors with high-density carbon coating at small incidence angle are chosen in order to achieve the highest reflectivity of the wavelength of the FLASH's XUV spectral range and low possible damage due to high pulse energies. Beamline BL3 is used for the most of the XUV-THz pump-probe experiments. The beam is transported to the experimental hall via 4 plane mirrors at the maximum incidence angle of 3° and has 2 schemes: providing the unfocused XUV beam to the experiment or focused by an elliptical mirror with 527 mm focal length.

The total difference in the optical path for XUV and THz at the experiment is 7 m (21 ns) for the current experimental setup as described in [27]. One solution to compensate this difference is to delay the XUV pulse by additional 7 m by refocusing it with a multilayer mirror with a focal length of 3.5 m backwards to the experiment. The mirror reflects the beam almost at the normal incidence angle and is specially designed for the geometry of each experiment [27, 4, 34].

Although this scheme was successfully implemented in the recent experiments at THz beamline, there are several drawbacks which limit the possibility for performing experiments

with the full potential of FLASH in terms of high intensity XUV pulses. Besides the limitation of the multilayer mirror design, this geometry also suffers from a large focal size of the X-ray beam ($>100 \mu\text{m}$ FWHM), caused by the large focal length (3.5 m) determined by the difference in optical path between THz and X-ray pulses. Reduction of the X-ray fluence in the experiment due to the combined effect of low reflectivity and large focus excludes high-intensity experiments (e.g. plasma physics [35]) or non-linear multiphoton ionizations [36] thus reducing FLASH's high pulse energy advantage over other sources in the same spectral range [6, 37, 38].

The newly planned and accepted upgrade project FLASH2020+ [20] includes the replacement of the fixed gap XUV undulators for FLASH1 with variable gap undulators. Variable gap undulators enable the rapid change of the wavelength during the experiment without significantly changing the electron beam energy and re-tuning of the machine. Combined with THz pulses, this feature will allow for the investigation of material properties (for example in the Si K edge at 1.8 keV) in a scanning wavelength fashion [39]. In this case the intrinsically narrowband XUV multilayer mirrors would become a limitation for such studies.

Another solution for the challenge of difference in the optical path for XUV and THz, is to generate two consecutive electron bunches, producing THz and XUV pulses such that the pulses overlap temporally in the experiment. The so-called THz Doubler scheme is presented in the Fig. 2.9. Both electron bunches naturally produce XUV and THz radiation. For typical THz pump/X-ray probe experiments the first electron bunch needs to be optimized to generate maximal THz pulse energy (refer to scheme in Fig. 2.9), while generating little or no X-rays, to reduce their potential influence on the sample. The second bunch, on the other hand, should be optimized to generate X-ray pulses with required properties, ranging from short pulse duration to high pulse energy, while suppressing the THz output (although this is less critical, because the 2nd THz pulse arrives later than the actual measurement and does not contribute in the pump-probe experiment) [6].

The concept of the double pulse generation at FLASH (THz Doubler) has been originally introduced in earlier research at FLASH by [29].

2.3.1 Generation principle

Electron bunches at FLASH are generated by the electron gun. Picosecond laser pulses irradiate the Cs₂Te photocathode and generate short electron packets that are further accelerated via the alternating RF field and shaped in the accelerator. The laser system operates at 1047 nm and its 4th harmonic at 262 nm is used to drive the electron emission of the photocathode.

The fourth harmonic of the driving photocathode laser, at 262 nm, is split by a polarization beamsplitter (fused silica at the Brewster angle). One of the branches is delayed by 21.5 ns with the option to fine-tune the arrival time of the second pulse via a delay stage (e.g. for adjusting it to the phases of the accelerating modules).

Double electron bunches for the THz Doubler have been set up following the procedure described by [29] and presented on the Fig. 2.10.

Divergence and beam size resulting from the difference in optical path are compensated by a Keplerian telescope. The two beams are recombined by a second polarization beamsplitter and brought together at a photocathode. Each of the pulses can be blocked by closing the corresponding shutter.

When it comes to the electron bunch tuning, such parameters as compression, charge and orbit of the electron beam influence the outcome of the pulse energy of the XUV beam the most. By changing the intensity of the injector laser via apertures or by adjusting the transmission through polarization sensitive optics, the charge of the electron beam can be manipulated. The compression of the electron beam can be adjusted by changing the relative arrival time (or the phase) of the injector laser with respect to the driving RF frequency. It is further shaped by magnetic chicanes. As different portion of the electron bunch is facing different section of the slope of the accelerating sinusoidal RF field, therefore experiencing different acceleration, which leads to a reshaping of the electron bunch temporal (current) profile. By manipulating the phase of the first bunch of the THz Doubler it is possible to reduce its lasing of XUV.

The orbit of the electron beam in the undulators plays an important role in tuning. If the position of the electron beam is offset with respect to the main axis of the undulators, the SASE process is disturbed due to the misalignment of the electrons with respect to the amplifying SASE beam. These changes are sensitive in a small range of $\sim 100\mu m$. Therefore, the gain of the XUV intensity is reduced. THz undulator is less sensitive to these deviations, therefore in some cases, changing the XUV intensity leads to a comparatively small changes for THz.

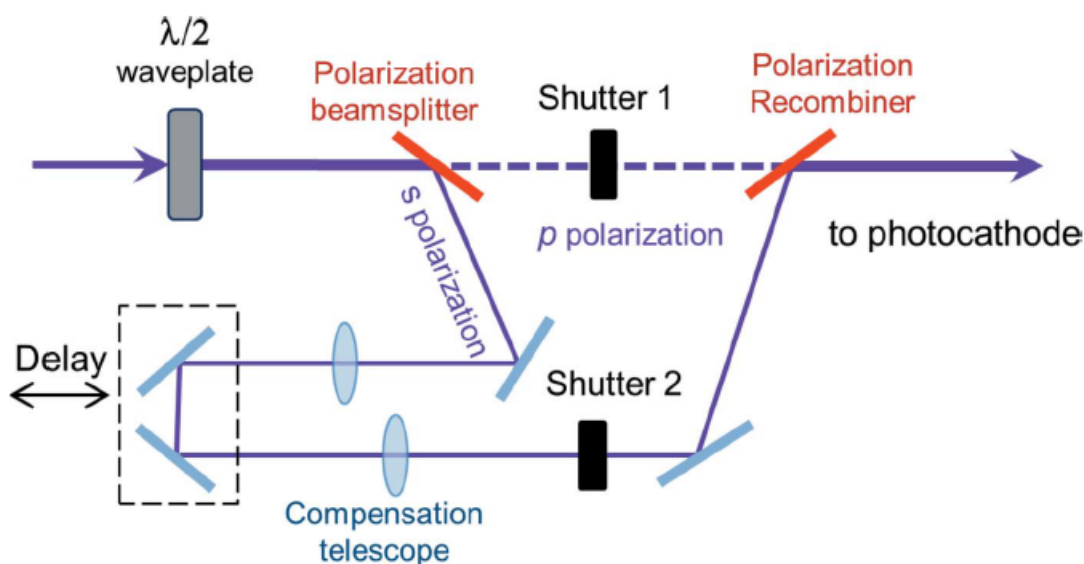


Figure 2.10: Scheme of the laser pulse doubler [adapted from [29]]. The laser pulse is split into 2 replicas: one pulse is delayed and then recombined with the direct one. Each branch includes a shutter, so that each pulse can be selected at will.

Chapter 3

THz Diagnostics

THz pulse shape can be characterized using short (less than the duration of one cycle of the THz pulse) optical laser pulses by sampling along the THz profile. Electro-optical sampling (EOS) method, based on the THz dependent modulation of the polarization of the non-centrosymmetric crystals (Pockels effect) is very commonly used. At FLASH it serves two purposes: 1) to measure the full temporal profile of the THz pulse and 2) for measurement of the arrival time jitter between the external laser in the hutch and the THz pulses. The existing scheme was modified, enabling the simultaneous detection of the arrival time of two THz Doubler pulses.

3.1 Electro-optical sampling theory

The linear electro-optical effect, also called Pockels effect, describes the change of the refractive index of a material caused by an externally applied electric field. This effect can be observed only in materials which are lacking inversion symmetry for crystals [40, 10]. The refractive index can be described by the index ellipsoid, which depicts the orientation and relative magnitudes of the refractive indices:

$$D_i = \sum_{j=1}^3 \epsilon_{ij} E_j \quad (3.1)$$

where D_i is the electric displacement, ϵ_{ij} is the relative permeability and E_j is the applied electric field. The refractive index n_{ij} relates to the permeability like:

$$\eta_{ij} = \frac{1}{\epsilon_{ij}} = \frac{1}{n_{ij}^2} \quad (3.2)$$

where η is the so-called impermeability. In some crystals, the presence of an external electric field will redistribute the charges in the molecules, therefore the orientation and size of the refractive index ellipsoid will change. In this case the refractive index of the crystal becomes dependent on the external electric field.

Expanded with the Taylor-expansion the impermeability can be expressed like following:

$$\eta_{ij} = \eta_{ij}(0) + r_{ijk}E_k + s_{ijkl}E_kE_l + \dots \quad (3.3)$$

From the equation (3.3) Pockels r_{ijk} and Kerr s_{ijkl} coefficients are obtained, which describe effects induced by the external electric field in the crystal. For crystals which are normally used in electro-optical sampling the typical values for Kerr coefficient s_{ijkl} lie in the range 10^{-21} to $10^{-14} \frac{m^2}{V^2}$, and the Pockels coefficients r_{ijk} : from 10^{-12} to $10^{-19} \frac{m}{V}$. The Kerr coefficients are significantly smaller than the Pockels coefficient in such crystals as GaP and ZnTe, which are used in this work and therefore can be neglected and will not be considered in the further discussion.

In the absence of the external electric field $E = 0$ the principal axis system of the crystal is presented as:

$$\eta_{ij} = \begin{pmatrix} \frac{1}{n_{11}^2} & 0 & 0 \\ 0 & \frac{1}{n_{22}^2} & 0 \\ 0 & 0 & \frac{1}{n_{33}^2} \end{pmatrix} \quad (3.4)$$

The crystal symmetry defines the number of independent elements and in case of ZnTe and GaP, there is only one independent element which is non-zero $r_{63} = r_{52} = r_{41}$. Therefore the Pockels effect coefficient for the ZnTe, GaP and generally the cubic $\bar{4}3m$ crystal group looks like:

$$r_{ijk} = \begin{cases} r_{41}, & \text{if } i = j = k \\ 0, & \text{else.} \end{cases} \quad (3.5)$$

Taking the above transcription, impermeability becomes:

$$\eta_{i,j}(\mathbf{E}) = \frac{1}{n_{ij}^2}(\mathbf{0}) + \sum_{k=1,2,3} r_{ijk}E_k \quad (3.6)$$

Electric field, which is incident to the EO crystal along its [110] axis, with the angle α can be presented as:

$$E_{THz} = E_{THz} \begin{pmatrix} \frac{1}{\sqrt{2}} \cos \alpha \\ -\frac{1}{\sqrt{2}} \cos \alpha \\ \sin \alpha \end{pmatrix} \quad (3.7)$$

The field dependent impermeability tensor becomes:

$$\eta = \frac{1}{n_0^2} \begin{pmatrix} 1 & 0 & 0 \\ 0 & 1 & 0 \\ 0 & 0 & 1 \end{pmatrix} + r_{41} E_{THz} \begin{pmatrix} 0 & \sin \alpha & \frac{\cos \alpha}{\sqrt{2}} \\ \sin \alpha & 0 & \frac{-\cos \alpha}{\sqrt{2}} \\ \frac{\cos \alpha}{\sqrt{2}} & -\frac{\cos \alpha}{\sqrt{2}} & 0 \end{pmatrix} \quad (3.8)$$

The solution of the equation (3.8) is presented in the following literature [10, 40]. In this work, the emphasis is made on the results of these calculations for finding the modified refractive indices $n_{1,2,3}$:

$$n_i = \frac{1}{\sqrt{\lambda_i}} \quad (3.9)$$

In normal conditions $r_{41} E_{THz} \ll \frac{1}{n_0^2}$, therefore

$$n_1 = n_0 + \frac{n_0^3 r_{41} E_{THz}}{4} (\sin \alpha + \sqrt{1 + 3\cos^2 \alpha}) \quad (3.10)$$

$$n_2 = n_0 + \frac{n_0^3 r_{41} E_{THz}}{4} (\sin \alpha - \sqrt{1 + 3\cos^2 \alpha}) \quad (3.11)$$

$$n_3 = n_0 - \frac{n_0^3 r_{41} E_{THz}}{2} \sin \alpha \quad (3.12)$$

The direction of the axis, where the refractive index component n_3 is perpendicular to the crystal plane (110) and parallel to the propagation direction of the THz and the probe laser and perpendicular to the polarization direction. Therefore, the polarization of the laser cannot be affected in this direction.

Ordinary and extraordinary parts of the laser pulse propagate with different phase with respect to each other. Along the length of the crystal the beams acquire a relative phase shift, resulting in an elliptically polarized beam. For a beam with the wavelength λ_0 the phase shift is given by:

$$\Gamma = \frac{2\pi}{\lambda_0} (n_1 - n_2) = \frac{\omega d}{2c} n_0^3 r_{41} E_{THz} \sqrt{1 + 3\cos^2 \alpha}, \quad (3.13)$$

where d is the thickness of the crystal.

The phase retardation of the laser polarization Γ linearly depends on the strength of the externally applied electric field E_{THz} and the thickness of the crystal and changes with the

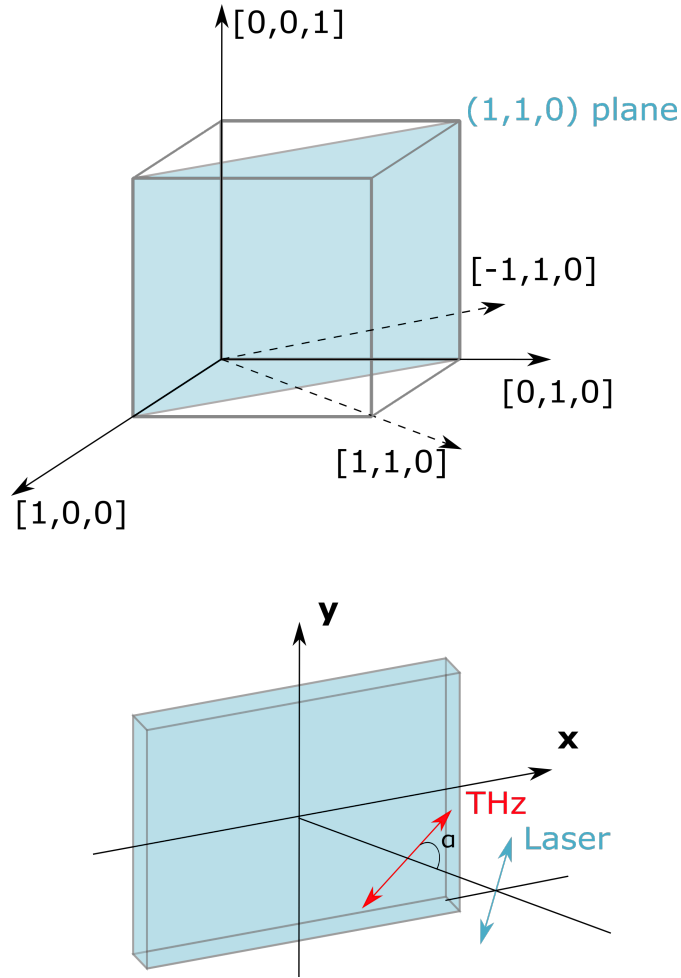


Figure 3.1: EO crystal orientation. The EO crystal is cut along the (110) plane, and lies in the XY coordinate system from the incoming THz beam perspective. THz and laser beam come perpendicularly to XY plane.

different incident angle α between the polarization of the field and the $[-1\ 1\ 0]$ axis, normal to the crystal cut plane (Fig. 3.1). Maximum phase retardation is achieved when $\alpha = 0$, when E_{THz} is parallel to the X-axis of the crystal.

In conclusion, the most effective experiment geometry to have the highest EO effect is when the THz pulse is incident to the (110) crystal cut plane and linearly polarized along $[-1\ 1\ 0]$ axis and. The retardation parameter in this situation becomes:

$$\Gamma = \frac{2\pi n_0^3 d}{\lambda_0} r_{41} E_{THz}. \quad (3.14)$$

The effect of the phase retardation of the optical probe laser depends on the relative angle between the laser polarization and the axes of the crystal. If the laser polarization is parallel to one of the crystal axes, no effect will be measured because there will be no difference induced for different polarization components. But, if the laser is polarized at any other angle to the optical axes, then its polarization can be described at the superposition of 2 polarization components

parallel to the axes of the crystal and therefore the phase retardation will make an effect and lead to the elliptical polarization.

In the ideal conditions, THz and laser pulses would propagate with the same speed in the crystal, but in reality, the refractive index is different for the optical and THz frequencies, leading to the group velocity mismatch (See Fig. 3.2) [10]. This effect leads to the laser pulse spectral broadening and to the decrease of measured signal amplitude, therefore limiting the possible time resolution. The refractive index of the ZnTe and GaP has a smooth frequency dependence in the optical and infrared range and is plotted on the Fig. 3.2 [41, 42]. ZnTe and GaP have detection limitations, which are defined by the transverse optical lattice oscillations, with resonance frequencies at 5.3 THz for ZnTe and at 11 THz for GaP, respectively [10]. Near the resonance, the refractive index is changing drastically, therefore the phase matching between the laser and the THz pulses is almost impossible to achieve. The Pockels electro-optical coefficient is also highly affected by the lattice oscillations around the resonance frequencies.

3.2 Balanced detection

When a linearly polarized laser pulse arrives at the EO crystal overlapping with the THz pulse, the laser polarization becomes elliptical. This polarization modulation can be transferred into an intensity modulation by using a combination of half- and quarter-wave plates, making it possible to use intensity sensitive detectors like photodiodes or CCD-cameras. This is the common method of retrieving the THz electric field, which is applied at various schemes and is used for both electron-bunch and the actual THz electric field profile diagnostics [43, 9, 40, 44].

Sequential electro-optical sampling (EOS) is implemented at FLASH in the THz characterization tool. EOS is used to characterize the shape of the THz electric field in a scanning fashion. A linearly polarized probe laser pulse (with a duration shorter than a cycle of the THz pulse) is overlapped with THz beam in the electro-optical crystal. The THz induces the birefringence in the crystal which leads to a change of the polarization of the laser pulse. By changing the relative delay between the laser and the THz this change of polarization is detected at each point in time. In order to measure the change of polarization the balanced detection scheme is used.

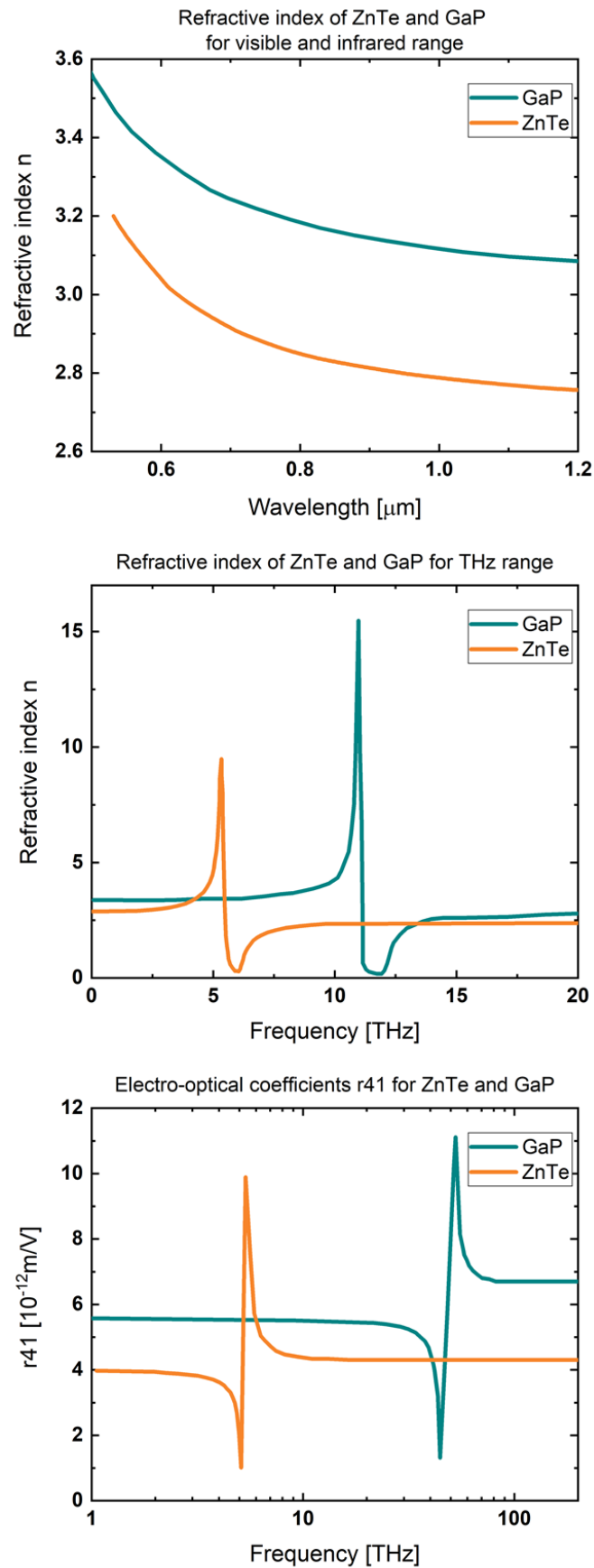


Figure 3.2: (Top) Real part of the refractive index for the laser (top) and THz (middle) wavelengths and the electro-optical coefficient (bottom) of ZnTe and GaP crystals. Adapted from [10]

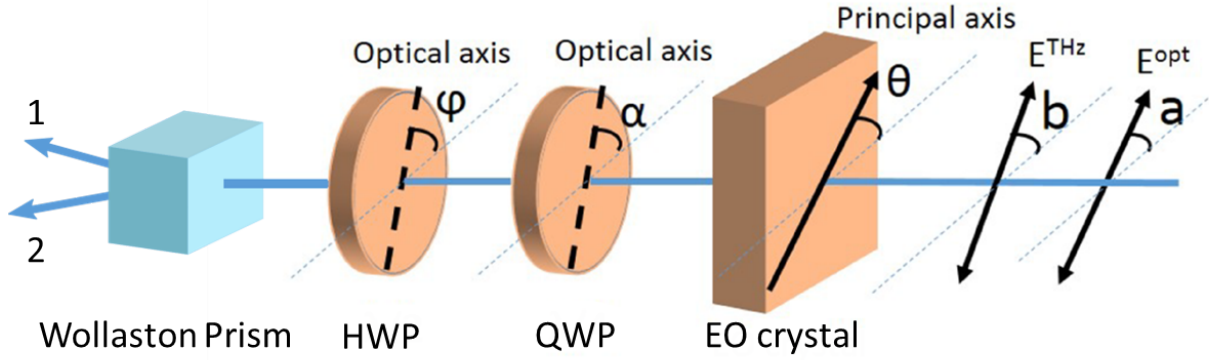


Figure 3.3: Balanced detection principle in EOS: a linearly polarized laser pulse becomes elliptically polarized after the EO crystal, Quarter (QWP) and Half (HWP) wave plates balance the signal on two identical photodiodes after the Wollaston prism. Adapted from [40]

In the balanced detection scheme by inserting a quarter-wave plate at $\phi = 45^\circ$ and the half-wave plate in a neutral position $\phi = 0^\circ$ after the EO crystal, the laser polarization becomes circular before applying THz field. The polarization components are split after the EO crystal with a Wollaston prism and sent onto two identical photo-diodes (Fig. 3.3). Without the presence of the THz field, the two polarization components are balanced with a quarter- and a half-wave plate and the signal on the photo-diodes is identical $I_{1,2} = \frac{1}{2}I_0$. In case of the temporal and spatial overlap of the laser and THz, polarization of the laser is modulated and the difference between polarization components is measured. The difference between the branches of the split pulse is background free and can be presented as:

$$I_{difference} = I_1 - I_2 = I_0 \sin \Gamma, \quad (3.15)$$

where $I_0 = \frac{\epsilon_0 c}{2} |E_0|^2$ is the incident laser intensity, with ϵ_0 being the vacuum permittivity.

The laser polarization, in the presence of the THz pulse becomes slightly more elliptical in comparison to the initial state and its ellipticity depends linearly on the THz field strength (following the equation. 3.14). By delaying the short laser pulses temporally along the THz pulse, a time-resolved measurement of the THz electric field is obtained. (The schematic representation of the balanced detection technique is shown on the 3.4(a)).

The limitation of the EOS scheme is the frequency respond of the crystal. Detection with the ZnTe crystal and 20 fs laser pulse duration provides the measurement range until 50 THz. The temporal resolution of this method is defined by the width of the scanning laser pulses and by the jitter between the laser and the THz.

3.3 Electro-optical spectral decoding (EOSD)

Although the EOS balanced detection method allows precise reconstruction of the THz electric field in theory, in the real life its resolution mainly suffers from the jitter between the external optical laser and the THz pulses from the machine. At FLASH, the optical probe laser is synchronized to THz pulses with a jitter of around 350 fs peak to peak. Therefore a second scheme is implemented and synchronized to the EOS, in order to exclude the contribution of the temporal jitter [9, 45].

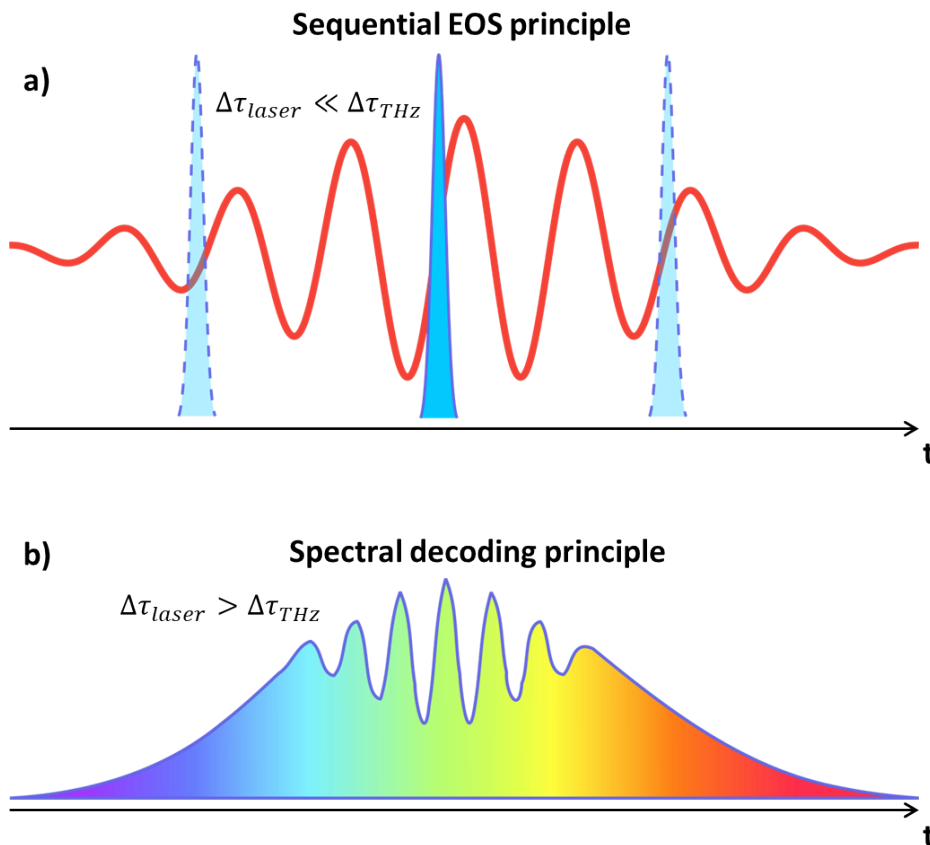


Figure 3.4: Sequential EOS and Spectral decoding techniques principles. a) Short laser pulse with the pulse duration shorter than the cycle of the THz pulse is used to measure the polarization modulation in a scanning fashion, b) whole THz pulse is imprinted on a stretched chirped laser pulse with the pulse duration longer than the pulse duration of THz.

In the spectral decoding the complete THz pulse is, in comparison to the EOS scheme, encoded on the linearly stretched laser pulse in a single-shot (Fig. 3.4 (b))[46]. The duration of the laser pulse is longer than the duration of the THz pulse. In this case, when passing through the electro-optical crystal, the laser pulse acquires modulation of polarization for different spectral components by the THz field, which is then transferred into the intensity modulation by using a polarizer. The measured signal is proportional to the electric field of the THz pulse like: $\frac{\Delta I}{I_0} \propto E_{THz}$ [46]. The intensity modulation is measured by dispersing the laser spectrum

with a grating onto a line CCD camera. Depending on the relative delay between THz and laser, different spectral components of the laser are modulated, which leads to the shift of the intensity modulation on the camera. The scheme of this technique is presented in the Fig. 3.5.

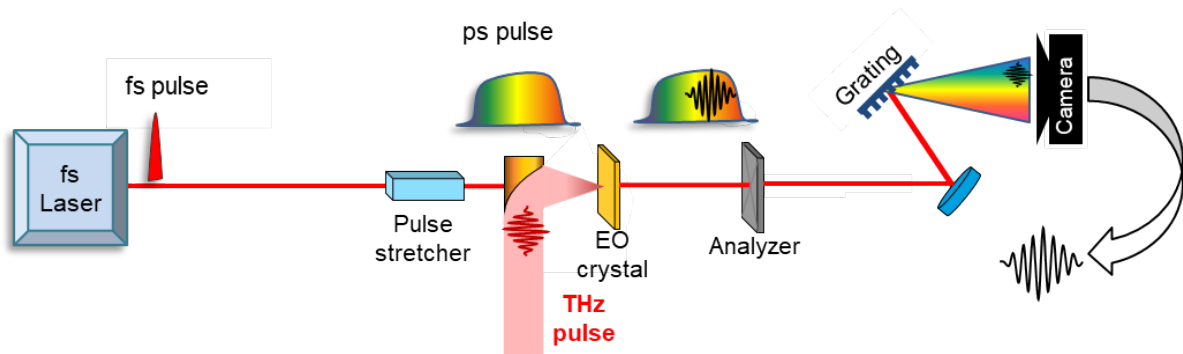


Figure 3.5: EOSD scheme principle: THz pulse is imprinted on a stretched laser pulse. The polarization modulation by the THz pulse is transferred to intensity modulation of the spectral components of the laser and detected via a grating spectrometer and a line CCD camera.

The temporal limitation of the spectral decoding technique depends on the pulse duration and the chirp of the laser pulse. It can be estimated as $\sqrt{\tau \times \tau_{stretched}}$, where τ is the laser pulse duration and $\tau_{stretched}$ is the chirped pulse duration. The linearity of the chirp is very important in order to retrieve the THz waveform correctly. The camera and grating parameters also contribute in the final resolution.

3.4 Pyro detectors

One of the most common types of detectors for the measurements of the THz pulse intensity is pyroelectric detector. The main feature of the pyroelectric crystals is that they have asymmetry, which leads to the change of electrical polarization due to heating or cooling. In the detectors, pyroelectric crystals are usually coated with a layer of absorbing material for the pulses in the IR-THz range. When the pulse comes, the absorbing material heats up, transfers the heat to the crystal layer, leading to the change of the surface charge and therefore the change of the polarization of the crystal and generation of the voltage peak. As the pulse passes and does not hit the detector anymore, the absorbing material is cooling, therefore creating a charge of an opposite polarity in the crystal and generating the second voltage peak. The total change of the polarization is proportional to the change of the temperature of the crystal, meaning that the detectors response is linear to the pulse energy change.

Typically, pyro detectors are designed with a window in the front, which has two functions: 1) it reduces the influence of the environment, such as the air flow, sounds or vibrations, which can lead to the false signal because pyroelectric materials are also naturally piezoelectric and 2) to narrow the spectral range of interest, as the window has certain transparency bandwidth. At the THz beamline, custom-made pyro detectors without a window are used. This expands the

sensitivity of detection for the whole spectral range of the THz source at FLASH. As the pulse energies are normally very high at FLASH, the signal to noise ratio of such detectors is very high and therefore the movements of the air do not induce many disturbances. Normally the measurements with pyro detectors are done with at least 10 averages per point in time, therefore increasing the signal to noise ratio.

Pyro detectors work at room temperature and their repetition rate depends on the thermal and electrical time constants. The thermal time constant depends on the size of the chip and can not be changed. The smaller the chip, the faster is the response. The electrical time constant depends on the electronics, implemented in the detector and can be widely adjusted in some configurations. The detectors, used at the THz Beamline at FLASH have a thermal time constant of 100ms and the custom designed electronics with the pulse shapers and amplifiers from the DESY FLA group, which allows to resolve the pulses within $4 \mu s$ and therefore distinguish them within the FEL bunch train, where pulses are separated by $100 \mu s$.

A set of $100 \mu m$ sized pyro detectors are implemented as a 2D matrix in the Pyrocam III from Ophir Photonics, which is widely used device for 2D beam profile measurements. Unfortunately it is not possible to integrate this device in the vacuum.

3.5 THz spectral filters

Broadband radiation from the dump magnet and undulator edges are always present together with the coherent undulator based radiation. Some experiments require the narrow spectral bandwidth, and to filter out the unwanted spectral components various spectral filters (e.g. metallic multi-mesh filters from QMC) are used. Often, it is especially important to cut off the shorter wavelength components, which extend to optical spectral range. Therefore, long pass filters, which block the wavelength shorter than a certain value letting the longer wavelengths pass with the efficiency over 90% , are commonly used at THz beamline.

3.6 THz Streaking

An established technique for the characterization of the XUV pulse duration in a single shot way is THz streaking. This technique also gives the information about the temporal jitter between XUV and THz pulses [47, 4, 48]. In the THz streak camera, the electrons produced by the excitation of a gas target with the XUV pulse, gain momentum by the applied external THz field. Two time-of-flight (TOF) spectrometers detect the deflected photoelectrons parallel and perpendicular to the polarization of THz field. The streaked electrons experience the energy shift, proportional to the THz field vector potential.

Although this technique is suitable for the measuring of XUV pulses, it requires a high level of complexity in order to measure the multi-cycle THz field profile at FLASH. It is well

possible to obtain the profile of a spectrally filtered THz pulse, but in order to resolve the higher harmonics of the THz pulse, short XUV pulses are required (<100 fs FWHM for resolving 10 THz pulses). Additionally, the shot-to-shot deviations in the XUV and THz pulse shape sets additional complications to the measurements.

3.7 Fourier transform infrared spectroscopy at FLASH

Another way to measure spectrum at THz beamline, besides the EOS technique is the Fourier transform infrared spectroscopy technique (FTIR), based on using the lamellar grating interferometer. The setup and description are presented in Chapter 6. The lamellar grating interferometer, contrary to the EOS setup has a much simpler principle without the need to use an external laser and the jitter correction setup. The full spectral measurement with the lamellar grating interferometer takes less than 30 min, while it takes 4-8 hours for the measurements with EOS, which is relevant during the beamtimes, when the time is very limited. It is also not affected by the bandwidth of the detection crystal (0 - 7 THz), which potentially allows to measure the full spectral range of THz at FLASH (1-300 μm or 1 - 300 THz).

Chapter 6 of this thesis describes the principles of FTIR spectroscopy, the working principle and benefits of the new developed lamellar grating interferometer for THz beam spectral characterization.

Chapter 4

THz Doubler characterization

The main idea behind the THz Doubler scheme, described in the Chapter 2 is optimization of the XUV-THz pump-probe experiments at FLASH. Originally THz and XUV pulses, generated by the same electron bunch are synchronized down to 5 fs, but have 7.7 m (21.5 ns) optical path difference when reaching the experimental station at FLASH. So far, to solve this problem a refocusing XUV mirror scheme was used, where XUV beam passed through the experiment, got refocused by a multilayer normal incidence XUV mirror backwards to the experiment, where it would overlap with the THz beam spatially and temporally. But due to the limitations of the multilayer mirrors for XUV in the given geometry, the full potential of FLASH is limited during the XUV-THz pump-probe experiments. Due to the narrowband nature of the multilayer mirror the reflectivity is typically $\sim 50\%$ of the initial pulse energy, the wavelength can not be changed without changing the mirror and the long focal length does not allow to focus the XUV beam tightly.

THz Doubler, on the contrary, has the potential to perform experiments with variable XUV wavelength without loosing the pulse energy due at the multilayer mirror, while keeping the XUV and THz pulses temporally synchronized. In the scope of this work, the temporal and spatial properties of the THz Doubler XUV and THz pulses were investigated. The results of this characterization are presented in this chapter, namely the temporal jitter and relative pulse energies of the THz Doubler pulses.

4.1 XUV suppression measurements

One of the most important requirements of the THz Doubler scheme is the suppression of the first XUV pulse while keeping the THz signal at a high level. At the same time, the second XUV pulse should have higher pulse energy. In order to understand which parameters contribute more or less in the suppression of the XUV, dedicated tuning studies were performed at FLASH.

For the relative pulse energy measurements of the XUV pulses several methods were used in this work are presented below. The main requirement for the detector is to measure 21.5

ns separated pulses simultaneously. In one of the techniques the fast XUV photodiode from OPTODIODE with a rise time of 5 ns was used. XUV photodiode was inserted in the direct XUV beam in the experimental chamber at FLASH1 beamline BL3. In order to avoid damage of the detector, strong attenuation filters for XUV were inserted in the beam. Typical attenuation levels were in the 10^{-2} range.

A typical shot obtained with the photodiode at the XUV wavelength 13.5 nm (92 eV) where two 21ns delayed pulses can be clearly distinguished is presented on the Fig. 4.1. The measurement was done before accelerator optimization, therefore the two XUV pulses differ in intensity only by a factor of 2.

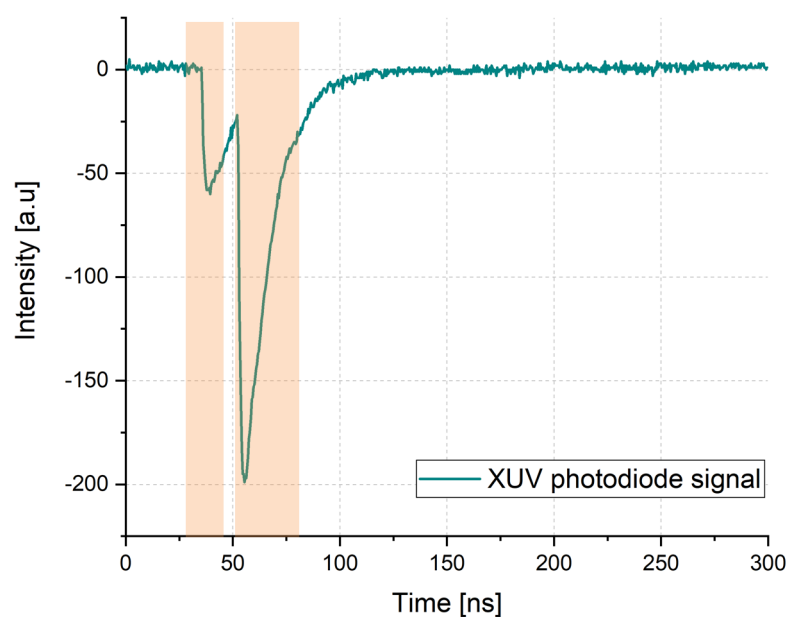


Figure 4.1: XUV double pulse suppression measurements with a fast XUV photodiode. 1st and 2nd XUV pulses separated by 21 ns can be clearly distinguished during the tuning phase. The orange bars indicate the positions of the pulses for clarity.

For these measurements, the XUV photodiode was installed in the in the sample position and therefore could not be used as an online pulse energy monitoring tool during the experiment. Therefore a second method, a Gas Monitor Detector (GMD) was used.

The GMD is a detector to measure absolute XUV pulse energies at FELs, which was developed at FLASH. It is a reliable diagnostics tool which measures XUV pulse energies on a shot-to-shot basis. This is particularly beneficial for SASE FELs like FLASH, where pulse energies experience statistical fluctuations [49]. GMDs are transparent detectors for XUV pulses, based on the ionization of gases and detection of electrons and ions. Charged particles, created by the ionization of gas molecules with an XUV pulse are accelerated in the ionization chamber via an external electric field towards the electrodes. The initial intensity of the XUV pulse is estimated from the amount of detected ions with more than 90% accuracy and less than

10% error. The GMD detectors are calibrated at the laboratory of the Physikalisch-Technische Bundesanstalt (PTB) in Berlin.

The GMDs temporal resolution is 100 ns FWHM, with the electronics available at FLASH1. It is well optimized for measuring the XUV pulse energy of the individual bunches within a bunch train in the MHz regime but the observation window is too long for resolving the 21 ns separated pulses. Although a separate measurement of each pulse was possible while the other pulse was blocked. The temporal resolution requirement was fulfilled by sampling not the integrated electron signal, but the direct analog signal from the GMD. This made a dramatic difference on the temporal resolution. Fig. 4.2 shows an example of the electron response: two sharp peaks on the left side can be well distinguished and correspond to the doubler XUV pulses, collected in the inner detector area. The residual signal comes from the outer region of the detector. This method gives a precise picture on the relative XUV pulse energies in a shot-to-shot non-invasive way, which is especially beneficial for the THz Doubler scheme.

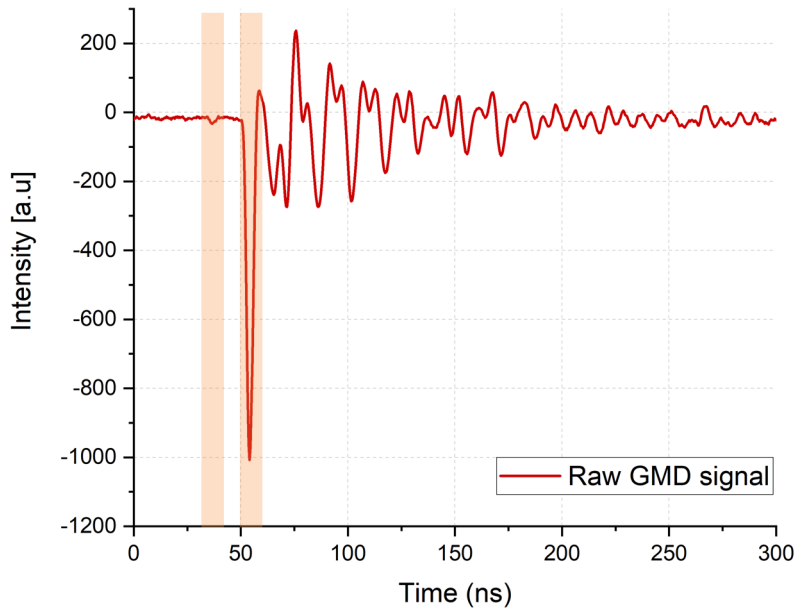


Figure 4.2: Electron signal from the fast GMD (not averaged) for XUV suppression measurements after tuning. The 1st pulse has significantly lower intensity than the 2nd pulse. The orange bars indicate the positions of the pulses for clarity.

The results of the suppression measurements for a XUV wavelength of 11 nm with the electron-GMD is shown on the Fig. 4.3. The pulse energy distribution is shown in Fig. 4.4. The results are shown in arbitrary values because the extracted fast GMD signal is not calibrated.

The average ratio of the 2nd pulse with respect to 1st $\frac{E_{2^{nd}UV}}{E_{1^{st}UV}} = 18$.

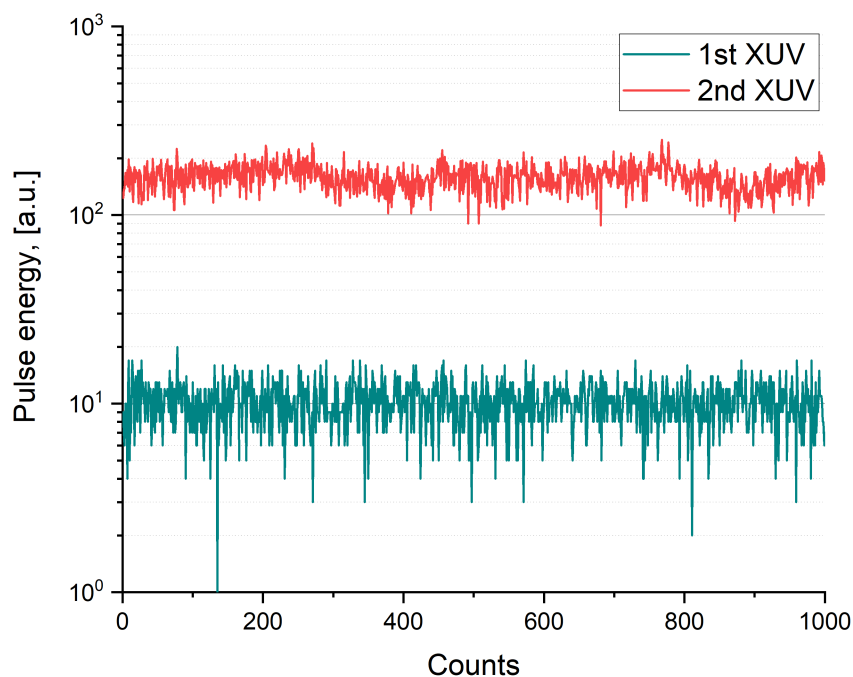


Figure 4.3: XUV double pulses suppression result. The 1st pulse stays constantly suppressed. Pulse energy ratio between the pulses is 1:17 (1st to 2nd) on average over 2.5 minutes of measurements.

Pulse energy	1 st pulse	2 nd pulse
XUV	0.4 μJ	40 μJ
THz	3 μJ	4 μJ

Table 4.1: THz Doubler pulse energies after tuning

These measurements demonstrate that independent manipulation of ns spaced electron bunches at FELs as well as XUV shot-to-shot characterization is possible. The generation of THz with high pulse energy for the first bunch was successfully performed as well.

During the experiment, the relative intensities of the XUV pulses measured via the XUV photodiode and the GMD differed a lot, therefore a correlation measurement was performed. Fig. 4.5 shows the results for the 2nd XUV pulse and it is clear that there is no correlation between two detectors. The XUV photodiode, the way it was installed in this experiment gave an approximate picture of the pulse energy fluctuations, but it showed a noticeable non-linear response, in comparison to the GMD. In the future, using the online-monitoring via GMD is more favourable.

The exact XUV pulse energy was measured with calibrated GMD and THz pulse energy - with a THz pulse energy meter. In this case one of the THz Doubler pulses was blocked in the injector laser section and another one was measured. The results of these measurements are presented in the Table 3.1.

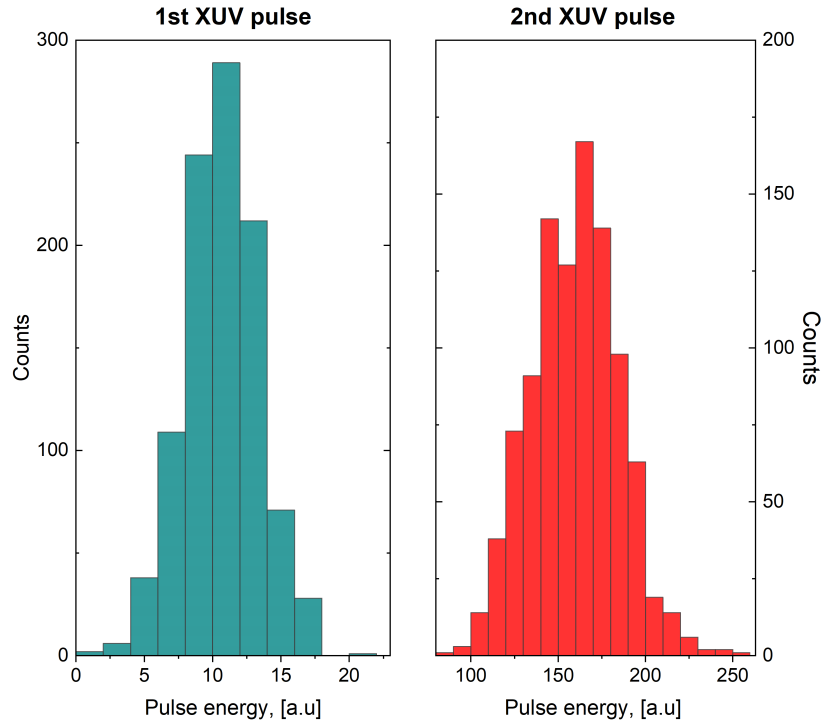


Figure 4.4: XUV Doubler pulse energy distribution after tuning.

For the calibrated THz pulse energy measurements a radiometer (RM3700, head RjP-735/RF, by LASER PROBE) is used. It was earlier cross-referenced to a PTB (The National Metrology Institute of Germany) traceable 3A-P-THz detector, by OPHIR OPTRONICS SOLUTIONS. This detector is installed in the THz hutch in the ambient air few cm (<10 cm) away from the diamond window which separates the vacuum chamber from the air in the laboratory. It is normally used for monitoring the THz pulse energy during the machine tuning procedure [27]. With the maximum repetition rate of 1 kHz, it can not resolve the separate pulses in the bunch trains. Normally it is triggered to 10 Hz of the machine and the output is the integrated pulse energy over 1ms, resolving single pulse trains from the machine. The measured pulse energy at the position of the detector is different to that in vacuum by the factor of 0.7 because of the absorption in the diamond window.

4.2 Jitter measurements

Knowing the arrival time information in pump-probe experiments is essential to be able to perform high resolution time-resolved experiments.

In the standard mode of operation, when one electron bunch generates both XUV and THz pulses used in a pump-probe experiment, the jitter between THz and XUV pulses at FLASH was found to be low (~ 5 fs) [4]. In this case THz and XUV are produced by the same electron bunch. In case of THz doubler scheme THz and XUV pulses are produced by different electron

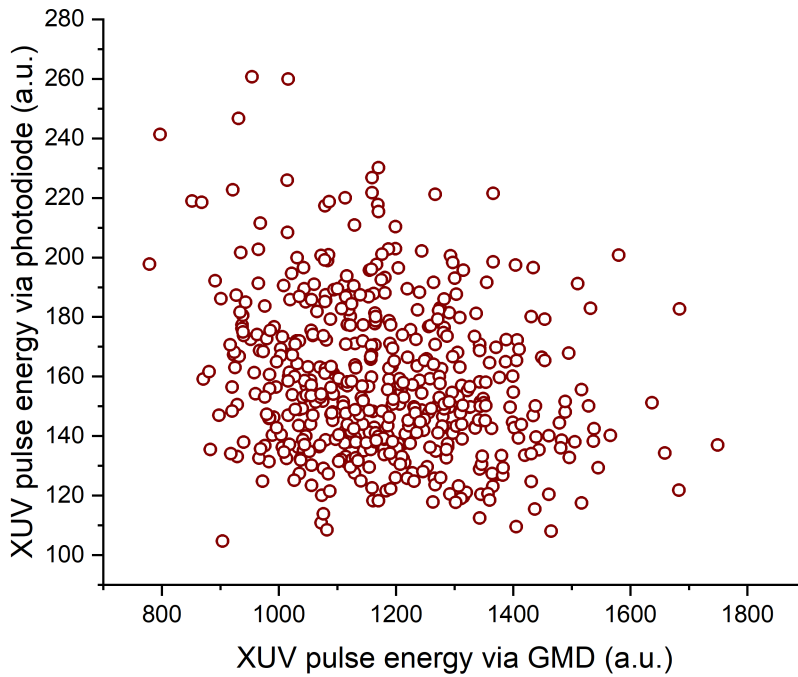


Figure 4.5: Correlation plot of XUV photodiode and GMD electron signal.

bunches with potentially very different parameters. Therefore, it is important to compare the arrival time jitter of the two pulses in the new THz Doubler scheme to the standard conditions.

The laser system for diagnostics of THz pulses at FLASH1 experimental hall is synchronized to the FLASH accelerator with a timing jitter up to 100 fs r.m.s. (200 fs peak to peak), which limits the resolution. Only pulses with a cycle longer than the jitter value can be resolved in this case ($> 30 \mu\text{m}$ or $< 10 \text{ THz}$). The resolution is dramatically improved down to 9 fs r.m.s. by monitoring and correcting for the jitter between the laser and THz with the combination of sequential electro-optical sampling (EOS) and spectral decoding (EOSD) schemes [9]. In order to measure the shot to shot arrival jitter EOSD scheme is implemented and synchronized to the EOS.

In order to measure the jitter between 21 ns separated THz pulses in the THz Doubler scheme the existing EOSD scheme was modified. As XUV and THz created by the same electron bunch are locked to each other it is assumed that the jitter between THz double pulses is comparable to the jitter between the THz and XUV pulses from the 1st and 2nd bunches of THz Doubler, respectively [4, 45, 50].

TANGERINE fiber laser from AMPLITUDE SYSTEMS, synchronized with the FLASH accelerator via the Master-clock [13], providing 1030nm wavelength pulses with a FWHM of 8.3 nm bandwidth and a minimum pulse duration of 320 fs FWHM. After the optical parametric amplifier (OPA) from CLASS 5 PHOTONICS [51] we get pulses with central wavelength of 830

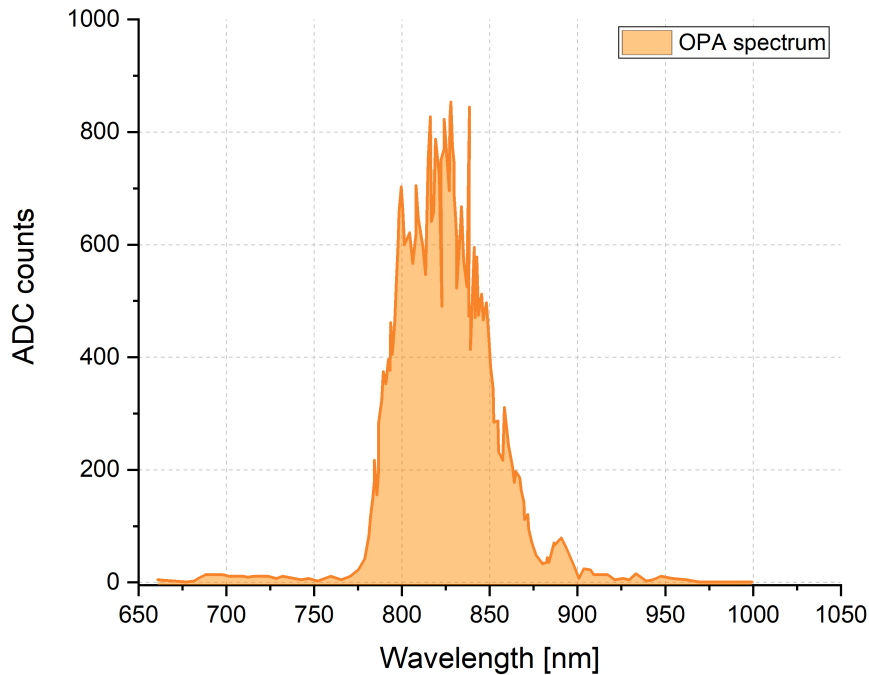


Figure 4.6: The spectrum from the OPA, centered around 830 nm with 50 nm bandwidth.

nm and approximately 50 nm bandwidth. The measured spectrum of the OPA is presented on the Fig. 4.6.

4.2.1 Modified spectral decoding scheme

The probe laser pulse initially having 30 fs FWHM at 830 nm is split with a non-polarising beamsplitter into 2 replicas [6]. One part of the beam is delayed by 21.5 ns with respect to another and then recombined on the same type of non-polarizing beamsplitter, therefore each replica of the pulse corresponds to the THz doubler pulses. 21.5 ns delay is achieved by multiple reflections of two 2" gold-coated mirrors.

The recombined laser beams are transported towards the EOSD setup along the same optical path. Because the beam is split optically and the whole setup is mounted on the same optical table, the temporal instabilities are considered to be negligible. The scheme of the EOSD for THz Doubler jitter measurements is presented in Fig. 4.7. Laser pulses are stretched with a dispersive material (150 mm dispersive Sf-57 glass) up to a duration, sufficient to cover 2 THz pulse length ($\Delta\tau_{THz} \sim 5 ps$). The laser pulses are spatially and temporally overlapped with the corresponding THz pulses on the electro-optical crystal. In order to be able to detect the respective arrival time between the two THz doubler bunches, the arrival time of the laser pulses is adjusted such that the THz doubler pulses modulate different spectral regions of their respective probe laser pulses. The modulations are well separated to avoid ambiguities

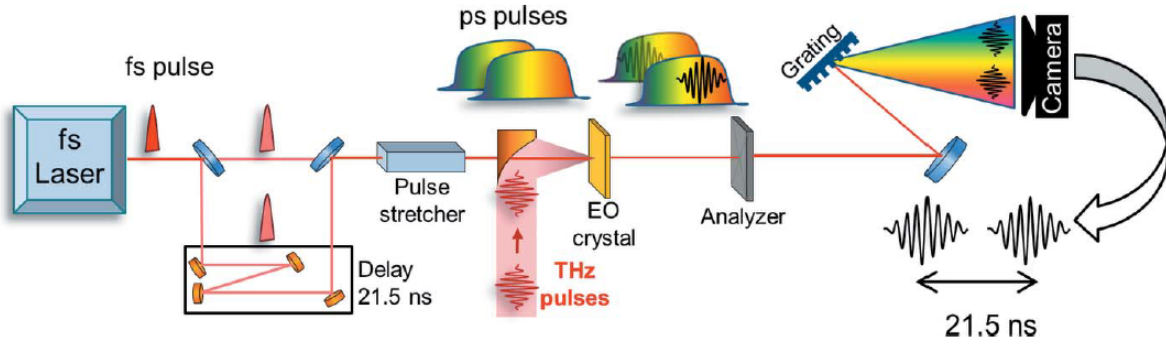


Figure 4.7: Modified spectral decoding scheme for detection of THz Double pulses. The probe laser pulse is split and delayed by 21.5ns, matching the arrival time of 1st and 2nd THz pulses respectively. Two laser pulses are imaged as one on the camera because of longer integration time, therefore enabling measuring the relative arrival jitter of both THz pulses.

in arrival-time determination. Laser pulses are sent to a grating spectrometer (PRINCETON INSTRUMENTS, Acton SP2300i) and dispersed on the 1D camera.

For detection, a line camera (BASLER Sprint Mono spL-2048-70km) was used. The camera is routinely used for the jitter measurements, using 512 pixels out of 2048, which allows it to run at the repetition rate of 200 kHz. For the THz Doubler scheme, it is important to fit the long laser pulses over the whole chip of the camera. Therefore, its useful range was extended to 1024 pixels, therefore the repetition rate was reduced to 100 kHz. Each pixel has the size of $10\mu\text{m} \times 10\mu\text{m}$ with 12-bit dynamic range [9].

4.2.2 Laser stretching

The stretching was chosen considering that the laser pulse must be long enough for two THz pulses to fit into the time window without overlapping on the camera. This is achieved when the laser pulse goes through a dispersive material with preferably high group velocity dispersion (GVD) value, which is usually used in order to estimate the stretching of the pulse in media. The material of choice is SF-57, which has a GVD value of $199.44 \frac{fs^2}{mm}$ [52]. Another suitable material would be ZnTe with the GVD of $923.71 \frac{fs^2}{mm}$ [41]. To estimate the length L of the dispersive material (SF-57 glass), necessary to stretch the pulse to the required pulse duration and to describe the propagation of the laser pulse through it, the spectral phase $\phi(\omega)$ around a central frequency of ω_0 can be used:

$$\phi(\omega) = \phi(\omega_0) + \phi'(\omega)(\omega - \omega_0) + \frac{1}{2}\phi''(\omega)(\omega - \omega_0)^2 + \dots \quad (4.1)$$

The laser pulse travels with a group velocity v_g . It propagates as a wave packet, composed of different frequencies within the given bandwidth:

$$v_g = \frac{c}{n(\omega) + \omega \frac{dn}{d\omega}} \quad (4.2)$$

After traveling the length L in the material, the different spectral components of the laser pulse gain corresponding spectral phases of

$$\phi(\omega) = k(\omega)L = \frac{\omega}{c}nL \quad (4.3)$$

where $k(\omega)$ is the the wave number of the plain wave in medium, or the propagation constant. The first-order derivative of the propagation constant k' relates with the group velocity as following:

$$k'(\omega) = \frac{dk}{d\omega} = \frac{1}{v_g} \quad (4.4)$$

The first derivative of the spectral phase $\phi'(\omega)$ describes the delay of the peak of the incident pulse T_g but not the delay of individual spectral components:

$$\phi'(\omega) = \frac{d(kL)}{d\omega} = L \left(\frac{dk}{d\omega} \right) = L \frac{1}{v_g} = \frac{L}{c} \left(n(\omega) + \omega \frac{dn}{d\omega} \right) = T_g \quad (4.5)$$

When the pulse propagates through the dispersive medium individual components travel with different velocities because the refractive index n is different for different frequencies of the laser pulse $n = f(\omega)$. This leads to the broadening of the pulse in the temporal domain. For convenience of the data reconstruction stretching of the laser pulse with a linear chirp is preferable in the EOSD setup. This allows for encoding of time to spectrum as a linear function. The second order of the propagation constant $k(\omega)$ is the group delay dispersion (GDD):

$$\phi''(\omega) = \frac{d^2\phi}{d\omega^2} = \frac{L}{c} \left(2 \frac{dn}{d\omega} + \omega \frac{d^2n}{d\omega^2} \right) = GDD \quad (4.6)$$

Group velocity dispersion (GVD) relates to GDD as $GDD = GVD \times L$.

The pulse duration of the linearly chirped laser pulse with original pulse duration of $\Delta\tau$ after the dispersive material of length L is:

$$\Delta\tau_{stretched} = \sqrt{\Delta\tau^2 + \left(4 \ln 2 \frac{GVD \times L}{\Delta\tau^2} \right)^2} \quad (4.7)$$

With one SF-57 glass block of 150 mm and the original pulse duration of 20fs at 830 nm central wavelength, the measured FWHM pulse duration of a Gaussian chirped laser pulse is $\Delta\tau_{stretched} = 6.4 \pm 0.1 ps$.

The results of the auto correlation of the pulse duration are presented in the Fig. 4.8.

The verification of the linearity of the chirp is described in the following section.

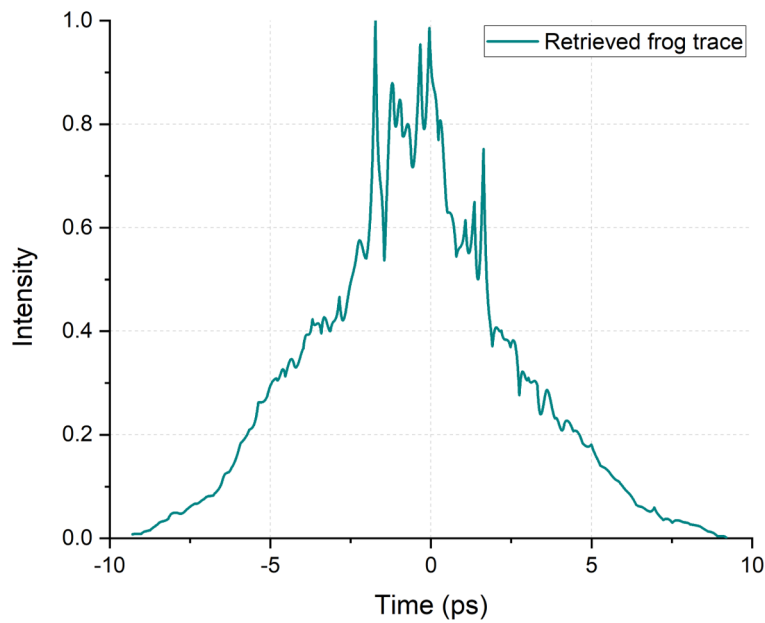


Figure 4.8: Pulse duration of the stretched laser pulse after passing through 150 mm SF-57 glass measured by FROG technique

4.2.3 Choice of the electro-optical crystal

In the electro-optical spectral decoding scheme (EOSD) which is used for arrival time measurements, EO crystals must have a high electro-optical coefficient r_{41} to ensure the encoding of the time information on the laser pulse with a good signal-to-noise ratio. The most common crystals for electro-optical sampling are Zinc Telluride (ZnTe) and Gallium Phosphate (GaP). GaP crystal has a broad detection range up to 11 THz and it is preferred for the sequential EOS measurements, because it allows to measure the THz electric field as precisely as possible.

ZnTe on another hand has a narrower detection bandwidth but a higher electro-optical coefficient r_{41} , leading to higher signal-to-noise ratio of the detected polarization modulation with a camera. This crystal is more preferred in single shot spectral decoding measurements, which is the critical technique for the jitter measurements. The shape of the detected THz field is of less importance, therefore there is no strict requirement on the detection bandwidth and neither on the absence of spectral distortions [40]. By using the cross-correlation technique, the accuracy of the arrival time can be determined down to 10fs for the signals which have a 3 THz maximum bandwidth [9].

4.3 Experimental realization

The THz pulses in the experiment presented here are generated by FLASH's electron beam dump magnet by the edge radiation process, as described in the Chapter 2 of this thesis and in

[5, 45, 30]. The profile of the Dump radiation deviates from the expected single-cycle profile possibly because of the non-crossed polarization setting of the EOSD setup and frequency mixing between the chirped laser and the THz pulse and the THz absorption in air [53, 40]. However, the measured distorted profiles keep the same shape during the measurements, therefore it does not affect on the arrival time measurements.

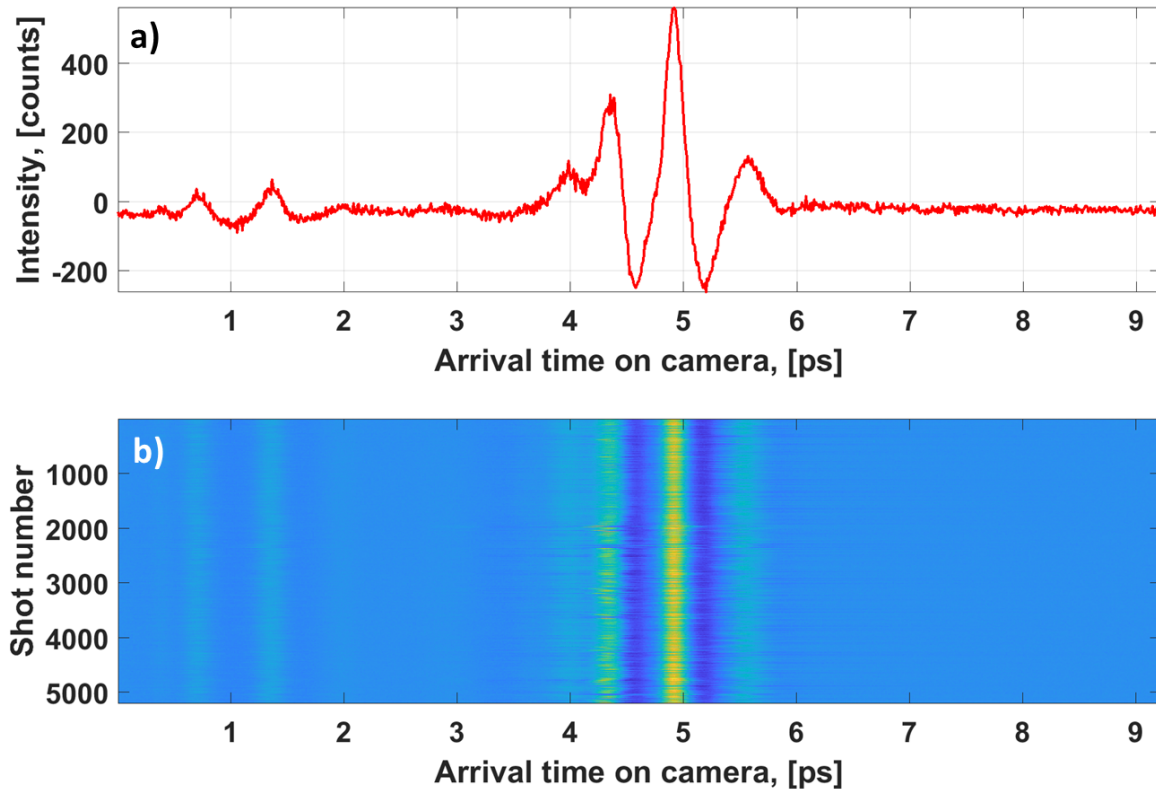


Figure 4.9: Spectral decoding traces for THz double pulses. a) Single shot background subtracted THz Doubler profiles measured simultaneously with a camera, b) 5000 consecutive traces with the jitter correction.

A single shot trace, showing the intensity modulation of the laser spectrum created by the THz pulses in the EOSD setup is presented in the Fig. 4.9 a). Two THz Doubler pulses can be well distinguished and do not overlap with each other, which makes it possible to evaluate the jitter of individual pulses with respect to the corresponding laser pulse. In order to do that, each pulse was separately evaluated. The jitter of the 1st THz pulse was found for the region between 0 ps and 2.5 ps, and 2nd - between 3 ps and 7 ps.

By arbitrary choosing a reference trace (for example the 1st trace) and doing the cross correlation of this trace to every subsequent one, the information about the arrival time for every single shot was retrieved. Every single trace was shifted towards the reference by its jitter value [9]. Fig. 4.9 b) shows the result of the corrected traces with respect to the reference. A good overlap of the peaks can be seen, which indicates the accurate jitter correction. This procedure was performed for each of the THz pulses.

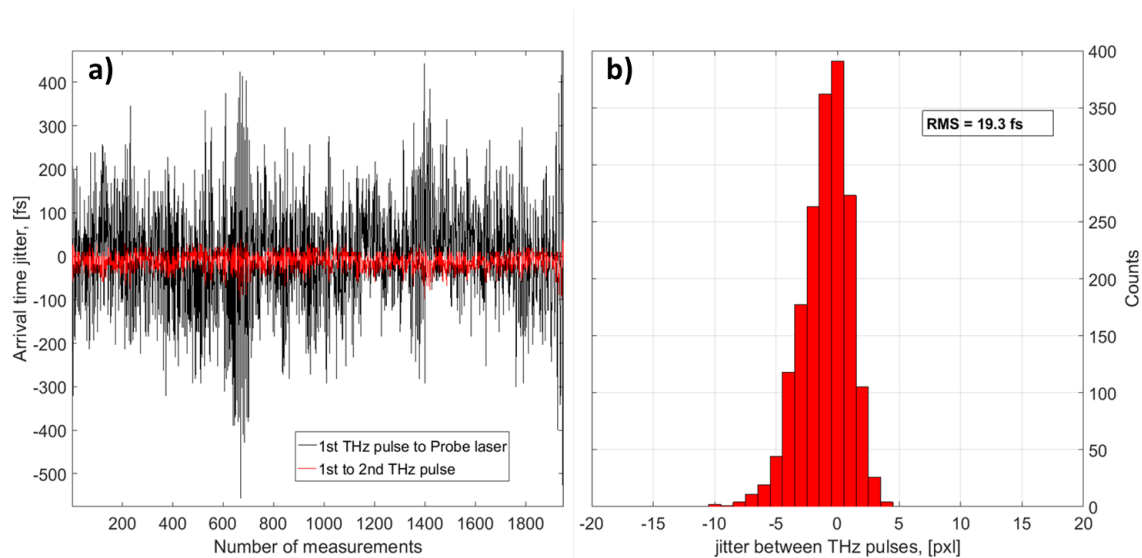


Figure 4.10: Jitter measurement results. a) Arrival time jitter of the laser with respect to the machine (black curve) and relative jitter between two THz Doublers pulses (red curve). b) Distribution of the relative jitter between THz Doublers pulses has a width of 19 fs (r.m.s)

The extracted arrival time of individual THz doubler pulse with respect to the corresponding probe laser pulse is shown as the black curve in Fig. 5.10. Assuming that the jitter between the split laser pulses is negligible, the difference of the jitter between the THz Doublers pulses gives their relative temporal jitter (red curve in Fig. 5.10). The jitter between THz pulses and probing laser (96 fs r.m.s.) is much larger than that between THz doubler pulses. The jitter measurements result for the condition when THz undulator was set to $140 \mu\text{m}$ wavelength was also performed. The jitter between the THz doubler pulses is estimated to be on the level of 19 fs (r.m.s.) over a period of 15 min.

Temporal calibration of the spectral decoding scheme was performed by measuring the undulator trace of the 2nd THz Doublers pulse with a $215 \mu\text{m}$ (1.4 THz) band pass filter. By measuring the trace over a few minutes at a fixed position and by applying the cross-correlation jitter correction procedure, a mean trace of the THz field can be obtained (Fig. 4.11 a)). The period of one cycle of the filtered THz pulse has a fixed value ($215 \mu\text{m}$ or 717 fs), which corresponds to a fixed number of pixels on the camera. This dependency and the linear fit is shown on the Fig. 4.11 b). The time-to-pixel calibration coefficient in this case is $9.7 \pm 0.1 \text{ fs/pxl}$. The linear dependence confirms the linear chirp of the laser pulse.

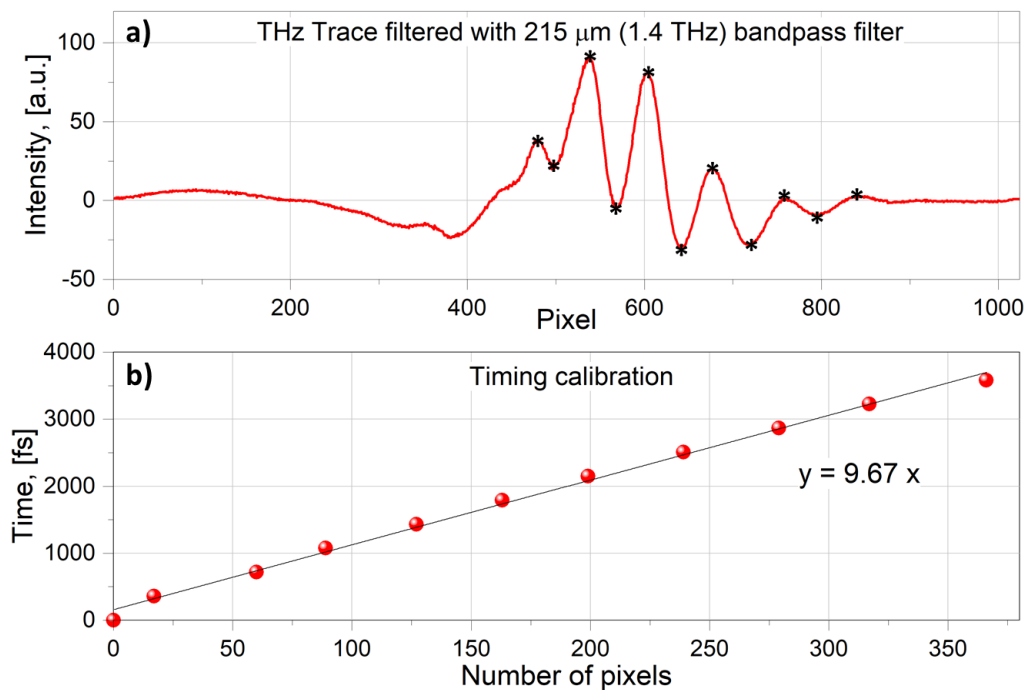


Figure 4.11: The mean trace of the THz field, filtered with 215 μm band pass filter used for spectral calibration. A period of one cycle corresponds to the 215 μm wavelength and a fixed number of pixels on the camera. The time-to-pixel calibration coefficient is $9.7 \pm 0.1 \text{ fs/pxl}$. The graph also demonstrates the linearity of the chirp.

Chapter 5

XUV plasma switch for THz

This chapter presents a new spatio-temporal overlap tool between XUV and THz pulses, based on the *XUV plasma switch* principle. The basic idea is probing with the THz the changes of optical properties of silicon, induced by intense XUV pulses. At the moment of the temporal overlap between two pulses, a clear switch of reflectivity/transmission of THz can be observed. This method offers the temporal resolution within the duration of the THz pulse (picosecond range) and can be implemented for both FELs and high harmonic generation (HHG) sources. The spatial characterization of THz and XUV pulses is done by 2D raster scan in the focus position. It provides the essential information of both the shape of the focus and the spatial overlap of the pulses. The THz Doubler scheme, described in the Chapter 4, offers a great timing flexibility for XUV-THz pump probe experiments, and therefore needs a tool for establishing the precise timing

Certain pump–probe schemes, e.g. THz streaking [4, 34], are comparatively tolerant against the spatial overlap between XUV and THz pulses and the actual focal position of the THz beam. The observable, i.e. the kinetic energy of the photoelectrons, is furthermore of considerable magnitude and can be utilized for further optimization of the pump–probe signal. This is almost never the case in pump–probe experiments on solid-state samples, utilizing one of the XUV probing techniques (e.g. X-ray magnetic circular dichroism (XMCD) [54, 55] and resonant inelastic X-ray scattering [56]). There, the spatio-temporal overlap between THz and XUV and in particular diffraction-limited focusing of the THz beam have to be achieved with the aid of versatile in-vacuum diagnostics.

The following section gives an overview on the ultrafast ionization processes taking place in silicon after the excitation by intense XUV pulses, as well as describes the experimental realization of the XUV plasma switch for two geometries: 1) with the XUV refocusing mirror, compensating the optical delay between XUV and THz pulses and 2) with the THz Double pulses scheme. The last section also describes the recent single-shot XUV plasma switch experiments and the further perspectives.

5.1 Theory of ionization dynamics in semiconductors

Silicon (Si) is a common material used as a beam splitter for the mid- and far-infrared spectral regions range [57, 9]. In the THz range, typically high resistivity ($>5\text{k}\Omega\text{cm}$) Si is used. In this case, the free-carrier absorption is reduced and Si has a broad and flat transmission along the broadband spectral range (from $12\ \mu\text{m}$ to millimeter wavelengths) [58], which makes it a suitable material for a beam splitter at such a broadband source as the THz sources at FLASH (See Fig. 2.7 for the transmission curve).

Si is also an interesting material to study the processes induced by intense X-Ray radiation in semiconductors [59, 51]. The free-electron plasma, created by the electronic excitation changes the optical properties of Si. These changes can be probed with UV, optical or THz pulses and such schemes are widely implemented at FELs as temporal characterization tools. Knowing these properties, the processes and their dynamics on femtosecond scales in Si pushes further the investigation of such topics like development of new highly sensitive photon detectors [60], nano-materials [61], new types of emitters [62, 63] and especially the miniaturising of semiconductor electronics. The information obtained for Si can be further applied for other physical models and materials. In the section below, the basic processes of the excitation of semiconductors with X-Ray pulses is described.

The study of the ionization processes and the plasma dynamics in the XUV and IR/THz ranges has widely contributed to the development of the timing and ultrafast pulse characterization at FELs [51, 64], as well as successfully used for pulse picking and temporal shaping of short IR or THz pulses [2, 39, 65, 66]

5.1.1 Excitation processes

The process of excitation of materials by intense X-Ray pulses happens on ultra fast time-scales and, depending on the properties of the material and the photon energy, can be governed by different processes [51, 39]. If the photon energy, $\hbar\omega_{ph}$, is high enough to excite the bound electrons with the ionization potential I_p (in M, L or K edges) from their initial states then these electrons will be transferred to the higher energy states E_e , leaving a hole in the corresponding energy level:

$$E_e = \hbar\omega_{ph} - I_p \quad (5.1)$$

If the energy of the incoming photon is less than the ionization potential, required to excite the bound electrons, then it will transfer the energy to the electrons in the valence band, and the latter will be lifted to the conduction band.

The primary ionization takes place on the ultrafast time-scale within the duration of the pump pulse (fs or shorter). The following secondary processes occur on longer time scales and can last up to several tens of picoseconds [59].

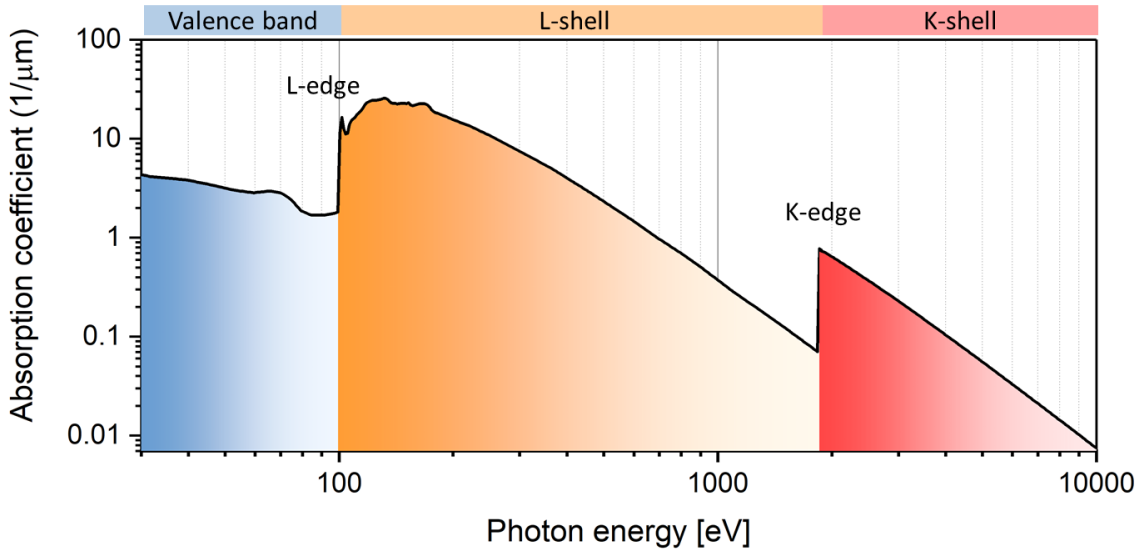


Figure 5.1: Photo-absorption coefficient of Silicon as a function of the photon energy. The values are taken from [67].

The excited electrons in the valence band with excess energy lose their energy via elastic and inelastic scattering on other electrons (impact ionization and Auger decay). These newly created electrons continue to scatter until they reach the band gap energy $E_{min} = E_g$ (minimum energy threshold below which the electrons cannot trigger further excitation processes). The holes, which are created during the primary ionization recombine with electrons in higher energy levels and the released energy can be sufficient for further excitation until the energy of the excited electron is reaching E_{min} .

The time scale τ of impact ionization of electrons can be estimated by considering the mean free path l_e and Fermi velocity of electrons $\langle v_e \rangle$: $\tau = \frac{l_e}{\langle v_e \rangle} \sim 10^{-16} s$.

In order to estimate the number of electrons N_e , created by one photon, effective-energy gap E_{EEG} can be used [68]. The concept of effective energy gap allows to correctly estimate the number of free electrons, produced by one photon within the duration of the ultrafast pump pulse (at FELs like FLASH the XUV pulse duration reaches down to ~ 10 fs FWHM) without taking into account the processes which happen on a longer time scales, such as electron-hole recombination and relative decay of electronic vacancies. E_{EEG} can be calculated as follows:

$$E_{EEG} = \frac{1}{2}(E_{gap} + E_{min}^e + E_{min}^h) \quad (5.2)$$

where E_{min}^e is the minimal electron energy needed for impact ionization and E_{min}^h is the minimal energy of holes created via the Auger decay. In case of Si, these values are presented in Table 5.1.

E_{EEG}	E_{gap}	E_{min}^e	E_{min}^h
2.62 eV	1.12 eV	1.12 eV	3 eV

Table 5.1: Si electron and hole energies

In case of a photon with the energy used in this work $\hbar\omega_{ph} = 92$ eV (13.5 nm), the corresponding number of created free electrons can be estimated using the effective energy gap concept with the given parameters above is

$$N_e = \frac{\hbar\omega_{ph}}{E_{EEG}} = 35 \quad (5.3)$$

The number of absorbed photons in the material can be calculated, knowing the absorption coefficient for the given photon energy and the total flux of the pump pulse (Fig. 5.1).

5.1.2 Calculation of the critical electron density for THz range

Optical properties of materials, such as reflectivity, transmission and the refractive index n can be described in terms of relative permittivity ϵ [69]:

$$n \propto \sqrt{\epsilon} \quad (5.4)$$

According to the Drude model [70], the electrons in the material can be treated as plasma with the corresponding plasma frequency ω_p , and relates to the relative permittivity ϵ as follows:

$$\epsilon = 1 - \frac{\omega_p^2}{\omega^2}, \quad (5.5)$$

If the material is irradiated with light which has the frequency $\omega > \omega_p$ then the reflectivity of the material decreases and the light can propagate through. If the frequency is lower, $\omega < \omega_p$, the material becomes reflective for this light. Plasma frequency depends on the density of the free electrons in plasma:

$$N_e = \frac{\epsilon_0 m_e}{e^2} \omega_p^2, \quad (5.6)$$

A real-life example of plasma frequency is that metals like aluminum or silver are highly reflective for visible light because their plasma frequency is higher than the frequency of light, but they are transparent for x-rays with much higher frequency than the plasma frequency.

In the equilibrium state at room temperature the intrinsic free electron density of un-doped Si is $1.5 \times 10^{10} \text{ cm}^{-3}$ [71]. An XUV pulse at 92 eV generated at FLASH has $\sim 6.8 \times 10^{12}$ photons for typical pulse energies in $\sim 100 \mu\text{J}$ range. The total number of free electrons, created by one XUV pulse per excited volume

$$N_e = \frac{N_{photons}}{V_{XUV}} = \frac{E_{pulse}}{\pi E_{photons} \alpha R^2}, \quad (5.7)$$

where α is the attenuation length for the XUV pulse and R is the radius of the XUV beam in the focus. In this work XUV pulse focused on the sample had a pulse energy of $E_{pulse} = 1\mu J$, a photon energy of 92 eV and a radius of $70\mu m$. Therefore, the estimated averaged electron density was equal to $4.2 \times 10^{19} [\frac{1}{cm^3}]$.

In the presented work, the critical electron density for the probing pulse at a wavelength of $8\mu m$ (37.5 THz) is $N_{e_{8\mu m}} = 1.8 \times 10^{19} [\frac{1}{cm^3}]$ and at wavelengths over $100\mu m$ (< 3 THz) it is less than $N_{e_{100\mu m}} = 1.1 \times 10^{17} \mu m [\frac{1}{cm^3}]$.

The critical electron density for the spectral range of the THz source at FLASH is presented together with the experimental results on the Fig 5.4.

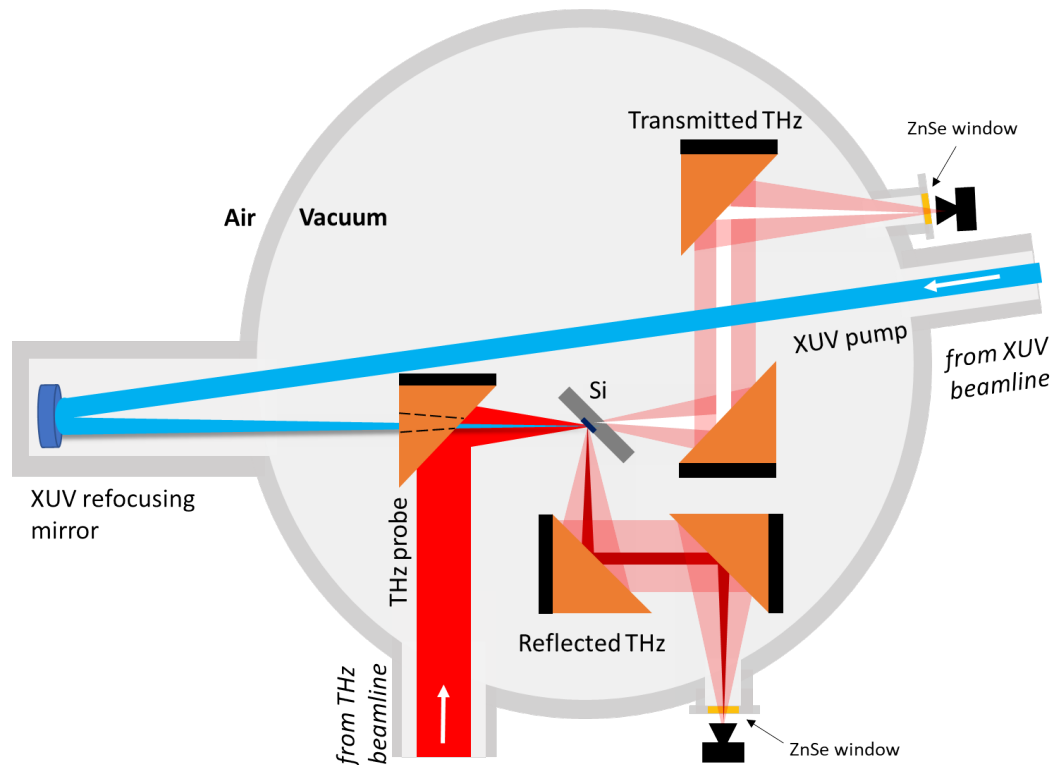


Figure 5.2: Scheme of the experimental setup for XUV plasma switch experiment in the refocusing mirror geometry with a single electron bunch generating XUV and THz. The XUV beam passes through the experiment and gets reflected and focused collinearly with THz beam matching the arrival time of THz on the Si sample.

5.2 XUV refocusing mirror geometry

The scheme of the XUV plasma switch experiment is presented on Fig. 5.2. THz and XUV beams are collinearly focused and spatially overlapped in the experimental chamber on 400 μm thick high resistivity ($>2000 \text{ Ohm} \times \text{cm}$) undoped Silicon from CRYSTECH at 45 degrees incident angle. The THz probe pulse is focused with a 152 mm focal length off-axis parabolic mirror. The XUV pump pulse at 13.5 nm (92 eV) was focused with a Mo-Si multilayer mirror, provided by R. Soufli during the user beamtime [72, 73, 74] with a focal length of 3.5 m (Fig. 5.3). The angle between incoming and outgoing XUV beam is 3 degrees and the reflectivity at 13.5 nm is approximately 65 %.

One part of the initial THz beam is transmitted through the Si wafer and another part is reflected. These beams are picked up by the corresponding off-axis parabolic mirrors, collimated and focused on the pyro detectors approximately 5 mm outside of the chamber. In the refocusing mirror geometry, 5mm thick ZnSe windows separate the experimental vacuum from the pyro detectors outside.

The detectors are INFRATEC (LME-301) pyros with 2x2 mm chip size and modified absorption material on the chip, which were specially designed for the group of B. Schmidt in

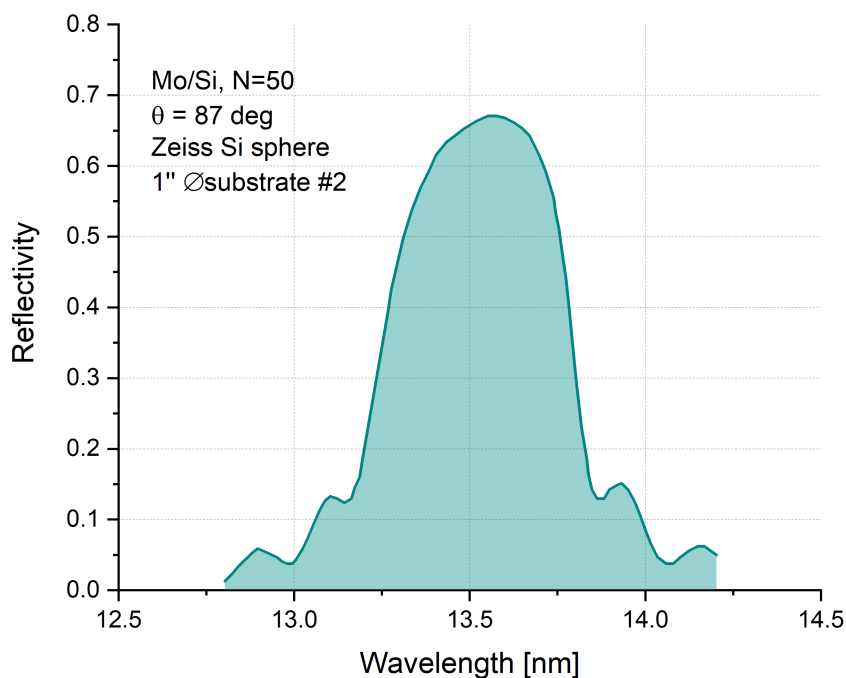


Figure 5.3: Reflectivity of the refocusing XUV multi-layer mirror with the central wavelength around 13.5 nm. Maximum reflectivity is around 65%. Courtesy to R. Souffi

DESY [12]. These pyros do not have a protective window, therefore they are sensitive in a broad spectral range.

An uncoated 5 mm thick ZnSe window from THORLABS was used, because it has a good transmission for $8\ \mu\text{m}$ (37.5 THz) and for longer wavelengths $>100\ \mu\text{m}$. The transmission curves measured with a time domain THz spectroscopy (TDS) scheme for the longer THz wavelength range combined with the data from THORLABS is presented on Fig. 5.4.

The XUV pump pulses had a fixed wavelength at 13.5 nm and THz probing has been performed at two wavelengths: 1) $8\ \mu\text{m}$ and 2) $100\ \mu\text{m}$. THz pulse duration is estimated from the EOS measurements previously performed for similar machine parameters. THz undulator, tuned to a certain wavelength generates 10 cycle pulses with the period equal to the set wavelength. Additional cycle in the THz electric field shape comes from the dump magnet and its period depends on the machine settings and lies in the range of few hundreds of femtoseconds. The pulse duration of THz pulse was expected at $8\ \mu\text{m}$ to be 300fs and at $100\ \mu\text{m}$ to be 3ps, respectively, based on the number of periods.

The XUV pulse duration was estimated from electron bunch length measurements with the Transverse Deflecting RF-Structure (TDS) (LOLA) [75]. LOLA is a setup for single shot measurements of the electron bunch shape, which also allows to roughly estimate the XUV pulse duration. The estimated XUV pulse duration is expected to be shorter than the measured duration

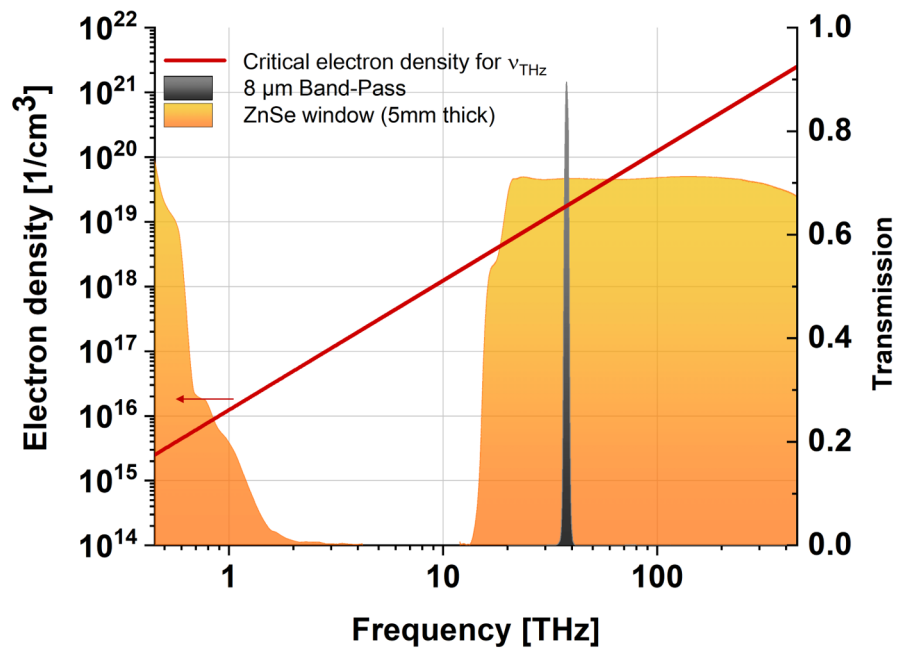


Figure 5.4: Filter for $8\mu m$ (grey area) and ZnSe window transmission (orange area) for XUV plasma switch experiment. Red line shows the required critical electron density for the THz plasma switch.

of the bunch ($FWHM_{XUV} = r.m.s_{bunch}$). Therefore with the bunch $FWHM_{bunch} = 184 fs$, the $FWHM_{XUV}$ corresponds to 148 fs short pulse [76]. The measurement of the longitudinal bunch profile with LOLA is shown on Fig. 5.5.

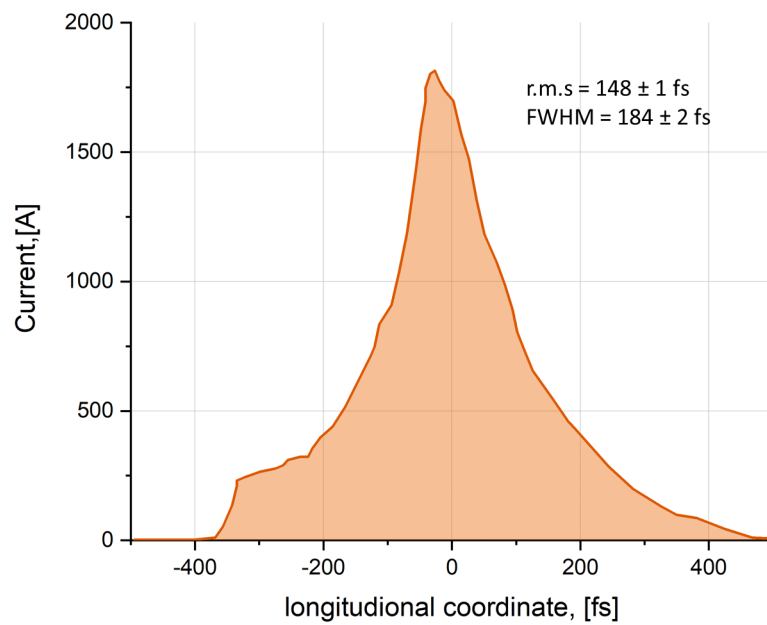


Figure 5.5: Electron bunch current profile measurement with the transverse deflecting RF-structure (LOLA). The with $\text{FWHM}_{\text{bunch}} = 184 \text{ fs}$, corresponding to $\text{FWHM}_{\text{pulse}} = 148 \text{ fs}$

5.2.1 2D beam profiles and spatial overlap

In order to characterize THz and XUV beams in the sample position, a special sample holder was designed. In the plasma switch experiment, the Si sample is placed at 45 degrees towards the incidence of the beam. To measure the shape of the beam and quality in focus it was preferable to place the detector perpendicular to the beam. Therefore the sample and the detector are installed at 45 degrees with respect to each other. (See Fig. 5.6 for details).

For 2D profile measurements a pyro detector was used in the raster scan technique. The reason for using the raster scan instead of the 2D detectors in this work is that the measurements of the beam profile in the focus position were performed in vacuum, which makes it impossible to use most of the commercially available detectors with the integrated electronics.

It showed a good response for both THz and XUV pulses, therefore it was preferable to use it for both beams for consistency of the results. XUV photons being very energetic, created high heat load on the absorbing layer of the detector. Therefore, in order to avoid the damage, the XUV beam was attenuated by Si_3Ni_4 transmission filters in the BL3 beamline, while the THz beam did not need any attenuation. The pyro detector was installed on the holder below the Si sample. The size of the chip of the detector was $2 \times 2\text{mm}$, therefore in order to measure the beam sizes in the order of $100\mu\text{m}$, a pinhole with a diameter of $100\mu\text{m}$ was mounted in front of it. The pinhole is made of stainless steel and has a black oxide coating, which makes it non conductive. The detector was wired to an external power supply and an amplifier outside of the vacuum chamber. This type of pyro detector installation for this particular experiment is highly compact and flexible, which is critical in a geometry with limited space.

The second detector, installed on the sample holder below the pyro detector is a fast XUV photodiode, which was initially used for monitoring the relative pulse energies of XUV pulses in the THz Doubler geometry. Later, when the fast GMD measurements were used, it was no longer necessary to use the XUV photodiode.

By moving the pyro detector of the XUV photodiode in the beam, either spatial overlap or the XUV suppression can be checked during the experiment.

The sample holder was mounted on an X-Y positioner, combined of 2 motorized linear stages from Newport with a total range of movement of 2.5 cm. Detectors and sample positions were chosen to enable the largest possible range of movement, to avoid cutting the beam and to allow for measuring full 2D beam profiles.

The optimal focus of the THz beam was adjusted by moving the 3rd linear stage from OWIS along the Z axis (Fig. 4.6) and measuring the beam profile along the focal axis of the parabolic mirror. THz beam was chosen as a reference for the focal position instead of XUV, because the XUV beam is much smaller than the THz beam, and is focused by a mirror with a much longer focal length, making its focal depth longer.

Once the X-Y central positions of the beams were found, the beams had to overlap spatially. During the preparation time, when the chamber was not pumped, the rough spatial overlap was

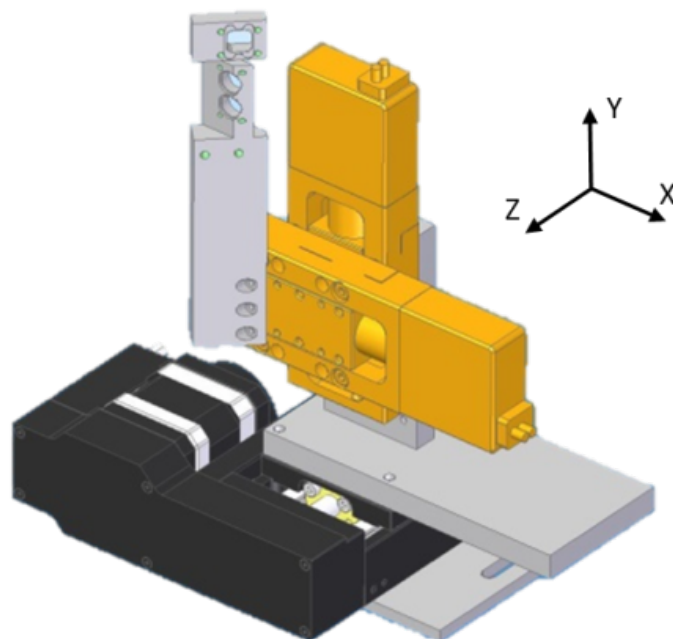


Figure 5.6: Setup for THz and XUV 2D raster scan in the sample position. Pyro detector is mounted on motorized XY-stages on same axis as the Si sample. Additional stage in Z plane to optimize the position of the sample in focus.

established with a camera in the focal position. Once the chamber was pumped, the positions of the beam changed slightly. It was precisely adjusted by the position of the last XUV focusing mirror.

The measurement was done by using the LabView software, specially programmed for this experiment. For the data acquisition, two oscilloscopes VirtualBench from National Instruments were used. The software controlled the acquisition during the scanning, during free movement and the positions of all motorized stages inside the experimental chamber.

The results of the 2D beam profile measurements are presented on the Fig. 5.7. THz beam in the focus has ellipsoidal shape elongated in the vertical direction due to imperfect focusing and misalignment of the coupling into the off-axis parabolic mirror during this particular experiment.

The beam size of the THz beam with the THz undulator set at $100\mu\text{m}$ nominal wavelength is $400 \pm 20\mu\text{m} \times 1470 \pm 30\mu\text{m}$, and at $8\mu\text{m}$ wavelength the diameter FWHM is $180 \pm 15\mu\text{m} \times 320 \pm 15\mu\text{m}$. In order to match the beam size of XUV and THz as much as possible, an aperture was inserted in the XUV beam 30 m upstream of the experiment in the FLASH tunnel [33], to optimize the ratio between beam sizes. The beam size of the XUV beam with a pinhole was $230 \pm 30\mu\text{m}$, without the pinhole $140 \pm 18\mu\text{m}$. The ratio between the areas of the THz and XUV beams is 1:9 for THz at $100\mu\text{m}$ and 2:3 for THz at $8\mu\text{m}$.

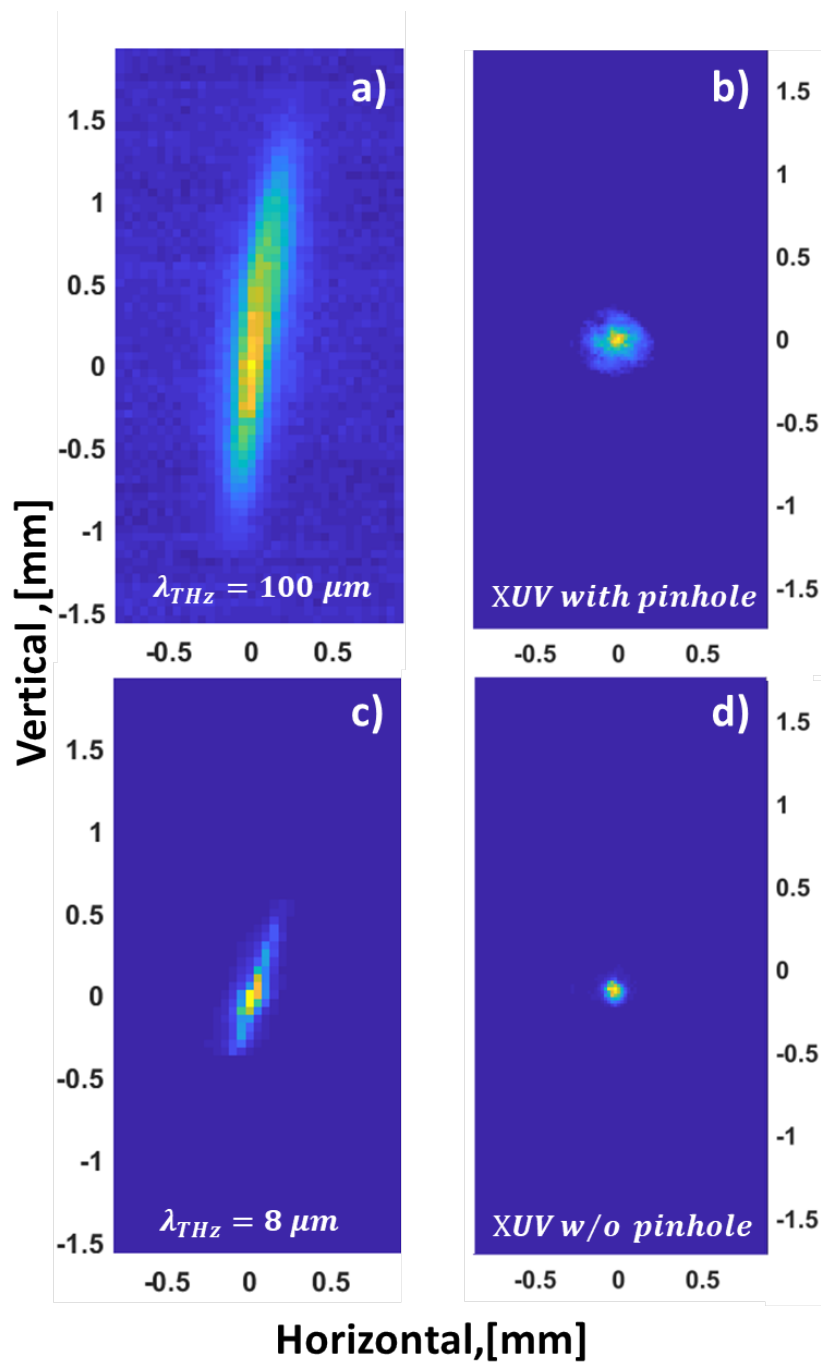


Figure 5.7: Result of the 2D scan and spatial overlap in the focal position in the refocusing mirror geometry. a) THz profile with the $FWHM = 400 \pm 20 \mu m \times 1470 \pm 30 \mu m$ at the wavelength $\lambda_{THz} = 100 \mu m$, b) XUV profile with a pinhole in the FLASH tunnel with the $FWHM = 230 \pm 30 \mu m$, c) THz profile with the $FWHM = 180 \pm 15 \mu m \times 320 \pm 15 \mu m$ at the wavelength $\lambda_{THz} = 8 \mu m$, d) XUV profile without a pinhole with the $FWHM = 140 \pm 18 \mu m$.

5.2.2 Results of the temporal overlap and resolution of the method

Pulse energy of the XUV measured with the GMD was $110 \mu J \pm 20 \mu J$. THz pulse energy, measured inside the THz hutch [27] with a calibrated pulse energy detector through a diamond window was $0.5 \mu J \pm 0.1 \mu J$. The pulse energy meter for THz is installed in the THz hutch [27] separated from the experimental chamber by a few meters. The beam goes through the re-collimating optics until it reaches the experiment, therefore insignificant losses of the pulse energy along this distance are present. Estimated XUV transmission through the beamline of 78 %, according to [33], the refocusing mirror (62 %) and attenuation filters (1.3 %) was around $700 nJ \pm 10 nJ$, yielding the final intensity on the sample as $6.76 \times 10^9 \frac{W}{cm^2}$ and $2.65 \times 10^9 \frac{W}{cm^2}$ for the XUV without and with aperture, respectively.

Measurement of both transmission and reflection of the THz probe pulse on the sample allows one to correct for the pulse-to-pulse fluctuations of the THz pulse energy. The pulse energy fluctuation for THz undulator tuned to $100 \mu m$ is 3.6 % r.m.s. and at $8 \mu m$ it is 14 % r.m.s..

At this point, XUV and THz are spatially and temporally overlapped on the sample. XUV pulse generates free carriers in the Si, which in turn changes its optical properties, that can be observed in the changes of reflectivity and transmission of the probe THz pulse, which was measured. When THz arrives earlier than XUV, the sample experiences no change of optical properties, therefore the measured THz intensity is constant.

Once THz arrives later than XUV (right side of the Fig. 5.8), which creates free carriers, increasing the free electron density in Si, the reflected and transmitted portions of the THz beam change the ratio. This change of the optical properties is measured in the experiment. Results of time-dependent reflectivity measurements (presented as $\frac{(R - R_0)}{R_0}$ where R_0 is the equilibrium reflectivity) are presented in Fig. 5.8.

To gain understanding of the process, it is instructive to study the rising edge of the reflectivity change. The duration of the slope is the convolution of the pulse duration of THz and XUV pulses:

$$\Delta\tau = \sqrt{\Delta\tau_{THz}^2 + \Delta\tau_{XUV}^2 + \Delta\tau_{jitter}^2 + \Delta\tau_{excitation}^2}. \quad (5.8)$$

For the THz wavelength $\sim 100 \mu m$, the measured slope width is $\Delta\tau_{100\mu m} = 2.2 ps$ and for $8 \mu m$ wavelength $\Delta\tau_{8\mu m} = 1.2 ps$ (calculated as the time between the points corresponding to the 10 % and 90% levels of total amplitude of the signal). XUV and THz are naturally synchronized in this experiment, with temporal jitter smaller than 5 fs, therefore its contribution we neglect. We assume that the excitation time of free carriers is much faster than other timescales in this experiment and we neglect it as well [77, 51].

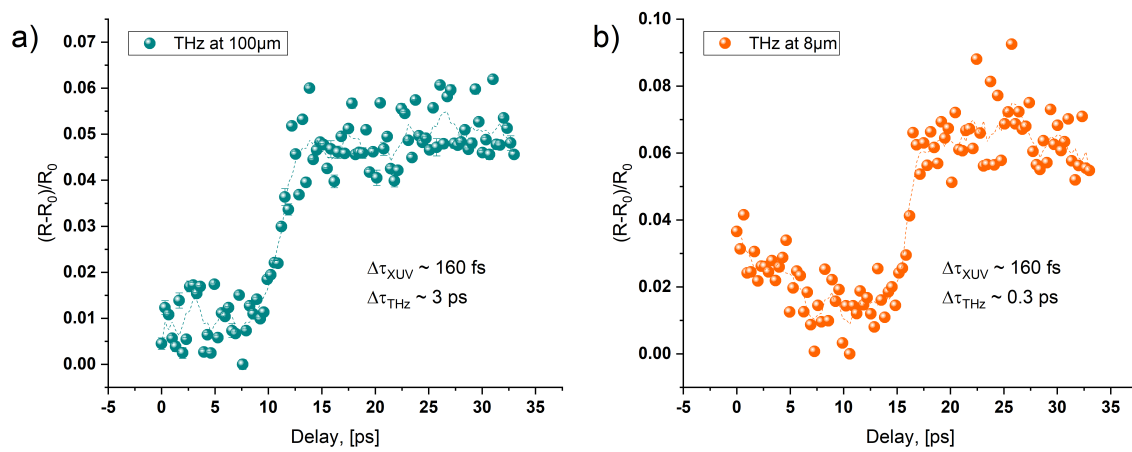


Figure 5.8: Transient THz reflectivity change of Si, excited by 13.5 nm XUV pulse in the refocusing mirror geometry, probed with two THz wavelengths: a) for $\lambda_{THz} = 100\mu m$ the slope width is $\Delta\tau_{100\mu m} = 2.2$ ps and b) for $8\mu m$ - $\Delta\tau_{8\mu m} = 1.2$ ps

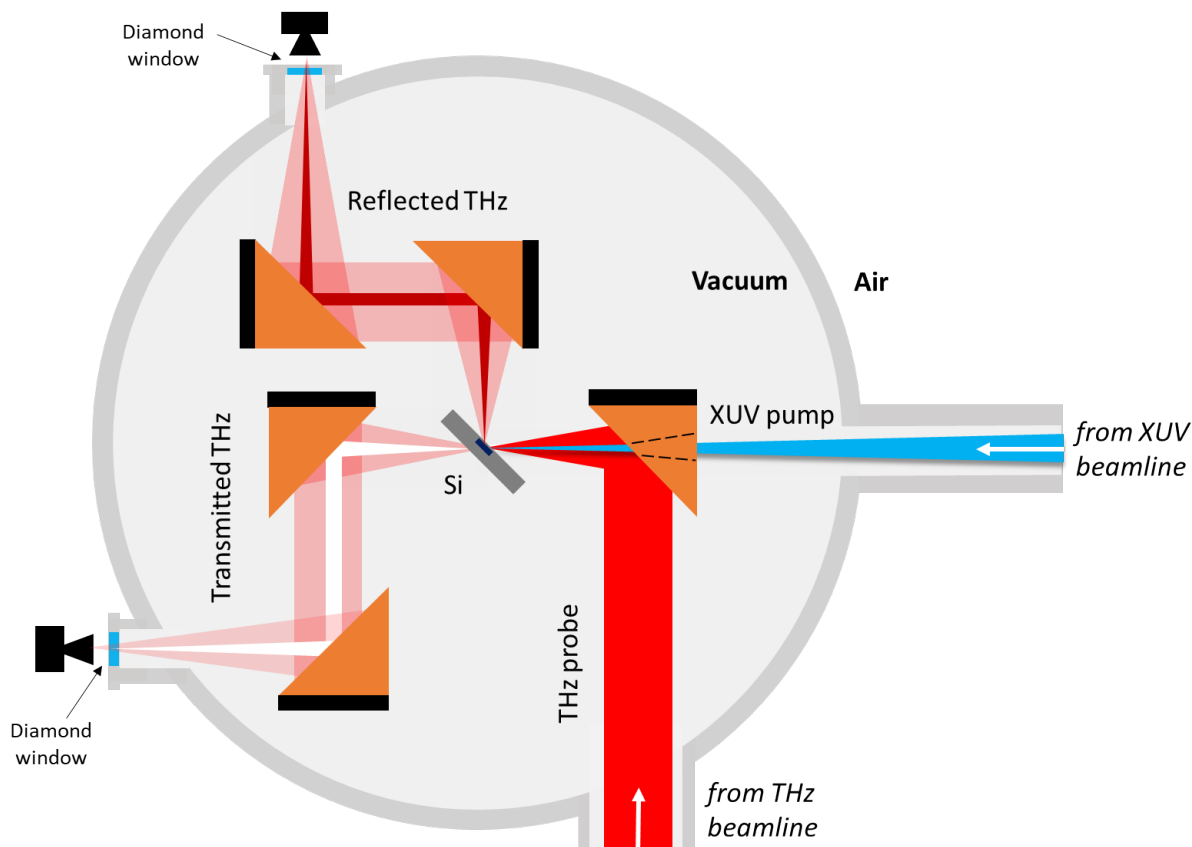


Figure 5.9: Scheme of the experimental setup for XUV plasma switch experiment in the THz Doubler geometry. XUV and THz beams are focused collinearly on the Si sample, matching the arrival time of the 1st THz pulse and 2nd XUV pulse of the Doubler scheme.

5.3 THz Doubler geometry

A second step in the evaluation of the applicability of the THz Doubler scheme for pump-probe experiments at FLASH is the XUV plasma switch experiment in the THz Doubler geometry. The internal geometry of the experiment differs from the scheme in the previous section (see Fig. 5.2 for the previous scheme), because of the different positions of the incoming beams.

The new scheme of the experimental chamber is presented on Fig. 5.9. The difference from the previously described in the section 4.2 of this thesis scheme is that the XUV is focused on the sample using a focusing mirror that reflects the XUV beam with 6° deflection, at so-called grazing incidence angle at beamline BL3 at FLASH [33]. Because of the large incidence angle and the appropriate coating, this mirror is suitable for a broad range of XUV spectral range (4.2 nm - 100 nm) and therefore does not limit the wavelength choice during the experiment. This mirror has a focal length of 2m and is used to focus the XUV beam on the pure Si sample at the incidence angle of 45° .

On contrary to the previous scheme, here XUV and THz are focused collinearly and overlapped in focus. The THz beam is split into 2 parts by the Si wafer: one part is transmitted and one is reflected. Both reflected and transmitted beams are picked up and collimated by off-axis

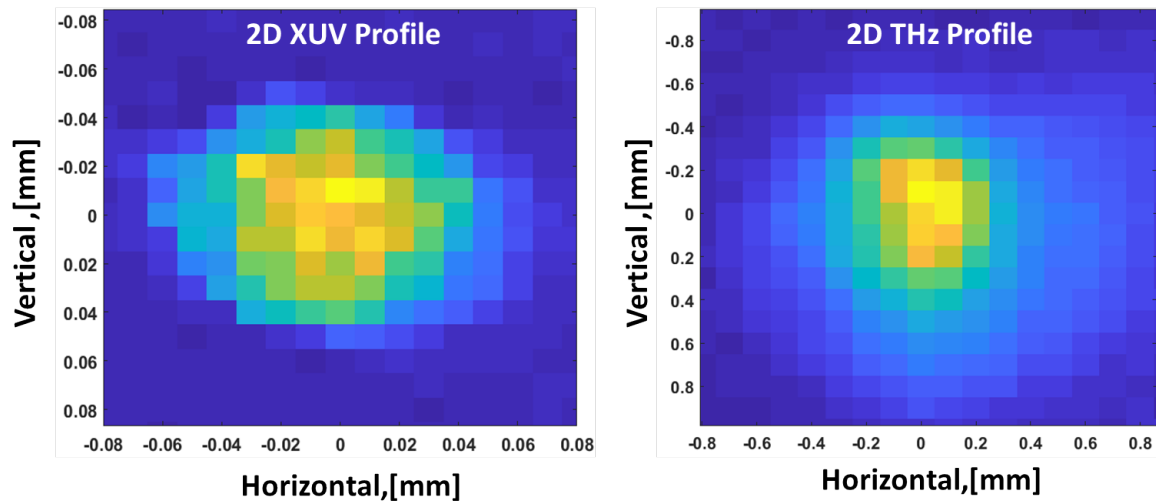


Figure 5.10: 2D beam THz and XUV profiles with the Doubler geometry in focus. Left: XUV beam at 11.5 nm with the beamsize in focus of $77 \pm 10 \mu\text{m} \times 85 \pm 10 \mu\text{m}$ FWHM and THz beam at $100 \mu\text{m}$ with $330 \pm 20 \mu\text{m} \times 640 \pm 30 \mu\text{m}$ FWHM.

parabolas and later focused on the pyro detectors outside the chamber. The sample is the same high resistivity ($>2000 \text{ Ohm} \times \text{cm}$) undoped Silicon from CRYSTECH which was used in the previous plasma switch experiment in the refocusing mirror geometry.

In this scheme the experimental chamber vacuum is separated from air with diamond windows made by chemical vapor deposition (CVD) from DIAMOND MATERIALS (for transmission curve see Fig. 2.7 of this thesis). Diamond is known to have excellent transmission for the broad spectral range. Diamond window is an upgrade for the experiment and was not available for the previous scheme with the refocusing mirror geometry (ZnTe was used there).

The probing wavelength of THz was $100 \mu\text{m}$ and the wavelength of XUV was 11.5 nm. 2D beam profiles were measured by the same technique as described in the section 4.2.1, with a smaller pinhole in front of the pyro detector. This time the pinhole had the diameter of $50 \mu\text{m}$. Measured beam size of the XUV in focus is $77 \pm 10 \mu\text{m} \times 85 \pm 10 \mu\text{m}$ FWHM, which is 2 times smaller in comparison to the values measured in the previous experiment. THz focus size is $330 \pm 20 \mu\text{m} \times 640 \pm 30 \mu\text{m}$ FWHM. The results of the 2D beam profiles are presented in the Fig. 5.10. Having a longer beamtime available, it was possible to optimize the THz focus better and more consequently, which made the THz focus smaller than in the previous THz plasma switch experiment, presented in the previous section.

Full power of XUV without the attenuation was less than $1 \mu\text{J}$ for the first pulse and $21 \mu\text{J} \pm 2 \mu\text{J}$ for the second pulse. THz pulse energy measured with the calibrated THz pulse energy meter through the diamond window in the THz hutch was $3.4 \pm 0.4 \mu\text{J}$ for the 1st pulse and $1.2 \pm 0.1 \mu\text{J}$ for the 2nd.

The temporal scan of THz pulses with respect to XUV with an optical delay and the effect of the reflectivity switch in the overlap position are presented in Fig. 5.11. The scan was performed for different filters for XUV in order to estimate the lowest limit of the effect. With XUV pulse

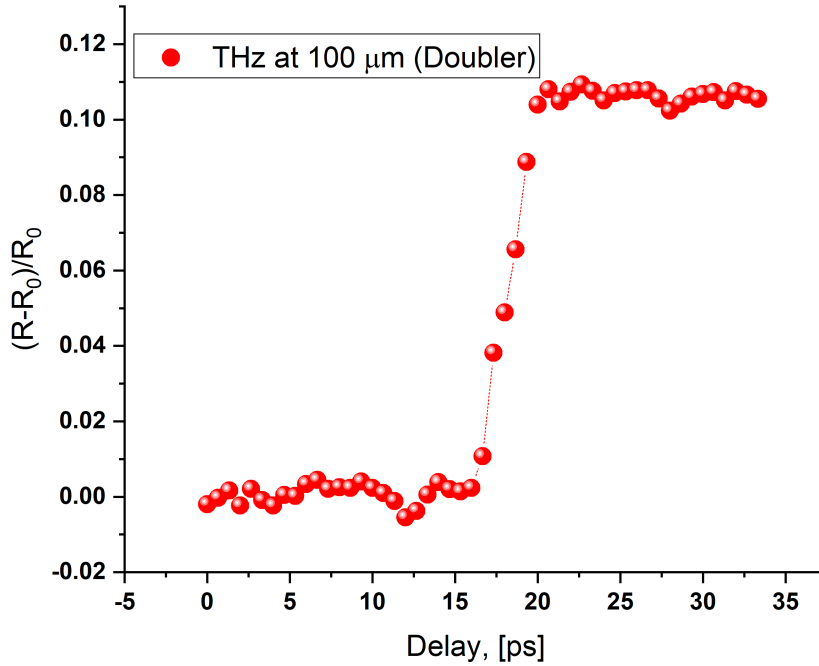


Figure 5.11: The transient optical reflectivity curve for THz for Si sample measured in the THz Doubler geometry. The duration of the reflectivity slope is 2.4 ps.

energy after the attenuation with Si_3N_4 filter of 350 nm thickness being 13.6 nJ, the measured effect of the change of reflectivity is 12 %.

It was assumed that the jitter between XUV and THz pulses from 1st and 2nd electron bunches is less than 19 fs r.m.s, as shown in the section 4 of this thesis. It is safe to assume that the jitter between 1st and 2nd THz pulses is as well 19 fs r.m.s. or less. The duration of the reflectivity slope is defined as a convolution of pulse duration of XUV, THz and the jitter, and in this case we again like last time can neglect the jitter and excitation time values.

The width of the reflectivity change slope, (calculated as the time between the points corresponding to the 10 % and 90% levels of total amplitude of the signal) gives the FWHM = 2.4 ps, which closely corresponds to the pulse duration of THz pulse at 100 μm wavelength at FLASH. No significant further contribution to temporal jitter between XUV and THz pulses in the THz Doubler scheme can be derived from this data.

In order to estimate the sensitivity of the XUV induced plasma switch for THz, series of measurements with different XUV fluences were performed. XUV pulse energy was attenuated with different combinations of XUV attenuation filters. The results are presented on Fig. 5.12. Different combinations of attenuation filters were used: Si_3N_4 850 nm (red line), Si_3N_4 350 nm + Nb 405 nm (orange line) and Si_3N_4 500 nm (green line). The effect of the plasma switch in THz spectral range is very efficient and can be clearly observed even at XUV fluences as low as $45 \frac{\mu J}{cm^2}$. Due to the lack of available attenuation filters and limited amount of the beamtime, it

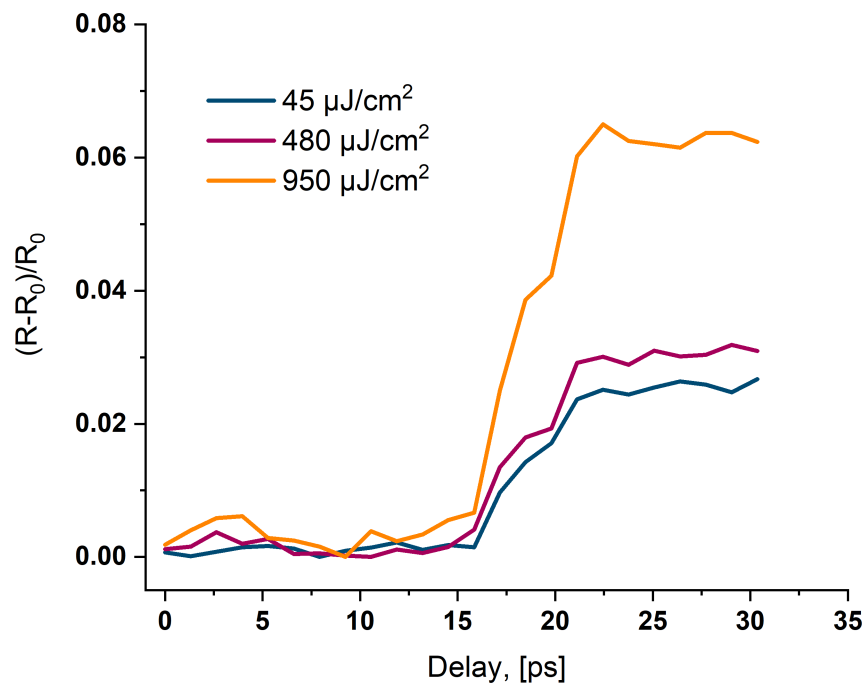


Figure 5.12: Pump fluence dependence of Si

was not possible to reduce the XUV fluence in a fully controllable fashion. However, estimating from the contrast ratio of the pumped/un-pumped reflectivity changes, it can be assumed that the threshold for the plasma switch is below this fluence. These results demonstrate the efficiency of the method, allowing performing the time overlap experiment with not very demanding setup of the machine. It does not require neither tight focusing nor high pulse energies.

In the real-life applications as a temporal and spatial tool, this experiment can be performed during the accelerator setup time, using only a small portion of the THz and XUV beams, or if technically possible - in parallel to the main experiment.

5.4 Comparison to the experiment in the refocusing mirror geometry

The aim of this work was to perform the proof-of-principle experiment in two geometries (refocusing mirror and THz Doubler) and to show the feasibility of the THz Doubler scheme for the future experiments. In conclusion, the results show the following:

- The results obtained with the new scheme are comparable to the results with the refocusing mirror scheme

- Good suppression of the 1st XUV pulse and the good tunability for high pulse energy of the 2nd pulse (starting from 1 μJ optimization up to 40 μJ) ensures that the 1st pulse does not create disturbances in the investigated system before the probing THz pulse and the main 2nd probe XUV pulse come (the pulse energy ratio between XUV pulses $\frac{E_{2^{nd}UV}}{E_{1^{st}UV}} = 18$ or more). Therefore, it is comparable to the scheme with the XUV refocusing mirror.
- The plasma switch experiment with the THz Doubler scheme was performed using XUV wavelength of 11.5 nm, which demonstrates that the new scheme is comparable to the refocusing mirror geometry and can potentially replace it. In the future FLASH2020 project, where the fixed-gap are going to be replaced with variable gap XUV undulators at FLASH1, it will be possible to change the wavelength during the experiment on demand without the need to replace the critical components inside the experiment, such as the refocusing XUV mirror.

5.5 Future perspectives for the single shot XUV plasma switch for THz

Measuring the change of optical properties of materials in a single shot way allows to access the non-reproducible effects of strongly excited materials with very high temporal resolution. This is important, for example, for measuring the material properties at the edge of their damage threshold. Such experiments require high level of complexity with the temporal and spatial overlap of three sources of radiation: THz, XUV and the optical laser.

One of the examples of such experiments is the XUV plasma switch, probed with THz, which is further analyzed with the tilted pulse front spectral decoding in a single shot way. The XUV plasma switch part is similar to the experiment described in the previous section and the single shot THz detection is based on using the echelon mirrors [78, 79, 80, 81, 44].

Echelon mirrors have a step-like surface structure and split the probe laser pulse into multiple beamlets which have a fixed relative time delay with respect to each other. Depending on the experiment, the echelon mirrors can be used either in transmission (propagation through the glass) or in reflection (reflection on metal coated surface). The reflection geometry has the advantage for the detection of higher THz frequencies in comparison to the transmission geometry, because it does not introduce additional chirp on the laser pulse. Plus, the material of the transmissive echelon prisms might suffer from the defects of the components during the manufacturing, because they are typically composed of quartz glass and epoxy glue [80]. The reflected laser pulse also does not gain broadening, as it would do when passing through the dispersive material.

Here the THz detection principle with 1D echelon mirrors and results of the single shot XUV plasma switch experiments performed at FLASH will be described.

5.5.1 Tilted pulse front single shot encoding

The total delay Δt and the temporal resolution of this scheme is defined by the height h and the number of steps on the echelon surface m : $\Delta t = \frac{mh}{c}$, where c is the speed of light in vacuum. After the echelon mirror laser beam propagates collinearly with the THz pulse onto the detection EO crystal, where both are focused on the same spot. The time-separated laser beam components overlap in the focus with a 2-lens imaging system but they are separated after the focus and spatially resolved on a 2D CCD detector. See Fig. 5.13 for details.

Like in the previously described techniques, the modulation of the laser polarization by THz is transformed into the intensity modulation by a combination of a Quarter wave plate (QWP) and a Wollaston prism. The Wollaston prism separates the crossed-polarized components of the laser and both of them are imaged on the same CCD detector. The THz profile is encoded on both images and the resulting electric field of THz can be retrieved by subtracting one signal from another and taking into the account the original intensity without the THz pulse (I_0):

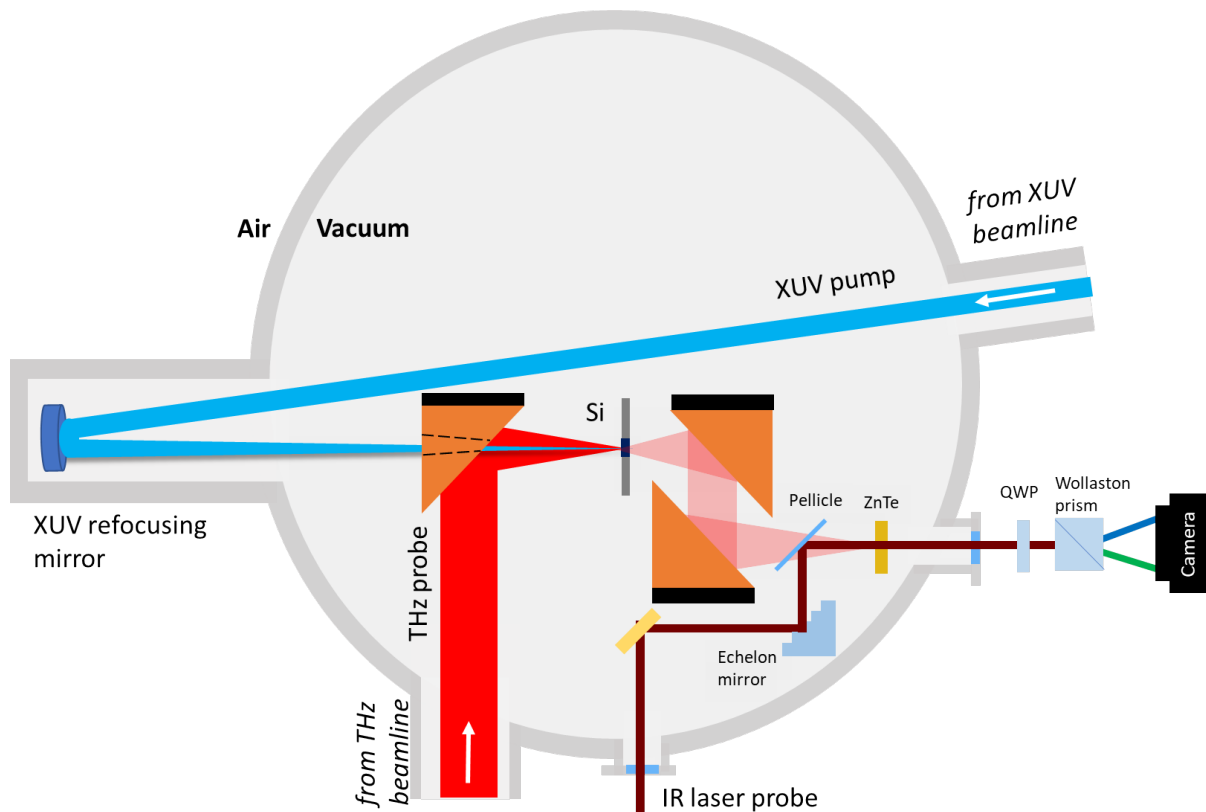


Figure 5.13: Schematic illustration of the tilted pulse front encoding setup. The probing laser pulse is reflected off the echelon mirror with a fixed height of the steps, introducing a 6 ps total time window. After the echelon mirror is is focused with a 2-lens imaging system on the EO detection crystal and overlapped with THz pulse in focus. After the crystal, the laser polarization components are split with a quarter wave plate (QWP) and Wollaston prism and imaged on the CCD camera.

$\frac{\Delta I}{I_0} = \frac{\Delta I_R}{I_0} - \frac{\Delta I_L}{I_0}$, where ΔI_R and ΔI_L are right and left images on the camera, corresponding to opposite polarization components.

This method allows measuring THz profile in a single shot, avoiding the spectral artefacts present in the single shot spectral decoding scheme.

During the user beamtime of Chen et. al from SLAC at FLASH (beamtime proposal number F-20171090) it was demonstrated that using echelon single shot technique for measurement of the THz transmission through the excited sample, allows for the precise XUV-THz temporal overlap with the THz sub-cycle precision (in this work down to 300 fs) [81, 82]. XUV wavelength was set to 13.6 nm, THz wavelength - to 100 μm (3 THz) central wavelength. The complete description of the setup and the experiment performed by the user group is going to be published in 2020.

For the time overlap measurements XUV and THz pulses were collinearly focused on the 500 μm thick pure high resistivity Si wafer in a vacuum chamber (see Fig. 5.13). When THz pulse hit the sample earlier than the XUV pulse, the THz was transmitted without changes. XUV pulse excited the Silicon and created free electrons, with the electron density sufficient to make the sample highly reflective for THz range and to reduce the transmission. Therefore when XUV and THz were temporally overlapped, the transmission of the THz pulse changed as fast as the pulse duration of the XUV. The THz single shot detection method allows to detect the change of THz transmission within the THz electric field profile.

Linearly polarized laser pulses, provided by the FLASH laser group and synchronized to the FLASH accelerator had a central wavelength around 800 nm with a bandwidth of 50 nm [1]. The laser pulse was expanded with a telescope and then reflected from the echelon mirror with 150 μm (500 fs) large steps height, which distributed the split laser beamlets over a total time window of 6 ps. The small steps of 7.5 μm (25 fs) define the temporal resolution of the created laser pulse pattern. The laser and THz beam were collinearly focused and overlapped on the ZnTe crystal. The laser beam is collimated after the ZnTe crystal with a lens with the same focal length as the focusing one.

THz induced the change of the polarization for every beamlet of the split laser beam along the whole time window of 6 ps. The change of the polarization was transformed to the change of intensity by the same method like in a spectral decoding setup: by a half wave plate, quarter wave plate and a Wollaston prism. The two crossed polarization components are sent to the CCD camera and produce symmetric pictures, imaging the echelon mirror and therefore encoding the laser pulse in XY picture.

The single shot traces of the THz transmission measurements with and without XUV pulse are shown of the Fig. 5.14. The background of the laser, measured without THz and XUV, was subtracted. Comparing the retrieved THz field shape with (red curve) and without XUV (blue curve), it can be seen that at the moment of time-overlap with the XUV, the intensity of THz has a sharp drop. Therefore these results demonstrate the capability of the single shot echelon

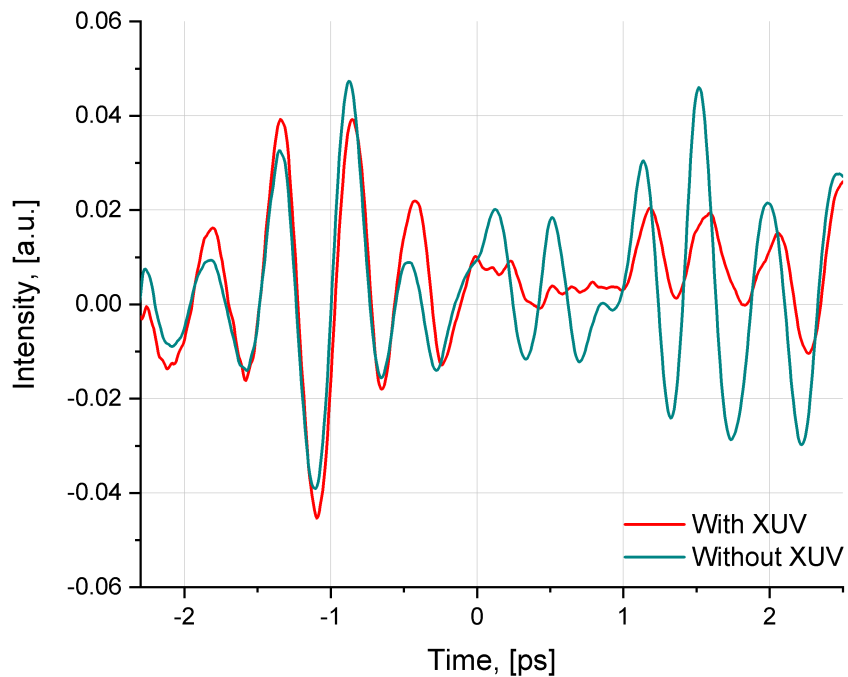


Figure 5.14: XUV-THz single shot arrival time measurement using the echelon mirror. Two examples, showing the THz transmission change before (green) and after the excitation (red) of Si with an intense XUV pulse at different relative arrival times of XUV and THz pulses. The time zero corresponds to the arrival time overlap between THz and XUV. The reduction of the intensity of THz can be well seen within the THz pulse length.

detection technique to find temporal overlap between XUV and THz within the period of the THz field cycle.

The presented results are the first demonstration of the single shot XUV-THz plasma switch, measured at 10Hz repetition rate. Future developments will include the operation in a burst mode at 200kHz repetition rate, using a line camera.

Chapter 6

Lamellar Grating Spectrometer

The THz spectral region is very interesting for a broad range of fields from astronomy observations, biology, security and up to THz driven miniature plasma accelerators [83],[84]. THz spectroscopy was first investigated and mostly developed in the early years of 20th century, when the first observations and study of the properties of space objects like galaxies and planets, their temperatures, dynamics and density were performed. It pushed for the developments of special Fourier-transform spectrometers, interferometers and optics in this range. At FELs and laser laboratories, spectral characterization of broadband THz pulses is of high importance and FTIR spectroscopy can be an ideal solution.

A common method to measure the spectrum of THz radiation at FLASH is electro-optical sampling (EOS)[9], where the measured electric field of the pulse is transformed into spectral domain. EOS, being an established technique for THz characterization is a sophisticated experiment on its own and takes a lot of time. For the purpose of the spectral characterization of the source and at times when the knowledge of the electric field is not required, a more robust and quick device is needed. Therefore, the Fourier transform infrared (FTIR) spectroscopy is a potential solution for this type of measurements.

Reflective lamellar grating interferometers divide the wave front spatially, unlike most popular Michelson interferometer (based on splitting the amplitude of the beam) [85, 86, 87, 88]. Because of this, lamellar grating design has the key advantages: high (close to 100%) and smooth efficiency response (e.g. typical Fabry-Perot interferences that plague Michelson interferometers are absent). Because of their unique design, they allow the measurements in extremely large spectral ranges. Lamellar gratings are also found in extreme ultraviolet (XUV) spectroscopy and metrology [89, 90].

Due to its high efficiency, it is also a suitable tool for the experiments where high sensitivity is required, for example on water, where the absorption of THz is the highest. Recent research [91] also demonstrated the breakthrough result of generating THz from thin layers of water. A highly efficient THz spectrometer is essential for these types of experiments.

Gratings for THz are typically designed with a blazed reflection grating for a specific wavelength for λ or relatively narrow band (less than one octave) of the spectrum and sub-

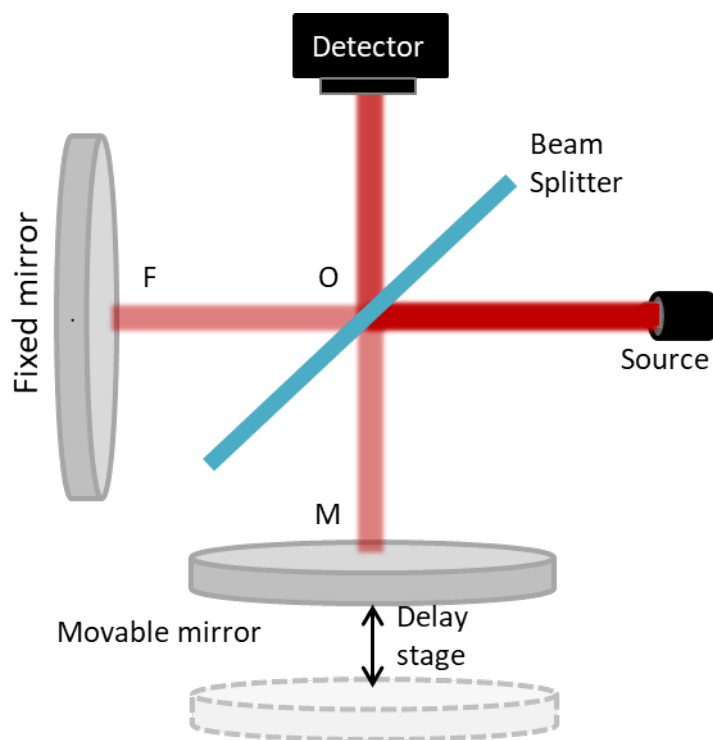


Figure 6.1: Scheme of a Michelson interferometer

harmonics ($\lambda/2, \lambda/3, \text{etc.}$). The size of the entrance and exit slit of the grating spectrometer also defines the bandwidth of the selected range. For measurements in a broad spectral range interferometers are better suited than grating spectrometers because they can measure the full spectrum of the source at once and they are quite flexible in the construction.

The following chapter gives an overview on the fundamentals of FTIR spectroscopy and introduces the lamellar grating spectrometer, specially developed for spectral characterization of the broadband THz source at FLASH.

6.1 Fourier-transform Infrared spectroscopy

The principle of the Fourier-transform spectroscopy, interferogram generation and the further analysis is presented in this work using a Michelson interferometer as an example. In Michelson interferometer the original beam is split into two replicas by using an efficient (ideally 50/50) beamsplitter and the two replicas are travelling a different path and delayed with respect to each other [86, 92]. After recombination of the two parts of the beam and focusing them on the detector, they interfere with each other. A simple scheme of a Michelson interferometer is presented on the Fig. 6.1.

In spectroscopy it is common to describe radiation frequency in wavenumbers ν_0 in cm^{-1} , which corresponds to the number of wavelengths per unit distance (per cm) as $\nu = \frac{1}{\lambda}$. For further discussions it is convenient to assume that the beamsplitter is ideal and splits the intensity of the beam equally. In this case if the initial intensity of the source is $I(\nu_0)$ then the intensity

of each branch of the beam reaching the detector is $I(\nu_0)/4$. The optical path difference or the retardation δ between the beams which reflect from the fixed and from the movable mirror is equal to $2(OM - OF)$. In the configuration when $OM = OF$, the path difference between the beams is 0 and can be referred as the zero path difference (ZPD) or zero retardation. At this position the two beams are in phase with each other: each of the beams experience the shift of 270° , have a zero retardation and therefore interfere constructively. The interference record for the source with the central wavelength λ_0 , corresponding to ν_0 wavenumber, measured by the detector can be described as a function of the retardation between the beams as following:

$$I'(\delta) = 0.5I(\nu_0)\left(1 + \cos 2\pi \frac{\delta}{\lambda_0}\right), \quad (6.1)$$

Therefore, when the retardation δ is equal to a full number n of wavelengths $n\lambda$, the interference is constructive and when δ is equal to $n\frac{\lambda}{2}$, the interference is destructive.

The modulated component of the equation 6.1 describes the interference term:

$$I(\delta) = 0.5I(\nu_0) \cos 2\pi \delta \nu_0, \quad (6.2)$$

In the real world, the beamsplitter is not ideal but has the dependency on the wavenumber ν and the detector response might be spectrally dependent and non-linear or any other parts of the system might affect the final measurement. In this case the interferogram $S(\delta)$ can be simply described as a combination of the effects of different components of the system:

$$S(\delta) = B(\nu_0) \cos 2\pi \delta \nu_0, \quad (6.3)$$

where $B(\nu_0)$ represents the intensity of the source at the wavenumber ν_0 , taking into the account the system's characteristics.

For a continuum source, the interferogram can be presented as:

$$S(\delta) = \int_{-\infty}^{+\infty} B(\nu) \cos 2\pi \nu \delta d\nu \quad (6.4)$$

In order to get the spectrum out of this interferogram, the Fourier transform (FT) must be applied to it. $B(\nu)$ is the spectral representation of the measured interferogram, obtained by scanning the movable mirror within the range of the linear stage $0 < \delta < L$:

$$B(\nu) = \int_0^L S(\delta) \cos 2\pi \delta \nu d\delta, \quad (6.5)$$

In order to record the interferogram correctly, it is important to take into account several parameters. First of all, if the interferogram is double sided (the mirror moves in both directions from the ZPD), it is necessary to do the scanning symmetrically around the ZPD. This can be explained when the interferogram is rewritten as following:

$$B(\nu) = \int_{-l}^{+l} S(\delta) \exp^{i2\pi\nu\delta} d\delta, \quad (6.6)$$

where l is the maximum retardation on the stage in one direction. When the exact ZPD was not found and the interferogram was sampled around a position where $\delta = 0$ but exponent in the equation 6.6 is not 0, and actually is a function of ν , then the phase shift occurs. The interferogram can therefore be rewritten as:

$$B(\nu) = \int_{-l}^{+l} S(\delta) \exp^{i(2\pi\nu\delta + \phi(\nu))} d\delta, \quad (6.7)$$

The resolution of the spectrum, measured with any kind of interferometer is defined by the maximum optical path difference OPD between two beams:

$$\Delta\nu = \frac{1}{OPD} = \frac{1}{2l} \quad (6.8)$$

Even if the resolution and the signal to noise ratio of the interferogram are very good, the phase shift can cause difficulties and artefacts when applying the Fourier transform to retrieve the spectrum. In this case the complex Fourier Transform is required instead of the cosine Fourier transform, which is easier to calculate. In order to prevent these problems, it is preferable to measure double-sided interferograms well as to apply phase-correction filters or apodization windows. Apodization windows are functions in the spectral domain which are normally used to suppress the sidelobes of the fourier transformed signal. When the resolution of the spectrometer is higher than the narrowest feature of the measured spectrum, then apodization might on the other hand degrade the resolution. When the spectral features are broader than the resolution, then the apodization serves as a smoothing function. The choice of the right filtering depends on the experiment and the required accuracy [92].

One more benefit of sampling two-sided interferograms rather than single-sided is the improved signal-to-noise ratio. In case of double-sided measurement, the data on both sides around the ZPD repeats itself but the noise is different, therefore collecting the data twice leads to an improved S/N ratio by $\sqrt{2}$. Although the measurement time will be increased.

Sampling frequency of the interferogram is another important parameter to take over. According to the Nyquist criterion, an interferogram can be sampled without the loss of information, if the sampling frequency is double, or greater the highest frequency of the studied system $f_{sample} \geq 2f_{max}$. In order to measure a good quality interferogram with the desired spectral resolution $\Delta\nu$ for the source with the limited spectral range up to ν_{max} the sufficient number of sampling points would be equal to:

$$N_s = \frac{2(\nu_{max} - \nu_{min})}{\Delta\nu}, \quad (6.9)$$

Concluding this section, the following parameters need to be considered when designing a general interferometer: the length of the stage to define the scanning range and therefore spectral resolution of the measurement, and the exact ZPD to avoid the phase errors.

6.2 Lamellar Grating spectrometer

Michelson interferometer has some disadvantages when it comes to measuring the radiation in a broad far infrared and THz spectral range. The main problem is the beamsplitter efficiency across the large wavelength range, such as for example of the THz source at FLASH. Most of the materials have a good transmission in a relatively narrow range and due to absorption. A suitable material for a beamsplitter the broadband THz detection would be diamond, but because of the high price, it is normally not possible to use it as a beamsplitter for beams with a large diameter (50 mm or larger), to accommodate for the broadband beam at FLASH, which needs to be collimated within the interferometer. A lamellar grating interferometer (LGI), contrary to the Michelson, splits the wave front instead of the amplitude, which allows for much higher efficiency, reaching almost 100 %.

The design of the lamellar grating interferometer is fairly simple: two parts of a mirror (so called lamellas), interleaving with each other, are equally illuminated by the incoming beam, splitting it into two parts. One part of the mirror is fixed, and another part is mounted on a movable linear stage. When moving the linear stage with the mirror, an optical path difference is introduced and like in the Michelson interferometer, the two parts of the beam interfere.

Being an interferometer, the lamellar grating has an advantage over the typical grating spectrometer for the broad spectral range just like any Fourier-Transform interferometer does, but it has restrictions, which come from the diffraction limits, from which the grating spectrometers also suffer. Some of these limitations can be avoided by the careful design of the lamellar grating geometry, which is the most optimized for the investigated spectral range.

The fringes of the lamellar grating can be treated as an array of rectangular apertures with the variable displacement d between them. Therefore, the reflected light from the lamellar grating experiences diffraction. The diffracted waves from every single facet with the period a are diffracted at an angle α (see Fig. 6.2 for the schematic) and interfere in the focal plane on the detector.

Constructive interference of waves is present when the grating equation is fulfilled:

$$m\lambda_c = a\sin\alpha, \quad (6.10)$$

where m is an integer representing the order of interference.

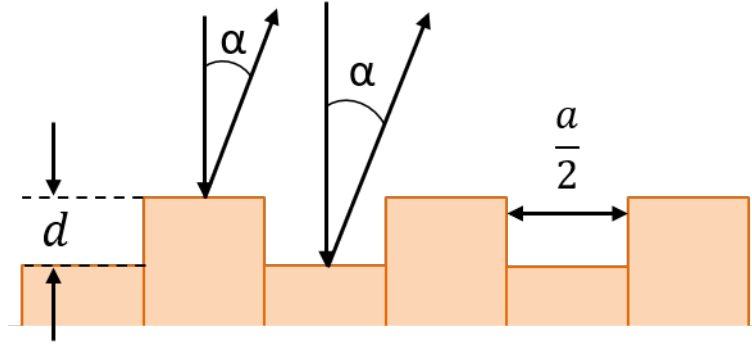


Figure 6.2: Schematic of the diffraction of waves on the lamellar grating at an angle α with the grating constant a and the displacement d between the fringes.

6.2.1 Choice of parameters

The short wavelength limit of the efficiency of the lamellar grating interferometer is defined by the separation between the diffraction orders. If the 0th and +1 or -1 diffraction orders overlap on the detector, then the measured interferogram signal is reduced, which affects the resolution and therefore the ability to measure shorter wavelengths. Fig. 6.3 shows the calculation of the positions of diffraction orders for different wavelength in the THz range and the principle of the diffraction order mixing on the detector.

In order to avoid the mixing of the first order diffracted beam a slit can be installed. Depending on the size of the detector, its own aperture can play the role of the slit. The short wavelength λ_{min} limit, following [93, 92, 87], is defined as:

$$\lambda_{min} = sa/f, \quad (6.11)$$

where s is the diameter of the detector aperture, f is the focal length of the focusing element (e.g. parabolic reflector).

Lamellar gratings also have the limit for the long wavelengths. According to [86] and [87], at the wavelength λ_{max} the cavity effect starts to take place. If the separation between the grooves (OPD) is very long, this optical system can be considered as a waveguide. According to [94], for the transverse electric mode TE_{01} of the wave propagation in a waveguide, the group velocity V_g is equal to:

$$V_g = c \sqrt{1 - \frac{1}{(a/\lambda)^2}}. \quad (6.12)$$

From this definition follows, that for waves with wavelength $\lambda > a$ the group velocity V_g becomes imaginary, therefore these waves can not propagate in the waveguide with the width a .

The TE_{01} mode travels with the velocity V_g , which is different from c , therefore the effective optical path difference δ_{eff} relates to the geometrical optical path difference δ as following:

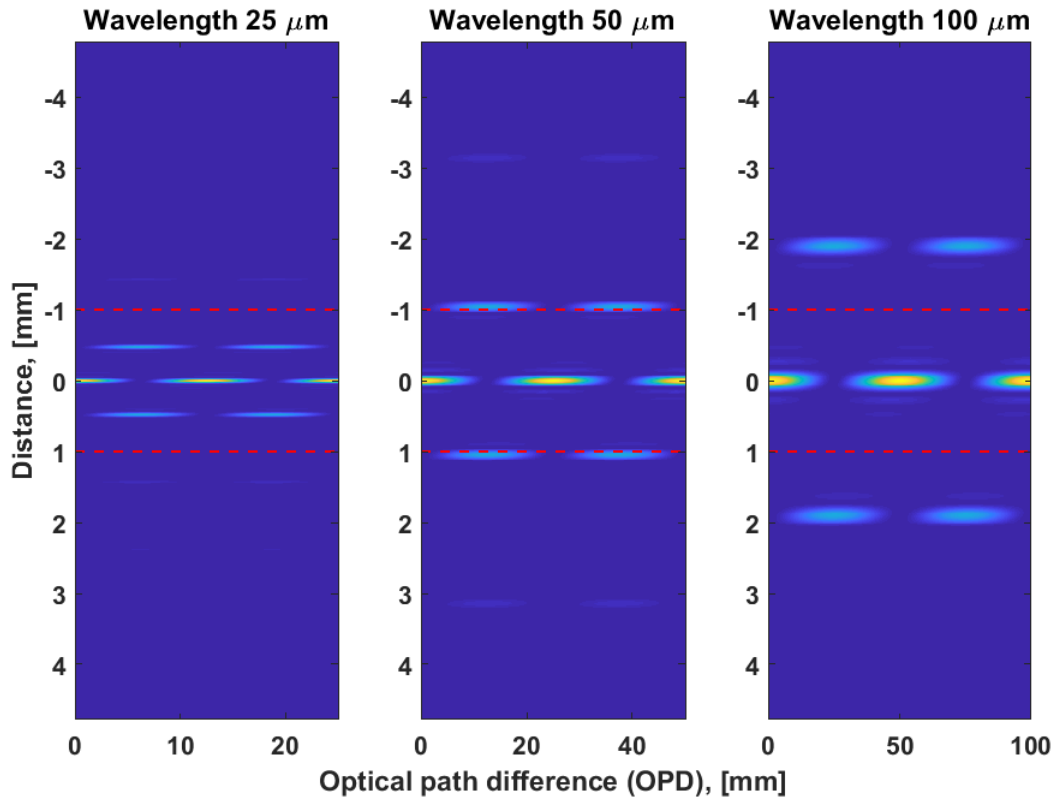


Figure 6.3: Calculated diffraction orders position for the lamellar grating with 10 grating periods with the period of 4 mm for three different wavelengths in the THz range: $25 \mu\text{m}$ (left), $50 \mu\text{m}$ (middle) and $100 \mu\text{m}$ (right). The red dashed line indicates the size of the detectors aperture, used in this thesis (2 mm diameter). The distance between the diffraction orders depends on the parameters of the setup. The critical short wavelength, at which higher diffraction orders enter the slit of the detector is λ_{min} .

$$\frac{\delta_{eff}}{\delta} = \frac{c}{V_g} = \frac{1}{\sqrt{1 - \frac{1}{(a/\lambda)^2}}} \quad (6.13)$$

It was found in [86], that the ratio $\delta_{eff}/\delta \simeq 1.05$ be less than 5% to make the lamellar grating reliable. This limitation comes from the different optical path, which parallel and perpendicular polarization components of the electric field travel. It leads to the artefacts in the spectrum, as two separated monochromatic lines. From this ratio it follows that the longer wavelength λ_{max} limit can be defined as:

$$\lambda_{max} \leq \frac{a}{3.2} \quad (6.14)$$

The geometry of the lamellar grating should be chosen with respect to the spectral range of the characterized source. THz source at FLASH has a very broad spectral bandwidth, in the range from $\lambda_{min}^{source} = 1\mu m$ to $\lambda_{max}^{source} = 300\mu m$.

From the equation 6.14 follows, that the period of the lamellar grating a should relate to λ_{max} as: $a \geq 3.2\lambda_{max}$. Therefore in order to cover the long wavelength limit of the THz source at FLASH ($\lambda_{max}^{source} = 300\mu m$) the grating period must be: $a \geq 960\mu m$.

To cover the short wavelength limit of the source ($\lambda_{min}^{source} = 1\mu m$), the focusing optics and the size of the detector must be chosen carefully, in order to avoid the mix of higher diffraction orders, as follows from the equation 6.11 it can be achieved with various combinations of the focal length f and the slit size s , for example with $f = 100mm$ and $s = 0.1mm$.

The lamellar grating parameters in this work differ from the described ideal case above. It has the grating period $a = 4mm$ (width of individual fringes $h = a/2 = 2mm$), focal length of the parabola $f = 100mm$ and the aperture at the detector $s = 1mm$. With this configuration, the lamellar grating is the most efficient within the spectral range between $80\mu m$ and $1250\mu m$.

The resolution of the measured spectrum is defined by the maximum OPD of the scan

$$\Delta\nu = \frac{1}{OPD}. \quad (6.15)$$

Therefore it can be chosen for every measurement, according to the available time and requirements. In this work the maximum OPD, produced by the linear stage was $l = 12mm$, therefore maximum achieved resolution is $\Delta\nu = 0.42 \frac{1}{cm}$.

6.2.2 Design of the lamellar grating

The lamellar grating interferometer described in this thesis consists of two interleaved gratings, manufactured from 100mm diameter gold coated copper mirror. One is fixed and the other is mounted on the motorized stage responsible for introducing the optical delay between the split beams. A 2 cm thick copper gold coated mirror was chosen because of copper's good thermal conductivity, good polishing quality which allows for high quality coating, as well because it

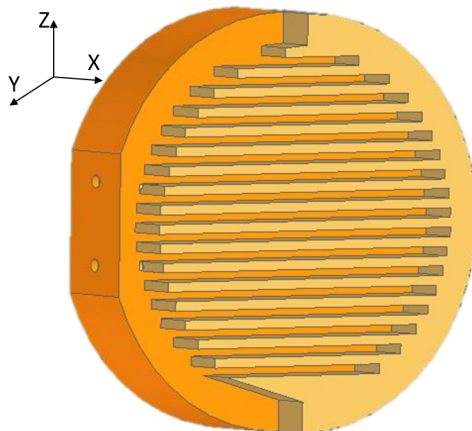


Figure 6.4: Schematic of the lamellar grating, manufactured from 100mm diameter gold coated copper mirror with the width of the fringes $h = 2\text{mm}$.

is possible to cut it with high precision. Cutting of the mirror was performed by the wire-cut electrical discharge machining (EDM) technique at the DESY workshop. The principle of this technique is the rapid current discharge between the electrodes, which are separated by the liquid electrode and the material of the mirror. Because the voltage between the electrodes is very high, the dielectric liquid is breaking and removing the material in between the electrodes. This technique was chosen because there is no actual contact between the electrodes and the mirror, which produces a very clean cut. 2 mm wide \times 2 cm thick fringes are rigid and do not bend significantly. Avoiding bending is important because two parts of the mirror must be aligned as parallel to each other as possible for the split beams to produce the interference on the detector. The width of the cut is much smaller than the width of the fringes (500 microns), therefore the beam losses on these spacing is kept at minimum. The schematic of the lamellar grating interferometer is presented on the Fig. 6.4.

In case when thinner fringes are needed, for example in $100\mu\text{m}$ range, it might be more beneficial to choose a different base material. Silicon would suit this purpose very well. It is possible to slice a Si wafer into micrometer thick lamellas, as has been demonstrated in the XUV community by [89, 90]. In their work authors used Si wafer with $100\mu\text{m}$ wide fingers for the reflective split-and-delay unit for XUV.

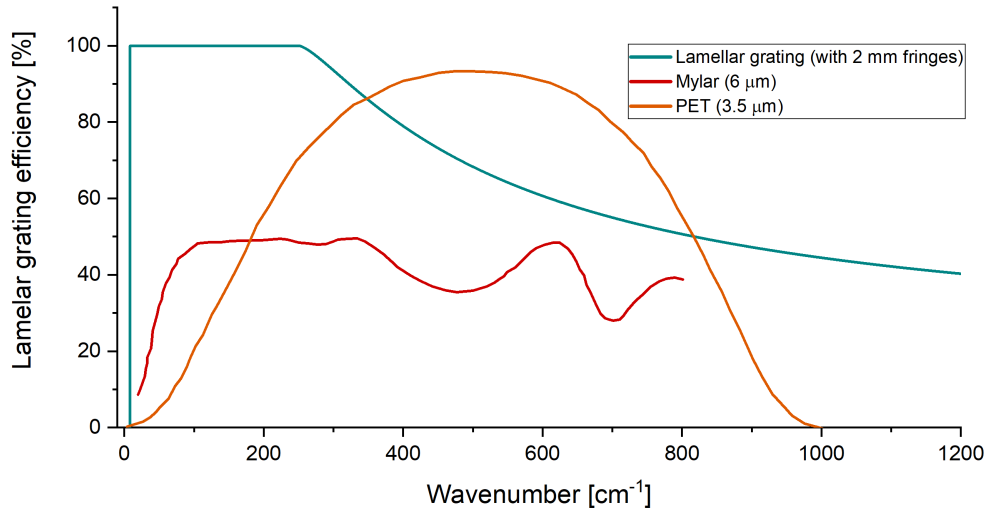


Figure 6.5: Comparison of the efficiency of the Lamellar grating interferometer (blue) with 2 mm width of the fringes to the Michelson interferometer with $6\mu\text{m}$ thick Mylar [95] (red curve) and $3.5\mu\text{m}$ thick polyethylene terephthalate (PET) [57] (orange curve) beam splitters. The efficiency of the lamellar grating has a uniform slope along a broad spectral range with the efficiency cutoff at lower σ_L due to the cavity effect.

6.2.3 Efficiency comparison to Michelson Interferometer

The efficiency of the lamellar grating interferometer within its calculated limits is higher than the efficiency of the Michelson interferometer because it does not suffer from transmission and reflection losses. It is also free from the polarization effects within its efficient range which happen when the beam components with the polarization perpendicular to the incidence plane are reflected better than the parallel components. Within the spectral range between λ_{min} and λ_{max} the efficiency of the lamellar grating is reaching 100 %. At longer wavelengths of the spectrum where the cavity effect takes place and the efficiency has a sharp cut-off at the value $\lambda_{max} = a/3.2$. At the shorter wavelength the mix of the diffraction orders at the detector limits the resolution down starting from the value $\lambda_{min} = \frac{as}{f}$. The 1st order is modulated in opposite phase with respect to the 0th order (See Fig. 6.3), therefore they can cancel each other, if they both reach the detector. In this case the efficiency of the detection is reduced.

If only the 0th and $m = \pm 1$ orders are considered to hit the detector, the Illumination on the detector looks like:

$$I_{|m|=1} \propto 2(2/\pi)^2 \frac{A\lambda}{A_{tot}} \quad (6.16)$$

where A_V and A_{tot} are the area illuminated by the 1st order beam at the detector and the total illuminated area of the detector respectively [96]. The factor 2 is coming from the sum of both

positive and negative orders and $(2/\pi)^2$ stands for the illumination of the 1st order at the peak. The 0th order illumination is equal to 1.

Therefore the efficiency of the measured interferogram on the detector is:

$$E(\nu) = \left(1 - 2(2/\pi)^2 \frac{A_\lambda}{A_{tot}}\right) \quad (6.17)$$

Assuming a circular shape of the apertures of the detector or of the slit with the diameter s and the focal length of the focusing element f , the ratio $\frac{A_\lambda}{A_{tot}}$ can be written as:

$$\frac{A_\lambda}{A_{tot}} = \left(1 - \frac{2(s-s')}{\pi s^2} (s^2 - (s-s')^2)^{1/2} - \frac{2}{\pi} \sin^{-1} \frac{s-s'}{s}\right) \quad (6.18)$$

where

$$s' = s - \frac{f\lambda}{a} \quad (6.19)$$

is a parameter for convenience of calculations. Equation 6.18 allows to calculate the efficiency of the lamellar grating for the spectral range of interest. The efficiency of the lamellar grating discussed in this work is presented on the Fig. 6.5.

At the wavenumbers ν_{max} the efficiency is reduced but still quite high (up to 40%). Michelson interferometer, on contrary, has a non-uniform, modulated low efficiency along the whole spectral range, which makes the Lamellar grating a preferable option.

6.2.4 White light interferometer for alignment

The alignment of the lamellar grating parts with respect to each other is critical for the quality of the measured spectrum. Misalignment of the reflected beam parts can lead to the situation, when each of the beams are focused on different positions on the detector and therefore the interference wither does not take place at all, or its contrast is low. Another obvious but important reason is that the movable part of the grating must move smoothly between the fringes of the fixed part without crashing into it. Taking into the account small spacing and 2 cm thickness of the mirror, it is important to take care of the possible miss-alignment.

Finding the exact zero path difference (ZPD) between two split beams is also important to produce the symmetric double-sided interferogram. This is described in more details in the next section.

To address both alignment and ZPD problems a white light interferometer was set up. White light interferometry is widely used in the topological surface studies and the inspection of optical elements[97, 98, 99]. In the work of [89] the white light interferometer was used in a similar way as in the current work: to determine and monitor the optical path difference between the parts of the lamellar grating for XUV. The reason for using white light interferometry and not any other single color, although it is much easier to align and handle, is the precision of the method. In order to find the ZPD with the highest precision possible, it is necessary to overlap

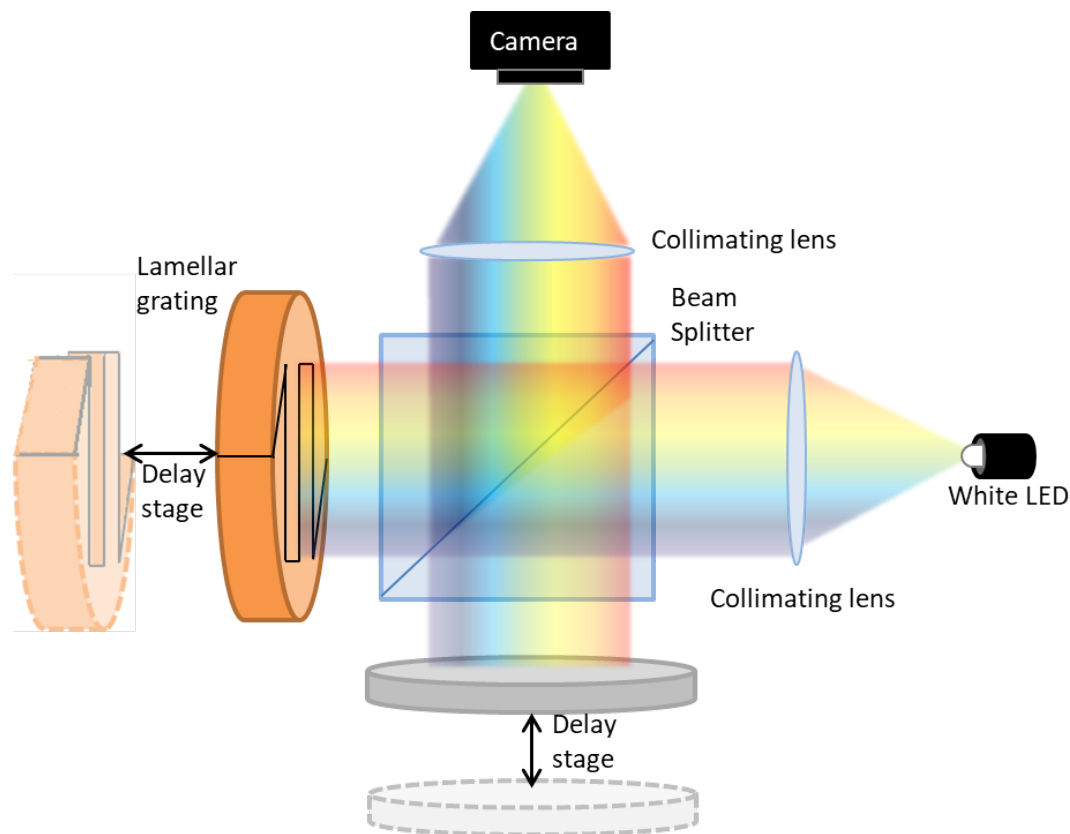


Figure 6.6: Scheme of the white light Michelson interferometer setup for the lamellar grating interferometer alignment. White light beam from the LED is split with an optical beamsplitter, one half of the beam is reflected from a metal mirror and one part is reflected from the lamellar grating. Both parts are recombined with the same optical beamsplitter on the screen (or camera).

two beams as precisely as possible which means to have the smallest coherence length of the source. The coherence length of the White LED is approximately 10 fs while the coherence of the red LED is around 140 fs.

The scheme of the white light interferometer used at the THz beamline is presented on the Fig. 6.6. The components are mounted on a separate breadboard which can be moved in for the alignment and later removed for the scanning of the THz beam. The source of the white light was the white LED from THORLABS LEDWE-15. The beam was split with a glass cube beamsplitter, after which one part was sent to a metal reference mirror mounted on a linear stage and the second part of the beam was sent to the lamellar grating, where one half of the grating was fixed and another part was also mounted on a linear delay stage. Both parts of the beam were recombined on the camera or on the screen in the image plane, where the interference was observed.

First step in alignment of the white light interferometer was to find the interference between the fixed part of the lamellar grating and the reference mirror by moving the reference mirror with the linear stage. After the temporal overlap was found for the fixed part, the interference was also found for the movable part of the lamellar grating by moving it with the delay stage. At this

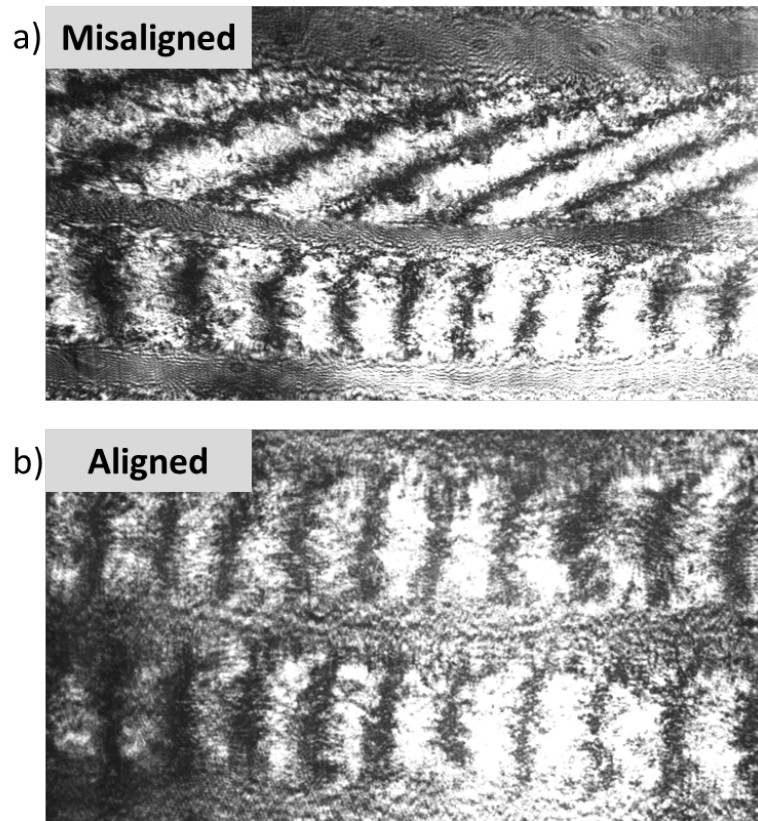


Figure 6.7: Alignment of the Lamellar grating with a red CW laser. a) miss-aligned case - the interference fringes from movable and fixed part of the lamellar grating have a different tilt. b) aligned case - interference fringes from both parts have the same tilt.

point the relative angle alignment between the parts of the lamellar grating could be established. The optical mount for the grating consisted of the rotation manipulator around Z and around X axis for the movable part and the height manipulator for the fixed part (see Fig. 6.4).

When the parts of the grating are miss-aligned then the interference fringes have a different shape: they have different tilt and different thickness, as presented on the Fig. 6.7. After changing the angle of one of them, the fringes have the same properties. The relative alignment of the angle between the parts of the lamellar grating does not necessary require the white light interferometry. Interference pattern obtained with any source of a longer coherence length, for example single color LED or a CW laser can also be used in this case. It is much easier to find the interference in this case.

Next step is to find the precise ZPD between two parts of the lamellar grating by moving the movable part around zero delay position with the linear stage. As the coherence length of the white light LED is so short and the interference pattern in very narrow, it is a very good indicator of both gratings being aligned in the same plane. Due to a longer coherence length of the red LED (LED631E from THORLABS) in comparison to the white one, it is easier use for finding the first rough timing. When the interference fringes appeared, the red LED was replaced with the white LED and the scanning was done with smaller steps until the fringes appeared again.

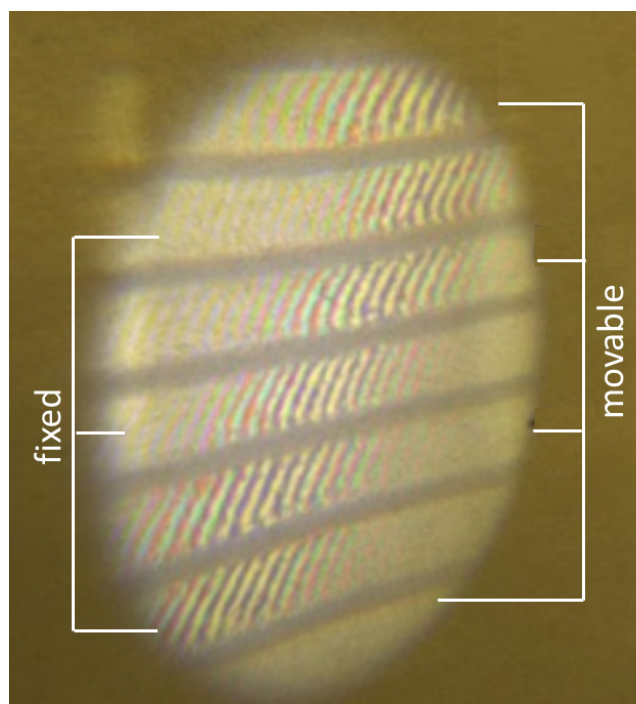


Figure 6.8: White light interferometry for lamellar grating alignment. The interference fringes appear on both movable and fixed lamellar grating parts and have the same tilt. This configuration corresponds to the time zero between the two parts and well aligned front surface of the fringes in terms of parallelism.

The result of the alignment of the lamellar grating using the white light interferometry is shown on the Fig. 6.8. Only a part of the whole grating was imaged because of the limited size of the glass-block beamsplitter. By using a larger aperture, it would be possible to image the full grating.

When the alignment procedure is done, and the white light interferometer is removed from the way of the THz beam and the scanning can be started (as presented on the Fig. 6.9).

6.2.5 THz beamline spectral characterization

The scheme of the lamellar grating FTIR spectrometer at the THz beamline is presented on the Fig. 6.10 [27]. THz beam from the beamline first went through the quartz window, separating the beamline vacuum from the ambient air in the laboratory. The quartz was later replaced with a CVD diamond window for better transmission (Transmission curve is presented on the Fig. 2.6). In order to avoid the excessive losses of the beam on the aperture of the window, it was initially focused with an off-axis parabola on the window. After the window the beam was picked up and collimated with another off-axis parabola and sent to the FTIR setup.

The challenge of spectral characterization of the THz beamline at FLASH originates not only in the broad spectrum but also in the shot-to-shot pulse energy fluctuations. These fluctuations

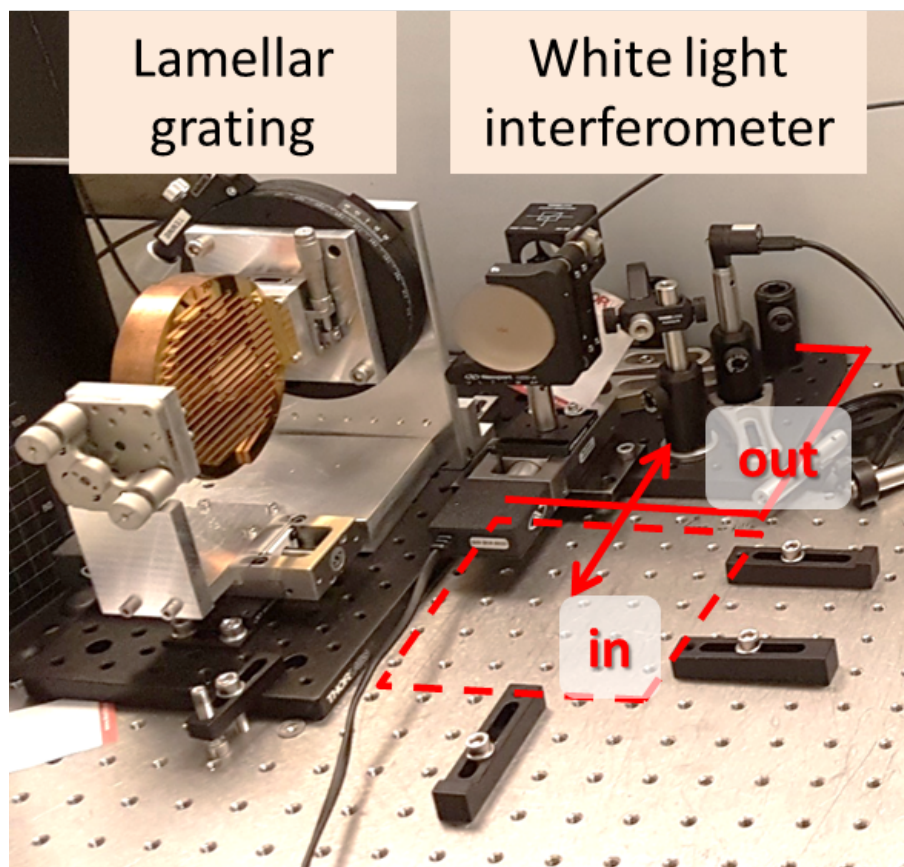


Figure 6.9: The white light interferometer setup for the alignment of the lamellar grating. White light interferometer can be moved in and out of the THz beam path on demand.

can reach up to 20 % r.m.s., therefore the reference measurement was additionally installed. In this case the intensity on the detector was reduced but the signal-to-noise ratio increased. A 100 mm diameter, 500 μm thick Si wafer split the THz beam into two parts, of which the transmitted beam was directed to the lamellar grating and the reflected beam was focused with a parabola on a pyro detector. For other cases, when high pulse energy of the beam is required and every photon is valuable the reference part can be removed.

THz beam, transmitted through the Si beamsplitter illuminated the lamellar grating homogeneously and centrally at a small incidence angle, adjusted in a way that the reflected beam would not be cut by the Si wafer (not shown on figures) and that it hits the focusing parabola centrally. Both parts of the beam, reflected from the LG were focused with a parabola with the focal length $f = 130$ mm on the pyro detector. For reference and interferometric measurements same pyro detectors with 2×2 mm chip size were used. These are also the same detectors, which were used in the plasma switch experiment from the Chapter 5 of this thesis.

An example of the measured and normalized symmetric double sided interferogram with the $OPD = 2\text{cm}$, for the THz pulse generated by the dump magnet and filtered with a 215 μm (1.4THz) band-pass filter, is presented on the Fig. 6.11. Due to the shadowing which occurs from cutting the beam at the longer delay between the mirrors, the interference signal has lower intensity. This effect appears because one part of the grating is illuminated more than the other and it might give the wrong interpretation of the spectrum during the Fourier transform. This can be avoided by reducing the incidence angle of the THz beam or by apodization or other type of filtering during processing [96].

A small portion of the beam was split for a reference measurement which is then used to normalize measured interferogram on a single-shot basis. The normalized interferogram in Fig. 6.12 was obtained during 20 minutes of scanning (12000 shots). Fig. 6.12) shows the normalized spectrum obtained by taking a Fourier Transform of the measured interferogram. The observed spectral content corresponds to the expected filter response with a signal-to-noise ratio exceeding 100. This signal-to-noise ratio is comparable to the EOS results [9].

Measurement has been performed in ambient air and a strong modulation from the water vapor absorption lines can be observed. The retrieved spectrum shows correlates well to the absorption peaks with the main portion of the spectrum lying within the bandwidth of the filter.

Another measurement result is presented on the Fig. 6.13. The scanning range was much shorter than in the previous measurement in the Fig. 6.12 - total of 2 mm corresponding to the resolution of 2.5cm^{-1} . The whole scan and the data processing took less than 10 min, which demonstrates that the lamellar grating interferometer is a quick and robust tool for monitoring and characterization of the spectrum of the THz source at FLASH.

In order to avoid the absorption in air and water vapor and to measure the reliable spectrum, it is planned to install the spectrometer in vacuum or in a gas filled chamber. This is the next step for the development of the instrument. So far at the THz beamline the vacuum chamber has

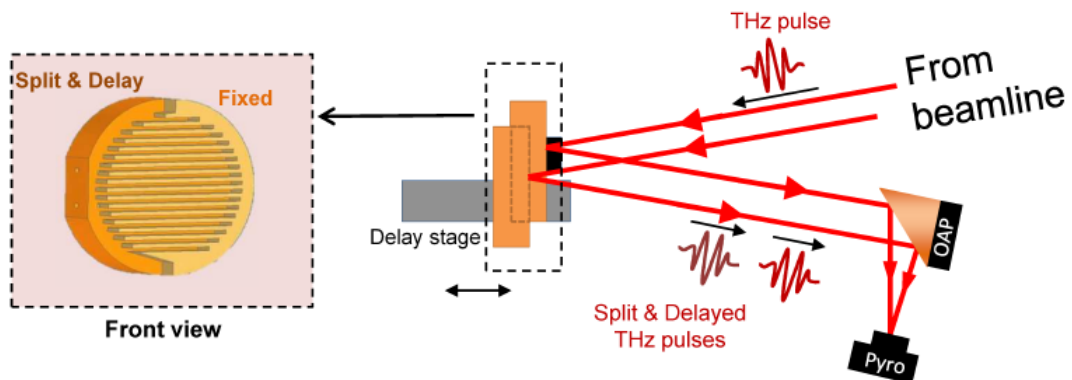


Figure 6.10: Scheme of the lamellar grating Interferometer. The THz beam from the beam-line is split into two parts with a lamellar grating and the two parts of the beam are later focused on the detector. By changing the time delay between two parts of the beam, the interferogram is measured.

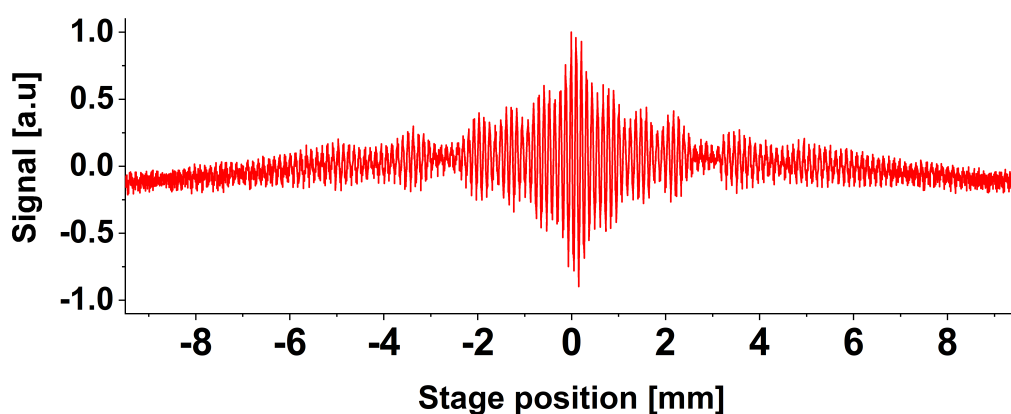


Figure 6.11: Double-sided interferogram with shadowing due to the partial cutoff of the beam reflected from the movable or fixed mirror at larger optical path difference.

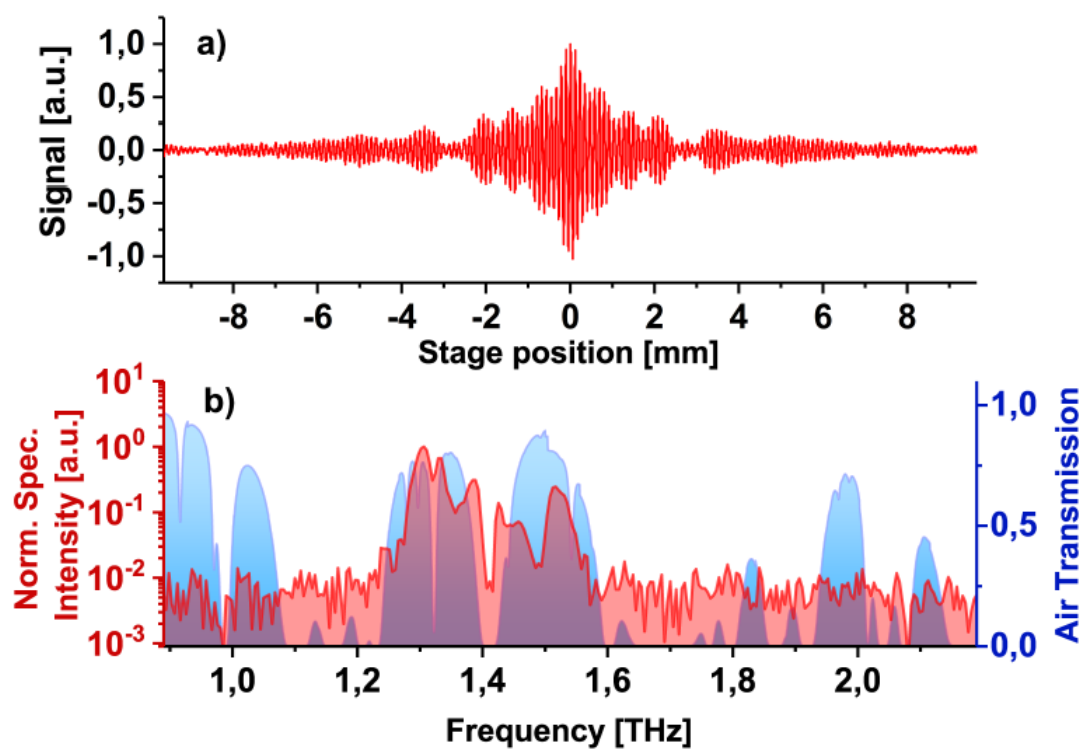


Figure 6.12: FTIR measurement for THz edge radiation with $215 \mu\text{m}$ THz band-pass filter. (a) Double-sided interferogram (b) Respective spectrum (red curve), air transmission with water vapor (in blue) shows strong absorption lines in this spectral range.

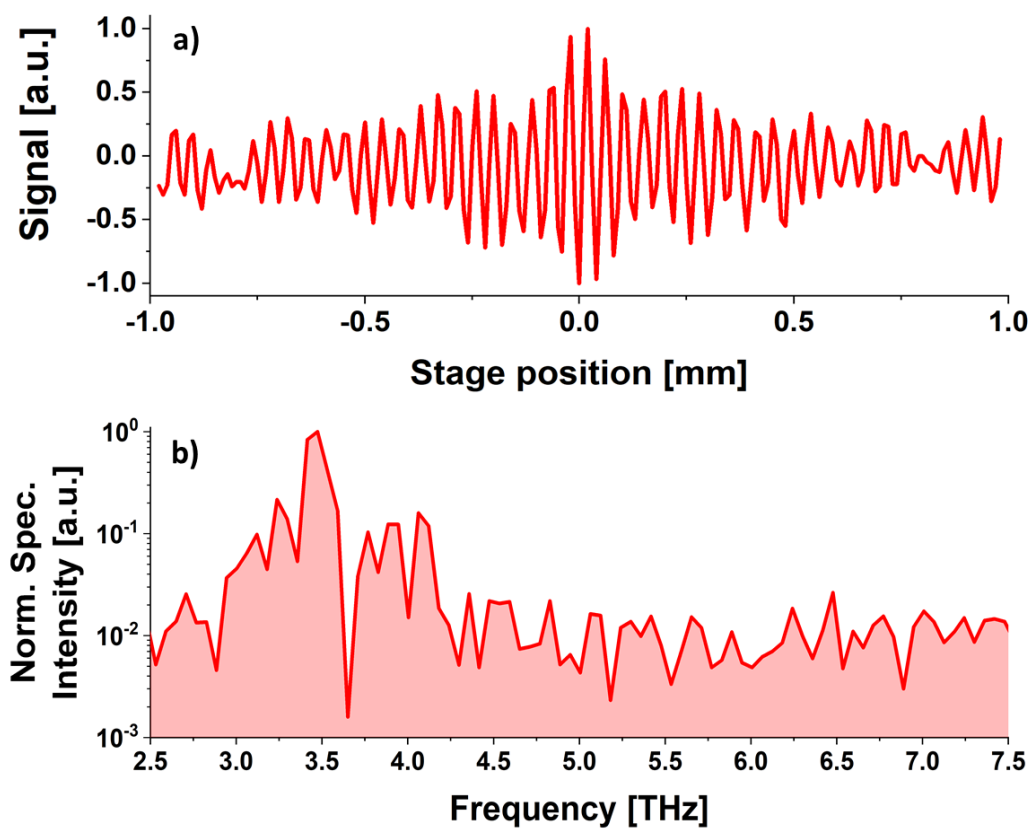


Figure 6.13: Interferogram (a) and the corresponding spectrum (b) of the dump magnet filtered with $88\ \mu\text{m}$ (3.4 THz) band-pass THz filter.

already been installed and the final commissioning of the spectrometer is to be done in the near future.

In conclusion, comparing two techniques for THz beamline characterization at FLASH (EOS and FTIR), the FTIR with the LG potentially covers a larger bandwidth and has comparable to EOS spectral to noise ratio. The time of the measurement is an important factor at big facilities like FLASH, where the experiment time is limited, that is why FTIR spectral measurements in vacuum are better in comparison to EOS.

Chapter 7

Conclusions and future perspectives

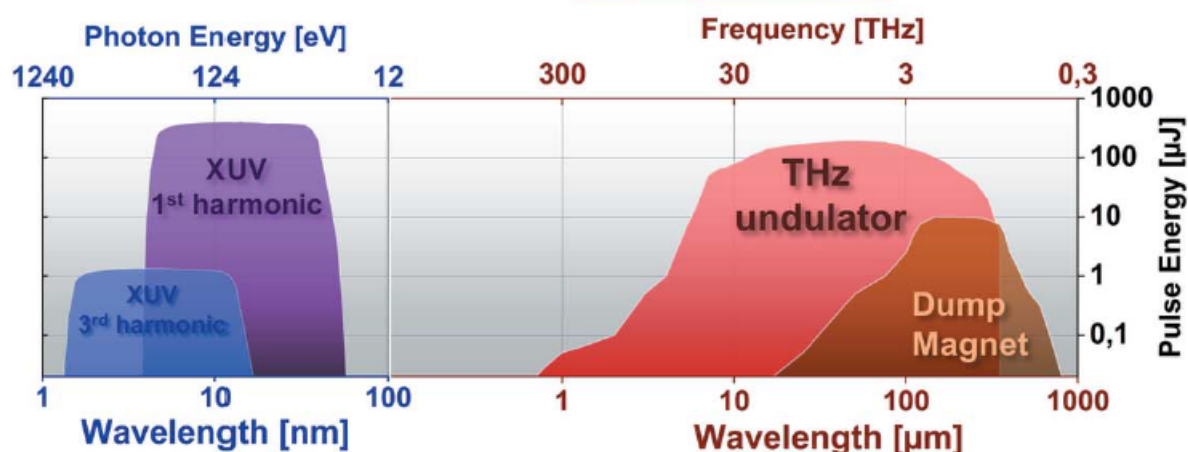


Figure 7.1: Spectral range and pulse energies from XUV and THz Sources in FLASH1. From [27]

FLASH, combined with synchronized ultrafast laser source covers the unprecedented spectral range from 1.4 nm to 300 μm , including harmonics [33], allows to perform a variety of experiments. Pulse energy and spectral range of the accelerator based light sources at FLASH1 are presented in the Fig. 7.1. THz source at FLASH covers the so-called THz gap in the electromagnetic spectrum, where very few coherent and yet high-power sources are available. In this important range between 1 THz and 10 THz lie the vibrational and rotational modes of different molecules, therefore these modes can be resonantly excited and studied. Unlike with XUV or optical radiation, THz photons excite the resonant modes without pumping the excessive energy into the system, therefore avoiding dramatic temperature increases or ionization processes. Here an overview of the most recent experiments and possibilities for the applications of the THz Doubler scheme is presented.

An example of the potential application of THz Doubler scheme is the THz-field driven streaking experiments, where high-field synchronized THz pulses are used to investigate the

electronic structured of the gas samples. Recent streaking experiments [100] studied the Auger decay in krypton and HCl molecules with the resolution much shorter than the duration of the pumping XUV pulses. This experiment opened the new range of opportunities for studies of the deep-core electronic excitations in the XUV regime. Such experiments benefit from the high-field THz pulses because it enables higher streaking field, therefore higher resolution of such experiments. With high-field THz, shorter XUV pulses, with durations in the range of tens of femtoseconds, can be better resolved.

The FLASH2020+ upgrade implies the installation of variable gap undulators for XUV in FLASH1, which will expand the possibilities of various experiments with XUV and THz dramatically. THz Doubler scheme, providing high field, synchronized THz pulses, combined with the variable XUV wavelength will enable such studies as [7] for observing the chirped Auger electron emission in the streaking experiments by scanning through the range of XUV wavelengths.

One of the exciting and intensely investigated research topics at FELs is the studies of ultra-fast magnetization dynamics of ferromagnetic materials. This topic has been studied with both IR and THz pump, where in case of using THz some thermal and electronic excitations above Fermi-energy could be avoided. The importance of these experiments reflects in the perspective of the potential development of ultrafast data storage devices [54].

With the availability of the variable XUV wavelength and the high intensity THz pulses, it will be possible for example to perform simultaneous measurements of spin dynamics of several materials with different properties [55, 101].

Such experiments being very interesting for scientific community at the same time are very challenging technically, as they require high magnetic fields of the pump THz pulses ($\approx 0.4T$) in order to induce the magneto-optical Kerr effect (MOKE) [102].

Among other applications, the THz Doubler scheme can open new frontiers for the research at FLASH, because the THz beam can be potentially transported to other beamlines like PG [103, 104], (compensating for even longer optical path difference between THz and XUV) where the dedicated XUV monochromator is installed for high resolution photoelectron spectroscopy, magnetic spectroscopy, resonant X-Ray Scattering (RIXS) experiments, etc.

The discussion about installing a dedicated high-field THz source is ongoing in the European XFEL [105]. The THz Beamline TeraFermi Trieste is running since 2018 and is already available for the users[106]. THz Doubler scheme offers an opportunity to combine the THz and X-ray pulses in the experiments fully synchronized and independent of the optical path differences between THz and X-Ray pulses at these facilities. In this case, the unique combination of wavelengths in pump-probe experiments can be achieved.

The XUV plasma switch for THz as the temporal and spatial overlap tool has been as well demonstrated in this work. The results show that the temporal overlap between XUV and THz pulses can be found within the pulse duration of the THz pulse. This proof of principle experiment was performed in both THz Doubler and the refocusing mirror geometry and showed

comparable results. The potential next step for the XUV plasma switch for THz would be the single shot measurement of the optical constants of the excited materials with the variable XUV wavelength.

When it comes to the spectral characterization of such a broadband THz source like at FLASH, only few techniques can be used. One of the ways to measure the spectrum is the lamellar grating interferometer, based on the Fourier-Transform spectroscopy, which is described in this work. The lamellar grating interferometer allows for the quick (< 20 min) spectral measurements with the adjustable spectral resolution, very broadband detection spectral range ($80\mu m$ to $1250\mu m$) and extremely high sensitivity. The next steps in the development would be to expand the effective spectral range towards shorter wavelength ($1\mu m$ to $350\mu m$), by modifying the geometry of the lamellar grating. Due to its high efficiency and robustness, the possible applications of this interferometer lie not only within the spectral characterization of the THz source at FLASH1, but also in various fields like astrophysics, biology, pharmacy and many industrial applications.

Appendix A

Acknowledgements

I would never be where I am at this moment of my life without the support of wonderful people, who helped me and inspired me along the way. These few years, which I spent on working on my PhD thesis have been both delightful and frustrating, but I'm grateful for every single one of these experiences.

I would like to give the first and most precious thank you to Nikola. We met for the first time somewhere on the DESY campus, where I got desperately lost on my first day of the summer student program in the far 2014. Next 2 months helped me to realize where I want to be in space in time, and that was in your team. Later in 2016 my dreams magically came true and you accepted me to the THz team as a PhD student. I'm forever grateful for that! And even though you always deny your status as my boss, I think you've done a great job! We've had good and tough times, ate kilos of Plasma cookies and drank liters of Fritzkola during the nightshifts. I'm glad that my project worked out during the given time and we got some nice results. I am very happy for your new position in Berlin and wish you a lot of fun, exciting experiments and cool people around. But Hamburg will be not the same without you.

Rui, you have helped me enormously during the last 4 years! There was not a single beamtime when we haven't worked together. I will never forget the frustration of 8 hour alignment procedures. Your deep understanding of physics and disciplined approach of solving problems taught me a lot. It was an honor and pleasure working with you! I wish you a lot of success in your future scientific career.

Marc, we've been through so much together and you've always believed in me in my most stupid moments and when I gave up myself already. You stayed with me aligning that horrible delay line instead of going to see your little kid, and I'm sincerely thankful for this. Without you this work would never be finished.

I'd like to thank Elke Plönjes-Palm for the kind and professional support during these years. You always have had an ear for me and encouraged me with an advice in the hard times. Thank you for taking the time and effort to supervise my work at the end. You are a wonderful group leader and person.

Siggi, thank you so much for your precious support! You always believed in me and gave me a lot of motivation to work during the long nights even when everything seemed to be a mess. In the end, with a bit of hammering the THz undulator it all worked out. It was very fun to work with you.

Karsten, I'm very thankful for your patience at the moments when I had no idea about anything and I just sat in the control room hoping that you would do the magic. And you obviously did!

Marie Kristin Czwalińska, your ability to tune for awesome THz at FLASH is fascinating! Thank you for your efforts and making these results possible.

Katja, thank you for scheduling the beamtimes for me! I know it was sometimes almost impossible to squeeze a day or two in the busy FLASH schedule. Every single beamtime was very valuable! Sometimes for various reasons it was not working smoothly, but sometimes exactly during those beamtimes we measured the best data.

I would like to thank the whole FLASH group for being so awesome. Guys, I have never worked in a better environment as with you. Everyone always had time to give me a helping hand when I needed it. I will never forget it and will be always there for you if you need me. All of you take a special place in my heart.

Torsten, there is a lot I would like to tell you and I am definitely not able to do it in just a few sentences. You are one of the reasons I came back to Hamburg and stayed here. You have inspired me to do great things and have been one of the most hard-working people I know. I remember that nightshift when you first measured your most awesome EOS trace. That was a happy moment worth years of work! You also asked me tricky questions in front of the white board at 3 o'clock in the night.. these were not very happy moments. But it was very fun working with you and it still is. Thank you for everything.

My dear Ivette, you have been my great support and voice of reason during these times. You always managed to stay cool when I rushed in your office, distracting you from everything you were doing and just pouring random information at you. You are one of the wisest and most inspiring people I have even known. I am very grateful for every second of our friendship! I hope you will finish your PhD studies soon as well and conquer the world. You have great potential in you.

Special thanks go to my PhD buddies Robin, Kostja and Jan. You guys survived my company all over these years! It's been very fun sharing the office and coffee/tea breaks with you. Thank you for the wonderful friendship and everyday support. Hope you learned from my mistakes and will go through your studies smooth and easy.

I'd like to thank Aleksandar Krmpot and Mihailo Rabasovic from the Institute of Physics in Belgrade for helping us with almost every beamtime we had. You're the THz Team for me. I will actually miss the beamtimes together, as well as amazing artworks of Aleksandar. I am sure that the end of my PhD is not the end of our friendship and we will meet in Kopaonik regularly!

Martin Büscher, you went almost through everything with me since my first day in Germany. I will always remember and will be grateful for everything you have done for me.

There is a special word for Dr. Susanne Dietz. Thank you for suddenly appearing in my life and bringing with you all the good things which were missing!

The very important place of these acknowledgements is devoted to my family. You have been my driving force during my whole life, you motivate me, push me, yell at me, never letting me stop. And I will try to never let you down. Thank you for believing in me. Tragically, our family got smaller this year, but I hope my uncle would have been proud today. I love you.

Bibliography

- [1] H. Redlin et al. *The FLASH pump–probe laser system: Setup, characterization and optical beamlines*. In: *Nuclear Instruments and Methods in Physics Research Section A-accelerators Spectrometers Detectors and Associated Equipment - NUCL INSTRUM METH PHYS RES A* 635 (Apr. 2011). DOI: 10.1016/j.nima.2010.09.159.
- [2] M. Harmand et al. *Plasma switch as a temporal overlap tool for pump-probe experiments at FEL facilities*. In: *Journal of Instrumentation* 7.8 (2012). DOI: 10.1088/1748-0221/7/08/P08007.
- [3] R. Ivanov et al. *FLASH free-electron laser single-shot temporal diagnostic: Terahertz-field-driven streaking*. In: *Journal of Synchrotron Radiation* 25.1 (2018), pp. 26–31. ISSN: 16005775. DOI: 10.1107/S160057751701253X.
- [4] U. Fröhling et al. *Single-shot terahertz-field-driven X-ray streak camera*. In: *Nature Photonics* 3.9 (2009), pp. 523–528. DOI: 10.1038/nphoton.2009.160.
- [5] G. Geloni et al. *A simple method for timing an XFEL source to high-power lasers*. In: *Optics Communications* 281 (July 2008), pp. 3762–3770. DOI: 10.1016/j.optcom.2008.03.023.
- [6] E. Zapolnova et al. *THz pulse doubler at FLASH: Double pulses for pump-probe experiments at X-ray FELs*. In: *Journal of Synchrotron Radiation* 25.1 (2018), pp. 39–43. ISSN: 16005775. DOI: 10.1107/S1600577517015442.
- [7] B. Schütte et al. *Evidence for chirped auger-electron emission*. In: *Physical Review Letters* 108.25 (2012), pp. 1–5. ISSN: 00319007. DOI: 10.1103/PhysRevLett.108.253003.
- [8] T. Qi et al. *Collective Coherent Control: Synchronization of Polarization in Ferroelectric PbTiO₃ by Shaped THz Fields*. In: *Phys. Rev. Lett.* 102 (24 June 2009), p. 247603. DOI: 10.1103/PhysRevLett.102.247603.
- [9] T. Golz. *Dissertation High repetition rate THz characterization at 4 th generation X-Ray light sources*. PhD thesis. 2018.
- [10] B. R. Steffen. *Electro-Optic Methods for Longitudinal Bunch Diagnostics at FLASH*. PhD thesis. 2007.

- [11] J. Rossbach, J.n Schneider, and W. Wurth. *10 years of pioneering X-ray science at the Free-Electron Laser FLASH at DESY*. In: *Physics Reports* 808 (Feb. 2019). DOI: 10.1016/j.physrep.2019.02.002.
- [12] S. Wesch. *Echtzeitbestimmung longitudinaler Elektronenstrahlparameter mittels absoluter Intensitäts- und Spektralmessung einzelner kohärenter THz Strahlungspulse*. PhD thesis. 2012, p. 185.
- [13] S. Schulz. *Implementation of the Laser-Based Femtosecond Precision Synchronization System at FLASH*. PhD thesis. 2011.
- [14] S. Schreiber et al. *Operation of the Flash Photoinjector Laser System*. In: *33rd International Free Electron Laser Conference* (2011), pp. 507–510.
- [15] E. Plönjes and K. Tiedtke. *The Soft X-ray Free-Electron Laser FLASH at DESY*. In: *Optical Technologies for Extreme-Ultraviolet and Soft X-ray Coherent Sources*. Berlin, Heidelberg: Springer Berlin Heidelberg, 2015, pp. 1–21. DOI: 10.1007/978-3-662-47443-3_1.
- [16] B. Faatz et al. *Simultaneous operation of two soft x-ray free-electron lasers driven by one linear accelerator*. In: *New Journal of Physics* 18 (June 2016), p. 062002. DOI: 10.1088/1367-2630/18/6/062002.
- [17] J. Wei, N. Baboi, and L. Shi. *Transverse diagnostics based on dipole mode signal fitting method in TESLA-type accelerating cavities at the free-electron laser FLASH*. In: *Phys. Rev. Accel. Beams* 22 (8 Aug. 2019), p. 082804. DOI: 10.1103/PhysRevAccelBeams.22.082804.
- [18] F. Loehl et al. *Experimental determination of the timing stability of the optical synchronization system at flash*. In: *EPAC 2008 - Contributions to the Proceedings* (2008), pp. 1386–1388.
- [19] T. Plath et al. *Free-electron laser multiplex driven by a superconducting linear accelerator*. In: *Journal of Synchrotron Radiation* 23 (2016), pp. 1070–1075. DOI: 10.1107/S1600577516009620.
- [20] *FLASH2020+ Upgrade of FLASH, Conceptual Design Report*. DESY, 2020. URL: <https://bib-pubdb1.desy.de/record/434950/files/FLASH2020pCDR.pdf>.
- [21] P. Schmüser. *Springer Tracts in Modern Physics 258 Free-Electron Lasers in the Ultraviolet and X-Ray Regime*. ISBN: 9783319040806. URL: www.mpe-garching.mpg.de/index.html.
- [22] F. Frassetto et al. *Compact spectrometer for on-line photon diagnostics at FLASH*. In: *Journal of Physics: Conference Series* 425.PART 12 (2013). ISSN: 17426596. DOI: 10.1088/1742-6596/425/12/122010.

- [23] K. Waltar et al. *Polarization-sensitive reconstruction of transient local THz fields at dielectric interfaces*. In: *Optica* 6.11 (2019), p. 1431. ISSN: 23342536. DOI: 10.1364/optica.6.001431.
- [24] M. Beye et al. *Non-linear soft x-ray methods on solids with MUSIX - The multi-dimensional spectroscopy and inelastic x-ray scattering endstation*. In: *Journal of Physics Condensed Matter* 31.1 (2019). ISSN: 1361648X. DOI: 10.1088/1361-648X/aaedf3.
- [25] T. Maltezopoulos et al. *A high-harmonic generation source for seeding a free-electron laser at 38 nm*. In: *Applied Physics B* 115 (Mar. 2014). DOI: 10.1007/s00340-013-5571-6.
- [26] E. Allaria et al. *Highly coherent and stable pulses from the FERMI seeded free-electron laser in the extreme ultraviolet*. In: *Nature Photonics* 6 (Sept. 2012), pp. 699–704. DOI: 10.1038/nphoton.2012.233.
- [27] R. Pan et al. *Photon diagnostics at the FLASH THz beamline*. In: *Journal of Synchrotron Radiation* 26.3 (2019), pp. 700–707. ISSN: 16005775. DOI: 10.1107/S1600577519003412.
- [28] O. Grimm et al. *Magnetic measurements with the FLASH infrared undulator*. In: *Nuclear Instruments and Methods in Physics Research Section A: Accelerators, Spectrometers, Detectors and Associated Equipment* 615 (Mar. 2010), pp. 105–113. DOI: 10.1016/j.nima.2009.12.018.
- [29] O. Grimm, Karsten K., and Siegfried Schreiber. *Double-Pulse Generation With the Flash Injector Laser for Pump / Probe Experiments*. 2006, pp. 3143–3145.
- [30] N. Stojanovic and M. Drescher. *Accelerator- and laser-based sources of high-field terahertz pulses*. In: *Journal of Physics B: Atomic, Molecular and Optical Physics* 46.19 (2013). ISSN: 09534075. DOI: 10.1088/0953-4075/46/19/192001.
- [31] M. Gensch et al. *New infrared undulator beamline at FLASH*. In: *Infrared Physics and Technology* 51.5 (2008), pp. 423–425. ISSN: 13504495. DOI: 10.1016/j.infrared.2007.12.032.
- [32] P. Dore et al. *Infrared properties of chemical-vapor deposition polycrystalline diamond windows*. In: *Applied Optics* 37.24 (1998), p. 5731. ISSN: 0003-6935. DOI: 10.1364/ao.37.005731.
- [33] K. Tiedtke et al. *The soft x-ray free-electron laser FLASH at DESY: Beamlines, diagnostics and end-stations*. In: *New Journal of Physics* 11 (2009). ISSN: 13672630. DOI: 10.1088/1367-2630/11/2/023029.
- [34] G. Schmid et al. *Terahertz-Field-Induced Time Shifts in Atomic Photoemission*. In: *Phys. Rev. Lett.* 122 (7 Feb. 2019), p. 073001. DOI: 10.1103/PhysRevLett.122.073001.

- [35] B. Nagler et al. *Turning solid aluminium transparent by intense soft X-ray photoionization*. In: *Nature Physics* 5.9 (2009), pp. 693–696. ISSN: 17452481. DOI: 10.1038/nphys1341.
- [36] M. Richter et al. *Multiphoton ionization of atoms with soft x-ray pulses*. In: *Journal of Physics B: Atomic, Molecular and Optical Physics* 43.19 (Sept. 2010), p. 194005. DOI: 10.1088/0953-4075/43/19/194005.
- [37] K. Honkavaara et al. *Status of FLASH*. May 2012, pp. 1715–1717.
- [38] J. Rönsch-Schulenburg et al. *Experience with Multi-Beam and Multi-Beamline FEL-Operation*. In: *Journal of Physics: Conference Series* 874 (July 2017), p. 012023. DOI: 10.1088/1742-6596/874/1/012023.
- [39] C. Gahl et al. *A femtosecond X-ray/optical cross-correlator*. In: *Nature Photonics* 2.3 (2008), pp. 165–169. ISSN: 17494885. DOI: 10.1038/nphoton.2007.298.
- [40] R. Pan. *Electro-Optic Diagnostic Techniques for the Clic Linear*. PhD thesis. 2015.
- [41] D. T.F. Marple. *Refractive index of ZnSe, ZnTe, and CdTe*. In: *Journal of Applied Physics* 35.3 (1964), pp. 539–542. ISSN: 00218979. DOI: 10.1063/1.1713411.
- [42] D.E. Aspnes and A. Studna. *Dielectric functions and optical parameters of Si, Ge, GaP, GaAs, GaSb, InP, InAs, and InSb from 1.5 to 6.0 eV*. In: *Phys. Rev. B* 27 (Jan. 1983). DOI: 10.1103/PhysRevB.27.985.
- [43] B. Green et al. *High-field high-repetition-rate sources for the coherent THz control of matter*. In: *Scientific Reports* 6. February (2016), pp. 1–9. ISSN: 20452322. DOI: 10.1038/srep22256. URL: <http://dx.doi.org/10.1038/srep22256>.
- [44] M. Chen et al. *Pulse- and field-resolved THz-diagnostics at 4 th generation light-sources*. In: *Opt. Express* 27.22 (Oct. 2019), pp. 32360–32369. DOI: 10.1364/OE.27.032360.
- [45] F. Tavella et al. *Few-femtosecond timing at fourth-generation X-ray light sources*. In: *Nature Photonics* 5.3 (2011), pp. 162–165. ISSN: 17494885. DOI: 10.1038/nphoton.2010.311. arXiv: 9809069 [gr-qc]. URL: <http://dx.doi.org/10.1038/nphoton.2010.311>.
- [46] Z. Jiang and X.-C. Zhang. *Single-shot spatiotemporal terahertz field imaging*. In: *Optics Letters* 23.14 (1998), p. 1114. ISSN: 0146-9592. DOI: 10.1364/OL.23.001114.
- [47] A. Azima. *An electro-optical timing diagnostic for pump-probe experiments at the Free-Electron Laser in Hamburg FLASH*. PhD thesis. 2009.
- [48] I. Grguraš et al. *Ultrafast X-ray pulse characterization at free-electron lasers*. In: *Nature Photonics* 6.12 (2012), pp. 852–857. ISSN: 17494885. DOI: 10.1038/nphoton.2012.276.

- [49] K. Tiedtke et al. *Gas detectors for x-ray lasers*. In: *Journal of Applied Physics* 103.9 (2008). ISSN: 00218979. DOI: 10.1063/1.2913328.
- [50] T. Oelze et al. *Correlated electronic decay in expanding clusters triggered by intense XUV pulses from a Free-Electron-Laser*. In: *Scientific Reports* 7 (Jan. 2017), p. 40736. DOI: 10.1038/srep40736.
- [51] R. Riedel et al. *Single-shot pulse duration monitor for extreme ultraviolet and X-ray free-electron lasers*. In: *Nature Communications* 4 (2013), pp. 1731–1737. ISSN: 20411723. DOI: 10.1038/ncomms2754. URL: <http://dx.doi.org/10.1038/ncomms2754>.
- [52] SCHOTT. *SCHOTT optical glass data sheets 2015-07-22*. Ed. by Schott. May 2017. URL: <https://refractiveindex.info/download/data/2015/schott-opticalglass-collection-datasheets-july-2015-us.pdf>.
- [53] S. Jamison. *X-ray science : X-ray FEL shines brightly*. In: *Nature Photonics* 4 (Sept. 2010). DOI: 10.1038/nphoton.2010.210.
- [54] B. Pfau et al. *Ultrafast optical demagnetization manipulates nanoscale spin structure in domain walls*. In: *Nature Communications* 3 (2012). ISSN: 20411723. DOI: 10.1038/ncomms2108.
- [55] F. Willems et al. *Probing ultrafast spin dynamics with high-harmonic magnetic circular dichroism spectroscopy*. In: *Physical Review B - Condensed Matter and Materials Physics* 92.22 (2015). ISSN: 1550235X. DOI: 10.1103/PhysRevB.92.220405.
- [56] M. Dell'Angela et al. *Extreme ultraviolet resonant inelastic X-ray scattering (RIXS) at a seeded free-electron laser*. In: *Scientific Reports* 6.November (2016), pp. 1–8. ISSN: 20452322. DOI: 10.1038/srep38796. URL: <http://dx.doi.org/10.1038/srep38796>.
- [57] C. C. Homes et al. *Silicon beam splitter for far-infrared and terahertz spectroscopy*. In: *Applied Optics* 46.32 (2007), pp. 7884–7888. ISSN: 15394522. DOI: 10.1364/AO.46.007884.
- [58] Tydex. *Silicon*. URL: <http://www.tydexoptics.com/pdf/Silicon.pdf>.
- [59] N. Medvedev. *Modeling ultrafast electronic processes in solids excited by femtosecond VUV-XUV laser pulse*. In: *AIP Conference Proceedings* 1464.July 2012 (2012), pp. 582–592. ISSN: 0094243X. DOI: 10.1063/1.4739911.
- [60] A. T. Tarekegne et al. *Impact ionization dynamics in silicon by MV/cm THz fields*. In: *New Journal of Physics* 19.12 (2017). ISSN: 13672630. DOI: 10.1088/1367-2630/aa936b.
- [61] M. Holzinger, A. Le Goff, and S. Cosnier. *Nanomaterials for Biosensing Applications: A Review*. In: *Frontiers in chemistry* 2 (Aug. 2014), p. 63. DOI: 10.3389/fchem.2014.00063.

- [62] H. A. Hafez et al. *Extremely efficient terahertz high-harmonic generation in graphene by hot Dirac fermions*. In: *Nature* 561.7724 (2018), pp. 507–511. ISSN: 14764687. DOI: 10.1038/s41586-018-0508-1. URL: <http://dx.doi.org/10.1038/s41586-018-0508-1>.
- [63] M. Zürch et al. *Ultrafast carrier thermalization and trapping in silicon-germanium alloy probed by extreme ultraviolet transient absorption spectroscopy*. In: *Structural Dynamics* 4.4 (2017). ISSN: 23297778. DOI: 10.1063/1.4985056. URL: <http://dx.doi.org/10.1063/1.4985056>.
- [64] F. Tavella et al. *Soft x-ray induced femtosecond solid-to-solid phase transition*. In: *High Energy Density Physics* 24 (2017), pp. 22–27. ISSN: 15741818. DOI: 10.1016/j.hedp.2017.06.001. arXiv: 1612.06698.
- [65] O. Krupin et al. *Temporal cross-correlation of x-ray free electron and optical lasers using soft x-ray pulse induced transient reflectivity*. In: *Optics Express* 20.10 (2012), p. 11396. ISSN: 1094-4087. DOI: 10.1364/OE.20.011396. URL: <https://www.osapublishing.org/oe/abstract.cfm?uri=oe-20-10-11396>.
- [66] M. B. Danailov et al. *Towards jitter-free pump-probe measurements at seeded free electron laser facilities*. In: *Optics Express* (2014). ISSN: 1094-4087. DOI: 10.1364/oe.22.012869.
- [67] Henke B.L., E.M. Gullikson, and J.C. Davis. *X-Ray Interactions: Photoabsorption, Scattering, Transmission, and Reflection at $E = 50\text{--}30,000$ eV, $Z = 1\text{--}92$* . In: *Atomic Data and Nuclear Data Tables* 54.2 (1993), pp. 181–342. ISSN: 0092-640X. DOI: <https://doi.org/10.1006/adnd.1993.1013>.
- [68] N. Medvedev and B. Rethfeld. *Effective energy gap of semiconductors under irradiation with an ultrashort VUV laser pulse*. In: *Europhysics Letters* 88.5 (2009), p. 55001. ISSN: 0295-5075. DOI: 10.1209/0295-5075/88/55001.
- [69] J. Mistrik et al. *Optical Properties of Electronic Materials: Fundamentals and Characterization*. In: Jan. 2017, pp. 1–1. ISBN: 978-3-319-48931-5. DOI: 10.1007/978-3-319-48933-9_3.
- [70] N. Ashcroft and David Mermin. *Solid State Physics*. Vol. 46. Jan. 1976. DOI: 10.1119/1.11117.
- [71] A. Tarekegne et al. *Impact ionization dynamics in silicon by MV/cm THz fields*. In: *New Journal of Physics* 19 (Oct. 2017). DOI: 10.1088/1367-2630/aa936b.
- [72] S. Bajt et al. *Multilayers for next-generation x-ray sources*. In: *Proc SPIE* 6586 (May 2007), pp. 14–. DOI: 10.1117/12.724786.

- [73] Skulina K. M. et al. *Molybdenum/beryllium multilayer mirrors for normal incidence in the extreme ultraviolet*. In: *Appl. Opt.* 34.19 (July 1995), pp. 3727–3730. DOI: 10.1364/AO.34.003727. URL: <http://ao.osa.org/abstract.cfm?URI=ao-34-19-3727>.
- [74] E. Gullikson, S. Mrowka, and B. Kaufmann. *Recent developments in EUV reflectometry at the Advanced Light Source*. In: *Proc SPIE* 4343 (Aug. 2001), pp. 363–373. DOI: 10.1117/12.436712.
- [75] S. Düsterer et al. *Development of experimental techniques for the characterization of ultrashort photon pulses of extreme ultraviolet free-electron lasers*. In: *Physical Review Special Topics - Accelerators and Beams* 17.12 (2014). ISSN: 10984402. DOI: 10.1103/PhysRevSTAB.17.120702.
- [76] J. Rönsch-Schulenburg et al. *Short sase-fel pulses at flashh*. In: *FEL 2013: Proceedings of the 35th International Free-Electron Laser Conference* (2013), pp. 379–382.
- [77] N. Medvedev et al. *Electron kinetics in femtosecond x-ray irradiated SiO₂*. In: *Contributions to Plasma Physics* 53.4-5 (2013), pp. 347–354. ISSN: 08631042. DOI: 10.1002/ctpp.201200095.
- [78] K. Y. Kim et al. *Single-shot, interferometric, high-resolution, terahertz field diagnostic*. In: *Applied Physics Letters* 88.4 (2006), pp. 1–3. ISSN: 00036951. DOI: 10.1063/1.2168897.
- [79] Y. Kawada et al. *Single-shot terahertz spectroscopy using pulse-front tilting of an ultra-short probe pulse*. In: *Opt. Express* 19.12 (June 2011), pp. 11228–11235. DOI: 10.1364/OE.19.011228. URL: <http://www.opticsexpress.org/abstract.cfm?URI=oe-19-12-11228>.
- [80] Y. Minami et al. *Single-shot measurement of a terahertz electric-field waveform using a reflective echelon mirror*. In: *Applied Physics Letters* 103.5 (2013). ISSN: 00036951. DOI: 10.1063/1.4817011.
- [81] B. K. Russell et al. *Self-referenced single-shot THz detection*. In: *Optics Express* 25.14 (2017), p. 16140. ISSN: 1094-4087. DOI: 10.1364/oe.25.016140.
- [82] S. M. Teo et al. *Invited Article: Single-shot THz detection techniques optimized for multidimensional THz spectroscopy*. In: *Review of Scientific Instruments* 86.5 (2015). ISSN: 10897623. DOI: 10.1063/1.4921389.
- [83] U. Puc et al. *Spectroscopic Analysis of Melatonin in the Terahertz Frequency Range*. In: *Sensors* 18 (Nov. 2018), p. 4098. DOI: 10.3390/s18124098.
- [84] E. Nanni et al. *Terahertz-driven linear electron acceleration*. In: *Nature communications* 6 (Nov. 2014). DOI: 10.1038/ncomms9486.

- [85] O. Ferhanoglu et al. *Lamellar grating optimization for miniaturized fourier transform spectrometers*. In: *Opt. Express* 17.23 (Nov. 2009), pp. 21289–21301. DOI: 10.1364/OE.17.021289.
- [86] J. R. Bell. *Chapter Fourteen - Sample Interferograms and Spectra*. In: *Introductory Fourier Transform Spectroscopy*. Ed. by J. R. Bell. Academic Press, 1972, pp. 180–199. ISBN: 978-0-12-085150-8. DOI: <https://doi.org/10.1016/B978-0-12-085150-8.50019-X>.
- [87] Richard T. H., D. Vrabec, and J. M. Dowling. *A High-Resolution, Far Infrared Double-Beam Lamellar Grating Interferometer*. In: *Appl. Opt.* 5.7 (July 1966), pp. 1147–1158. DOI: 10.1364/AO.5.001147. URL: <http://ao.osa.org/abstract.cfm?URI=ao-5-7-1147>.
- [88] J. Strong and G. A. Vanasse. *Lamellar Grating Far-Infrared Interferometer*. In: *J. Opt. Soc. Am.* 50.2 (Feb. 1960), pp. 113–118. DOI: 10.1364/JOSA.50.000113. URL: <http://www.osapublishing.org/abstract.cfm?URI=josa-50-2-113>.
- [89] S. Usenko et al. *Split-And-Delay Unit for FEL Interferometry in the XUV Spectral Range*. In: *Applied Sciences* 7.6 (2017), p. 544. ISSN: 2076-3417. DOI: 10.3390/app7060544. URL: <http://www.mdpi.com/2076-3417/7/6/544>.
- [90] T. Gebert et al. *Michelson-type all-reflective interferometric autocorrelation in the VUV regime*. In: *New Journal of Physics* 16 (July 2014), p. 073047. DOI: 10.1088/1367-2630/16/7/073047.
- [91] Q. Jin et al. *Observation of broadband terahertz wave generation from liquid water*. In: *International Conference on Infrared, Millimeter, and Terahertz Waves, IRMMW-THz* 071103 (2017). ISSN: 21622035. DOI: 10.1109/IRMMW-THz.2017.8067095.
- [92] P. Griffiths. *Fourier transform infrared spectrometry*. In: *Science (New York, N.Y.)* 222 (Nov. 1983), pp. 297–302. DOI: 10.1126/science.6623077.
- [93] M. Naftaly et al. *Silicon carbide—a high-transparency nonlinear material for THz applications*. In: *Optics Express* 24.3 (2016), p. 2590. ISSN: 1094-4087. DOI: 10.1364/OE.24.002590. URL: <https://www.osapublishing.org/abstract.cfm?URI=oe-24-3-2590>.
- [94] J. D. Jackson. *Classical electrodynamics; 2nd ed.* Wiley, 1975. URL: <https://cds.cern.ch/record/100964>.
- [95] X. B. Wang et al. *Surgical treatment of huge hepatocarcinoma with invasion or severe adhesion of diaphragm using the technique of orthotopic liver resection*. Vol. 62. 137. 2015, pp. 153–156. ISBN: ISBN-13: 978-0521029971 ISBN-10: 052102997X. DOI: 10.5754/hge14224.

- [96] John R. B. *Chapter fifteen - Lamellar Grating Interferometers*. In: *Introductory Fourier Transform Spectroscopy*. Academic Press, 1972, pp. 200–230. ISBN: 978-0-12-085150-8. DOI: <https://doi.org/10.1016/B978-0-12-085150-8.50020-6>. URL: <http://www.sciencedirect.com/science/article/pii/B9780120851508500206>.
- [97] J. Wyant. *White Light Interferometry*. In: *Proceedings of SPIE - The International Society for Optical Engineering* 4737 (July 2002), pp. 98–107. DOI: 10.1117/12.474947.
- [98] S. Baryshev et al. *Characterization of Surface Modifications by White Light Interferometry: Applications in Ion Sputtering, Laser Ablation, and Tribology Experiments*. In: *Journal of visualized experiments : JoVE* (Mar. 2013). DOI: 10.3791/50260.
- [99] S. Laubach et al. *Combination of a fast white-light interferometer with a phase shifting interferometric line sensor for form measurements of precision components*. In: (June 2017), p. 103291D. DOI: 10.1117/12.2269520.
- [100] K. Wenig et al. *Electronic decay of core-excited HCl molecules probed by THz streaking*. In: *Structural Dynamics* 6.3 (2019). ISSN: 23297778. DOI: 10.1063/1.5091756. URL: <http://dx.doi.org/10.1063/1.5091756>.
- [101] L. Müller et al. *Endstation for ultrafast magnetic scattering experiments at the free-electron laser in Hamburg*. In: *The Review of scientific instruments* 84 (Feb. 2013), p. 013906. DOI: 10.1063/1.4773543.
- [102] C. Vicario et al. *Off-resonant magnetization dynamics phase-locked to an intense phase-stable terahertz transient*. In: *Nature Photonics* 7.9 (Sept. 2013), pp. 720–723. DOI: 10.1038/nphoton.2013.209.
- [103] S. Dziarzhytski et al. *Microfocusing at the PGI beamline at FLASH*. In: *Journal of Synchrotron Radiation* 23 (Jan. 2016), pp. 123–131. DOI: 10.1107/S1600577515023127.
- [104] M. Martins et al. *Monochromator beamline for FLASH*. In: *Review of Scientific Instruments* 77 (Nov. 2006), pp. 115108–115108. DOI: 10.1063/1.2364148.
- [105] T. Tanikawa et al. *A superradiant THz undulator source for XFELs*. In: *Journal of Instrumentation* 14 (May 2019), P05024–P05024. DOI: 10.1088/1748-0221/14/05/P05024.
- [106] N. Adhlakha et al. *The TeraFERMI Electro-Optic Sampling Set-Up for Fluence-Dependent Spectroscopic Measurements*. In: *Condensed Matter* 5 (Jan. 2020), p. 8. DOI: 10.3390/condmat5010008.

Eidelstattliche Versicherung

Hiermit erkläre ich an Eides statt, dass ich die vorliegende Dissertationschrift selbst verfasst und keine anderen als die angegebenen Quellen und hilfsmittel benutzt habe.

Hamburg, den

Unterschrift
